On how the heating of the Solar Corona depends on the complexity of the magnetic field in the Solar Photosphere

Master of science thesis by
Øystein Håvard Færder
Institute of Theoretical Astrophysics
University of Oslo

6th March 2012

ABSTRACT

The solar corona has a temperature of order 1 MK, which is almost 200 times the temperature of the underlying surface. This fact has puzzled solar physicists for more than six decades. As of today, most solar physicists agree that the mechanism that heats the corona is connected to the dynamics of the magnetic fields in the photosphere. The question is: *how* does the coronal heating depend on the photospheric magnetic fields? That is the problem which this thesis focuses on.

Before investigating the problem, an introduction to the Sun is given, reviewing everything from the basics of a general star to the structure of the entire Sun, going through each layer, with focus on the atmosphere. Finally, the corona is brought into discussion, which leads us to the *coronal heating problem*. Two plausible heating mechanisms are discussed, both related to the generation of *current sheets*: 1) the stressing of a magnetic field which collapses into tiny current sheets (width of order 10 m) which eventually burst out as a *nanoflare*, a mechanism introduced by Parker (1988), and 2) a *hierarchy of current sheets*, analyzed by Galsgaard & Nordlund (1996), which also includes large-scale current sheets (width of several megameters) not related to nanoflares. Both mechanisms are actively referred to in the later chapters of this thesis.

To analyze the problem, the numerical code Bifrost is applied to solve the MHD equations on three-dimensional cutouts of the quiet-Sun (QS) atmosphere. Five theoretical models with different magnetic field configurations are evolved over time intervals of 30-80 min of solar time, and the resulting coronal temperatures and amounts of Joule heating (ohmic heating) in each model are analyzed, compared to each other and compared to the corresponding results of a standard model evolved by Hansteen et al. (2010).

The results confirms that both the tiny current sheets related to nanoflares and the hierarchy of large-scale current sheets *are* plausible mechanisms for coronal heating. It is plausible that the magnetic field structure in the QS photosphere is in the form of a “salt-pepper” pattern with poles of upward- and downward-oriented fields. The simulations indicate that the coronal heating *increases* with the typical separation distance between magnetic poles in the photosphere, at least when this separation distance is shorter than 6-7 Mm (which is approximately the numerical upper limit for typical separation distances in the models evolved in this thesis). This is probably because an increased mean separation distance between magnetic poles allows a more complex hierarchy of current sheets to evolve. It is also confirmed that an atmosphere of homogeneous vertical magnetic fields does not produce the high temperatures observed in the corona above unipolar regions such as plage.

ACKNOWLEDGEMENTS

First of all, I want to thank my supervisor, Viggo H. Hansteen, for giving me this project, giving me a chance to work with a famous problem which has puzzled solar physicists for more than 6 decades. I want to thank him for guiding me through the development of this thesis, always being available (on short or long distances) to answer my questions, for spending his time reading through my drafts and correcting my errors, and for looking into my numerical simulations whenever they crash. Thank you also for giving me a summer job to work with the same problem.

Also, many thanks to the other professors in solar physics at the institute for being helpful during the development of this thesis. Special thanks goes to Mats P. O. Carlsson, for answering questions related to solar physics, and for granting me access to Hexagon, a cluster of supercomputers owned by the University of Bergen and the Norwegian metacenter for High Performance Computing (NOTUR), making it possible to run my Bifrost simulations at a desirable speed. I thank Boris V. Gudiksen for demystifying the mathematics behind Bifrost. And to Luc Rouppe van der Voort, thanks for giving me nice observational pictures of the Sun to use in my thesis.

Thanks to all Ph.D. fellows who I have been able to discuss issues in solar physics with, both when it comes to the physics and to the numerical programming, and to share any frustrations related to it. Special thanks to Kosovare Olluri and Nuno M. R. Guerreiro for helping me programming with Bifrost, setting up simulation jobs on Hexagon and making fancy three-dimensional plots with Vapor.

Thanks to Torben Leifsen, Silje B. Amundsen and Unni Fuskeland for fixing any technical problems that has occurred with the computers at the institute. Thanks to Lill K. Theodorsen, Kristin Carlsson and Hans Kristian K. Eriksen for helping me with all the administrative things.

Thank you, my dear girlfriend, and soon to become wife, Glory May Santillan, for being so kind and supportive to me, and for being patient when I spend late evenings at the University working with my thesis. Thank you for always being a great source of motivation.

Thanks to all fellow students and employees at ITA for maintaining a good environment here. Thanks for all the off-topic discussions, movie nights and basement coffees.

I also want to thank the orchestra Biørneblæs were I can enjoy playing music and be social when not studying, and special thanks to fellow members of the orchestra who has read through the thesis to hunt down errors.

Many thanks to my family, for raising me up, for making me the man I am today, and for always being

there to support me.

Finally, I want to thank God, to whom I owe everything.

CONTENTS

1

INTRODUCTION

Our life-giving star, known as the Sun, has always fascinated humanity. For thousands of years, natural philosophers and, later, scientists have tried to understand its workings. As early as 2000 B.C., Chinese astronomers observed and predicted solar eclipses (which later have become an important source of information about the Sun), and in 350 B.C., sunspots were discovered by one of Aristotle's pupils, Theophrastus. The sunspots were, unfortunately, forgotten in Europe for more than a thousand years, but in China these features were being observed systematically (Priest 1982).

The real boost of knowledge about the Sun began in the 16th and 17th centuries: Copernicus (1543) stated that the Earth, as well as the five other planets known at that time, orbits the Sun instead of the Sun and the other planets orbiting Earth. Galileo Galilei "rediscovered" sunspots (after being observed by Thomas Harriot, Johannes and David Fabricius in 1611) as well as promoting Copernicus' idea of a heliocentric system, proposing that falling bodies are accelerated equally if the resistance of the medium is negligible and also proposing the principle of inertia; Johannes Kepler formulated three laws of planetary motion; Isaac Newton formulated the gravitational law and the three laws of motion. With the 18th and 19th centuries came the development of thermodynamics and atomic theory, the invention of photography and the discovery of atomic spectra, and with the 20th century came the development of quantum physics, the invention of the computers (and later parallel computers), the invention of CCDs (digital imaging devices used in telescope) as well as great enhancement in several observational instruments, amongst others telescopes and spectrographs. All of this has helped astronomers to gain a solid physical understanding of our mother star. Still, there are several mysteries about the Sun that remain to be solved.

1.1 A Review of our Current Knowledge about Stars

The Sun is a *star*, located in a *galaxy* known as the Milky Way, orbiting the galactic center with a speed of 220 km/s at a distance of 26400 light years (Kerr & Lynden-Bell 1986) . A galaxy is a huge accumulation of stars, usually shaped like an ellipsoid or a spiral disc, where the latter is the case of our galaxy. Assuming circular orbit, we can use the orbital speed of the Sun to find out that the solar orbit encloses a mass of $\sim 10^{11}\ M_\odot$, where $M_\odot$ is the solar mass. Since the outer-lying mass in fact counts at least 50 % of the total mass, and since most of the stars are less massive than the Sun (because the more massive stars die more quickly due to a much higher hydrogen burning rate), we can estimate

that there are between a few hundred billion and one trillion stars in the Milky Way. The Milky Way is one of more than 30 galaxies in a galaxy cluster known as the Local Group (Karachentsev et al. 2009). The cluster is $\sim$ 10 Mly (megalightyears) from the nearest neighbor cluster (Karachentsev 2005) and part of a $\sim$ 100 Mly wide disk-shaped supercluster (Kalinkov 1983), the Virgo Supercluster, making the Local Group one of $\sim (100\ \mathrm{Mly}/10\ \mathrm{Mly})^2 = 100$ clusters in the Virgo supercluster. The nearest neighbor superclusters are about 300 Mly away. Assuming that the density of superclusters is more or less homogeneous in the observable universe, which has a radius of $\sim$ 50 Gly (Gott et al. 2005), we can estimate that there are about $4/3\pi(50\ 000/300)^3 \sim 10^7$ superclusters in the observable universe. This means that there are more than 30 billion galaxies in the observable universe (the Hubble Space Telescope has estimated at least 80 billion), and the Sun is only one of more than 10^{22} stars. Before going into the details about the Sun, it is therefore important to have some basic knowledge about stars, i.e. what they are and how they work.

A star is a *ball of self-gravitating gas* that produces energy through atomic *fusion* in the core. Energy is transported through the different layers of the star until it leaves the star's surface, mostly in the form of *electromagnetic radiation*, while some of the energy that leaves the surface is deposited in a stellar wind, i.e. particles which move away from the star with a high velocity. A star can be surrounded by smaller spherical objects, known as *planets*, and if a planet is made of right material and lies close enough to the star, but not too close, the electromagnetic radiation from the star will warm up the planet sufficiently for the possibility of *life*.

We usually put the stars into different *spectral classes* by considering their *effective temperature* T_{eff}. Stars radiate almost like perfect black bodies, and therefore, after measuring the spectrum of a star, we can find the Planck radiation curve that fits the spectra optimally, see figure 1.1. More specifically Wien's displacement law states that the effective temperature of a star is related to the wavelength λ_{top} (measured in Ångstrøm), where the top of the Planck curve occurs, by $\lambda_{\mathrm{top}} T_{\mathrm{eff}} = 2.90 \cdot 10^7$ Å·K. The effective temperature of a star is roughly equal to its surface temperature, where the surface is defined as the spherical layer around the star where the bulk of the visual light emitted from the star becomes optically thin. The red stars, which have spectra centered around the longer wavelengths ($\lambda_{\mathrm{top}} > 6\ 500$ Å), therefore have cooler surfaces ($T_{\mathrm{eff}} < 4\ 500$ K), while the blue stars, with spectra centered around the shorter wavelengths ($\lambda_{\mathrm{top}} < 1000$ Å), have hotter surfaces ($T_{\mathrm{eff}} > 30\ 000$ K). Since the visible light only ranges from about 3800 Å to 7400 Å, we only see a small part of the spectrum of the hottest stars ($\lambda \sim 4000$ Å, which is blue light). The main spectral classes are, from hottest too coolest, the following: O, B, A, F, G, K, M. Additionally, each spectral class is divided into 10 bins indicated by a number from 0 to 9.

The other important stellar classification is the *luminosity class*, denoted by a roman number from I to V. The luminosity of a star is a measure of the electromagnetic energy which the star releases per time unit, and for a specific spectral class, the most luminous stars are in class I and the least luminous in class V. But this does *not* mean that the stars in the same luminosity class have roughly the same luminosity. In reality, the luminosity class tells us more about what kind of stars we are dealing with. Stars in class V are the so-called *main sequence* stars, while stars in classes I-IV are giants (class I denotes the most luminous supergiants). A main sequence star is a star which is in a physically stable state (does not undergo any dramatic changes in temperature and density) and where the only fusion process that takes place is fusion of hydrogen to helium (H→He) in the stellar core. Giant stars (classes I-IV) are older stars, depleted of core hydrogen, where H→He fusion takes place in

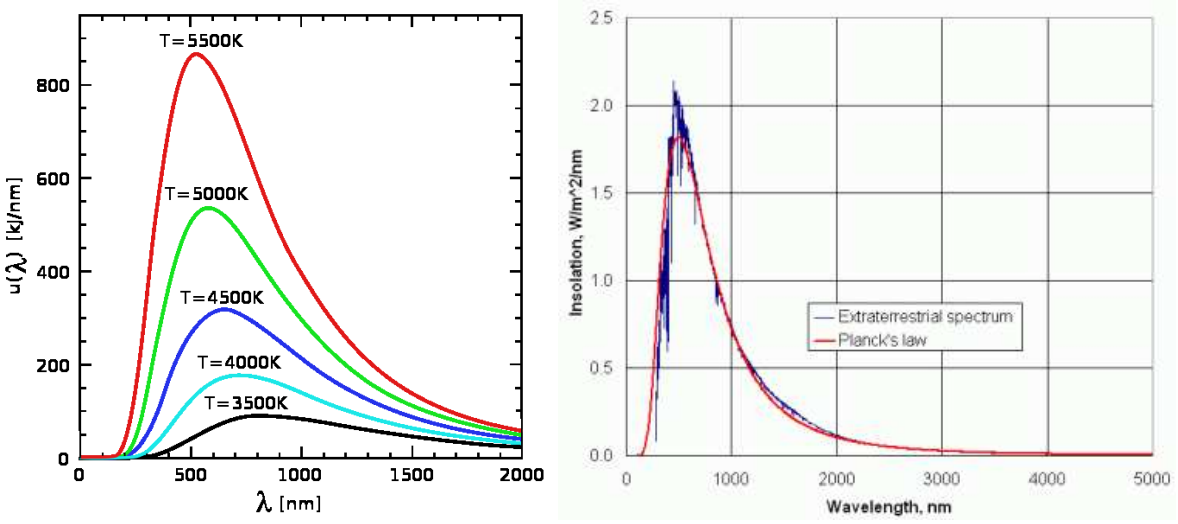

(a) Planck curves for black bodies with different temperatures.

(b) The solar spectrum fitted with a Planck curve for a black body with a temperature of 5800 K.

Figure 1.1: Planck curves and the Solar spectrum. Images are reprinted from `http://en.wikipedia.org/wiki/Planck's_law` and `http://www.pages.drexel.edu/~brooksdr/DRB_web_page/papers/UsingTheSun/using.htm`

surrounding shells. Additionally, fusion into heavier elements might occur, depending on the mass of the star. Figure 1.2 shows a Hertzsprung-Russell diagram where the stellar classification is visualized. It also shows the position of the Sun in an HR diagram.

Stars are formed in dense clouds of interstellar medium (ISM). The ISM is the matter that exists in space outside star systems, consisting of both ionized, atomic and molecular gas. Since these clouds are always in chaotic movement, several clouds might collide into each other, and this will cause the gas to compress. When a cloud gets dense enough, its internal gravitational forces will be so strong that it cannot be balanced by the forces due to the gas pressure. The mass of the cloud is then greater than the Jeans mass,

$$M_J = \frac{4\pi}{3}\rho R_J^3 = \frac{\pi c_s^3}{6G^{3/2}\rho^{1/2}},$$

where ρ is the mass density, R_J the Jeans radius, c_s the sound speed and G the gravitational constant. This triggers a gravitational collapse, where gas falls towards the centre of the cloud (i.e. the cloud is *accreting*). Since the accreting cloud is initially rotating, and since the angular momentum of the cloud is conserved, the gas outside the central part of the cloud rotates faster. This leads to a rapidly increasing centrifugal force which halts the in-falling gas in the rotation plane. Since there are no forces halting the gas from falling in from other directions, this leads to the development of a central mass, i.e. a *protostar*, surrounded by a flattened disc of rotating plasma (*accretion disc*). At some point, the accretion of the surrounding plasma stops, and we have a *pre-main-sequence star* (PMS star), which gets its energy from gravitational contraction, surrounded by orbiting clouds of cooler gas. The gravitational contraction in the PMS star continues until its core gets hot enough (10^7 K) to

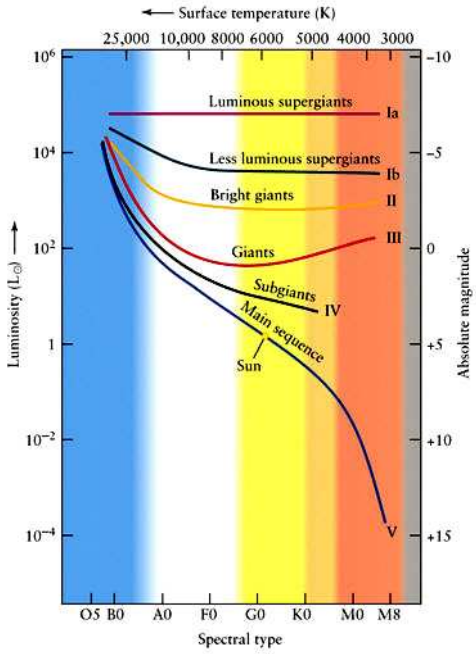

Figure 1.2: Hertzsprung-Russell diagram with stellar classification. The image is reprinted from `http://www.astro.lsa.umich.edu/undergrad/Labs/MWDisk/mwdisk.html`

start H→He fusion, and we have a *main sequence star*. Meanwhile, the surrounding orbiting clouds of gas cool down and condense into denser objects and end up as solid objects e.g. planets, asteroids and comets.

The high increase in the temperature due to the ignition of the hydrogen core (i.e. beginning of H→He fusion) causes the pressure gradient force to increase (due to an increase in the gas pressure) until it becomes strong enough to balance the gravitational force. In other words, hydrostatic equilibrium is achieved. The star is now in a stable phase and will remain so until the core hydrogen is more or less depleted. In fact, most stars spend more than 80 % of their lifetime as main sequence stars.

The core is only a small part of the stellar interior. Between the core and the surface, a star can have a *radiative* and/or a *convective* zone. These zones are discussed more in detail in section 1.2.1, but the main distinction between these two zones is the following: in a radiative zone, the efficient way of transporting energy outwards is by the diffusion of electromagnetic radiation, while in a convective zone, the energy transport is dominated by convective motion i.e. parcels of hot gas are buoyant and rise up to cooler regions, thereafter they cool and sink again. Convection is efficient in regions where the temperature drops fast enough with height (see section 1.2.1). Red dwarf stars (class M) are much smaller than other main sequence stars and have relatively cool surfaces ($\sim$ 3000 K), which means that they have a temperature that drops much faster with height than in the larger main sequence stars. In fact, the temperature drops fast enough to cause the entire star to be convective outside its core. As a result, the helium produced in the core is continuously mixed with the hydrogen in the envelope, which secures fresh amounts of hydrogen for the core to burn to helium. This means that the entire star works as a H→He "power plant" until all hydrogen in the star has turned to helium. Because red dwarfs have relatively small masses (down to 0.4 solar masses), the gravitational force on the core

is also relatively small and requires therefore less gas pressure from the core to maintain hydrostatic equilibrium. Therefore, the hydrogen burning goes quite slowly, and the time it takes from the birth of a red dwarf until the star is depleted of hydrogen can be calculated to be of order trillions of years i.e. much longer than the current age of the universe. Solar-like stars have a radiative zone around the core, and then a convective zone. Stars heavier than $1.1M_{\odot}$ (Maeder & Meynet 1989) have cores which fuse hydrogen to helium in a different way than stars with smaller masses (CNO-cycle instead of pp-chain), and this results in a higher core temperature, hence a higher temperature gradient around the core, which leads to a thin convective layer around the core. More massive stars have thicker convective layer around the core and thinner convective layer below the surface. In general, according to Schwarzschild (1958), upper main sequence stars (OBA class stars) have convective inner envelope and radiative outer envelope, while it is the opposite for lower main sequence stars (solar-like stars and lighter stars) except for M class dwarfs. OBA class stars therefore have smooth surfaces compared to lower main sequence stars, both because they have no granulation pattern (a characteristic surface pattern due to underlying convection) and because they have no magnetic field which extends outside the surface (hence no starspots, which are concentrations of strong magnetic fields on the surface). The only exceptions are some OB class stars where observations indicate magnetic fields which extends out of the surface, probably in the form of a stable field configuration (Braithwaite & Nordlund 2006).

When a star is depleted of core hydrogen, unless it is an M class dwarf (where all hydrogen is turned to helium in the end), the temperature and hence the gas pressure decreases abruptly due to the halt in the H→He fusion, and the star begins to contract. This continues until the shell which surrounds the core is hot enough to start H→He fusion. This produces a pressure gradient force which is too strong to be balanced by the gravitational force, and the outer envelope of the star expands rapidly. Solar-like stars are at this point in a phase known as the *red giant branch* (RGB), because they have expanded so quickly that the surface has cooled and turned red. What happens after the H→He burning shell is depleted of hydrogen depends on the mass of the star. Figure 1.3 shows how different post-main-sequence stars change their position in an HR-diagram during the final stages of their lives.

According to Lattanzio & Forestini (1999), stars heavier than $0.6M_{\odot}$ start fusing helium to carbon and oxygen in the core and later in the surrounding shell (after depletion of core helium). Solar-like stars are at this point entering a *horizontal branch* (HB) where they move to the left and right several times in the HR diagram i.e. their size and surface temperature are oscillating. The existence of a horizontal branch was discovered in the first detailed studies of globular clusters (Arp et al. 1952; Sandage 1953).

When the core is depleted of helium, i.e. when the entire core consists of carbon and oxygen, the star contracts due to the lack of a sufficient pressure gradient. When the gravitational pressure on the helium shell around the core is high enough, this shell starts fusing helium into carbon and oxygen. The star is now in the *asymptotic giant branch* (AGB) where it undergoes an enormous expansion because of the enormous pressure gradient due to the shell helium fusion. Because of the rapid expansion, the surface will be cold and red, hence this kind of star is known as a (super) *red giant*. Finally, the outer layers of the red giant are thrown off in the form of a planetary nebula, and the remainder is a hot core made of oxygen and/or carbon, known as a *white dwarf*.

Stars with higher mass can fuse carbon and oxygen into even heavier elements, but not heavier than iron (which is the element with the lowest energy per nucleon). These stars turn into supergiants and end their lives in powerful explosions known as *supernovae*. Possible stellar remnants after a

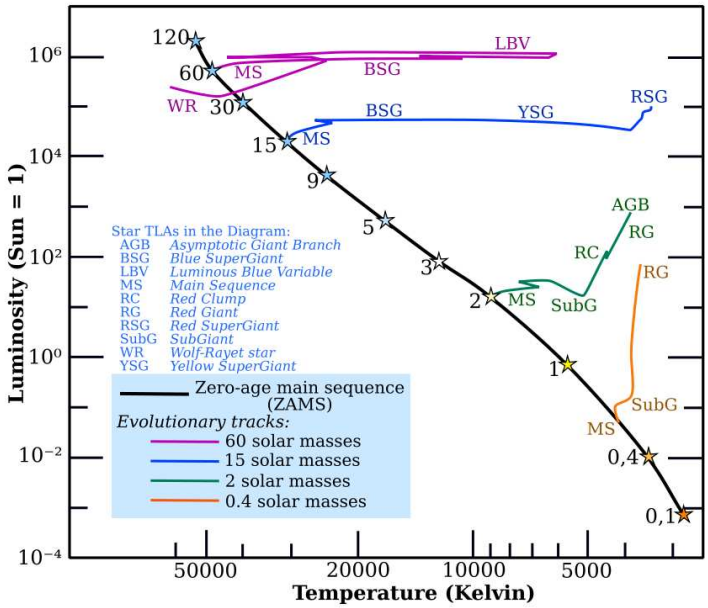

Figure 1.3: Selected stellar evolutionary tracks in an HR diagram. The numbers along the main sequence line shows the stellar mass in units of the solar mass. Image is reprinted from `http://en.wikipedia.org/wiki/Asymptotic_giant_branch`

supernova are *neutron stars* and *black holes*. Supernovae are powerful enough to produce elements heavier than iron.

In the early universe, there was only hydrogen and helium and some lithium, because these where the only elements which were efficiently created by Big Bang nucleosynthesis. Therefore, the oldest stars in the universe contained only these three elements. Later, after stars had produced heavier elements and released them in supernovae, these elements was spread into the ISM, and then new stars could be born with small amounts of heavier elements. The youngest stars are therefore the ones which are the richest in metals. Astronomers distinguish between population I, II and III stars, population I stars are rich on metals while population II and III stars have little or no metals. This means that population I stars are the youngest stars in the universe, and population II and III stars are the oldest. Note that very few, if any, population III stars have been found.

It is important to point out that our main (and practically only) source of information about a star is the electromagnetic (EM) radiation that we receive from it. As mentioned earlier in this section, from the spectrum of EM radiation we can first extract a Planck curve which tells us immediately about the star's effective temperature. But this Planck curve is "disturbed" by emission and absorption lines, because a star (obviously) consists of atoms that can absorb and emit photons. Because each chemical element has its characteristic absorption/emission lines, we can first of all use the line spectra to find out which elements that are present in the star and estimate the abundance of each element by measuring the intensities of the lines. The lines might be Doppler shifted or broadened due to velocities, and therefore Doppler shifts and Doppler widths can give us information about the star's rotation velocity, large-scale velocities of plasma inside the star and its temperature (since the Doppler width increases with the thermal velocities). The presence of a magnetic field can cause a Zeeman effect i.e. a splitting of one spectral line into several spectral lines, and by measuring the distance

between the lines it is possible to estimate the magnitude of the magnetic field. Because the light (or absence of light in the case of an absorption line) at a specific line that we receive from a star is often mainly produced at a specific depth inside the star, we can measure the intensity, Doppler shifts, Doppler widths, Zeeman effect and other spectral line effects from many different lines to estimate the temperature, large-scale velocities, magnetic fields and abundances of the different chemical elements in different regions inside the star's atmosphere and thus obtain a detailed knowledge about it.

1.2 A Review of our Current Knowledge about the Sun

The Sun is a yellow dwarf star, and figure 1.2 shows that it is a main sequence star in spectral class G. More specifically, it is a population I star of spectral class G2 V. It is in its middle age, approximately 5 billion years old, and has a mass $M_\odot = 2 \cdot 10^{33}$ g, a radius $R_\odot = 700$ Mm, an effective temperature $T_{\text{eff}} = 5780$ K and a luminosity $L_\odot = 3.84 \cdot 10^{33}\ \text{erg/s}$ (Schrijver & Siscoe 2009; Rusov et al. 2010). According to recent works by Asplund et al. (2009), the Sun consists of 73.81 % (of total mass) hydrogen(H), 24.85 % helium(He), and the last 1.34 % is oxygen(O), carbon(C), neon(Ne), silicon(Si), nitrogen(N), Magnesium(Mg), iron(Fe), sulfur(S) etc. in order of decreasing mass abundance.

The Sun, as other stars, is divided into several layers. The solar interior consists of a *core*, where energy is produced by H→He fusion, a *radiative zone* where the energy produced in the core is transported (very slowly) outwards by diffusion of electromagnetic radiation, and a *convective zone* where the energy is transported further outwards by convection until it reaches the surface. The surrounding solar atmosphere consists of a *photosphere*, where the bulk of the electromagnetic radiation that leaves the Sun is emitted, a *chromosphere*, being a mostly transparent layer with relatively constant temperature (about 4000-7000 K), a *transition region*, where the temperature rises to 1 MK within a height range of no more than a few megameters, and a *corona*, which is a very hot ($\sim$ 1 MK) and transparent layer (in visible light) which can be seen as a crown around the Solar disk at Solar eclipses.

The Sun undergoes differential rotation, which means that the gas at different latitudes moves around the Solar axis with different angular velocities. The rotation period is about 25 days at equator, increases with latitude and is more than 30 days at latitudes higher than 60° (Khokhlova 1959). Differential rotation, combined with convective motions beneath the surface (which in fact is the cause of the differential rotation), is responsible for the dynamo which generates and maintains the magnetic fields and the magnetic activity on the Sun.

1.2.1 An Overview of the Solar Interior

Leighton et al. (1962) discovered *solar oscillations* during analysis of velocity fields in the solar atmosphere. This gave rise to a study known as *helioseismology*, which has later played a large role in mapping the solar interior. According to Gizon et al. (2010), helioseismology provides precise tests of the theory of stellar structure and evolution, and it also enables the study and discovery of effects not included in standard solar models (standard models of the solar interior are spherically symmetric models without rotation and magnetic fields and with a simplified treatment of convection). There are three kinds of solar oscillations that are usually studied in helioseismology: 1) p-modes i.e. pressure-driven waves, 2) g-modes i.e. gravity-driven waves and 3) f-modes which are gravity waves that

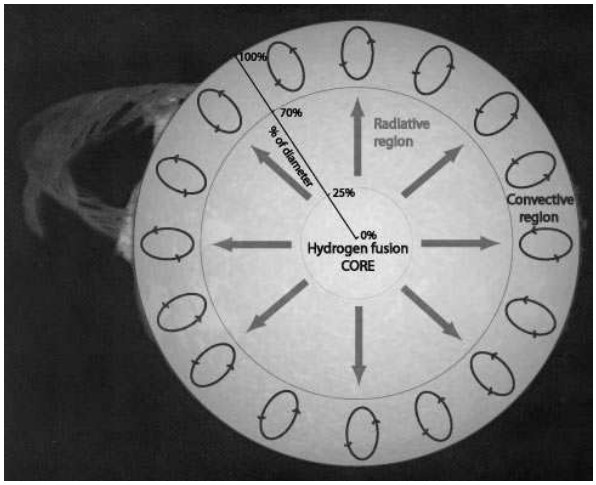

Figure 1.4: Structure of the Solar interior, adapted from Inglis (2003)

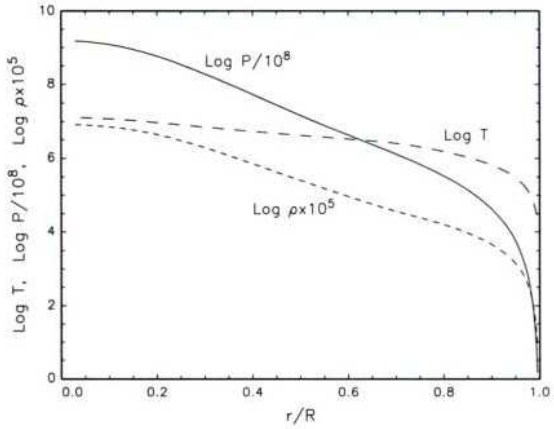

Figure 1.5: Log of temperature in K, pressure in 10^8 $\mathrm{dyn/cm^2}$ and density in 10^{-5} $\mathrm{g/cm^3}$ as function of fractional radius, where $R = 0.886 R_\odot$. The plot is reprinted from Hansen et al. (2004).

occurs near the surface.

The solar interior is made up by a core, a radiative zone and a convective zone as shown in figure 1.4. It has a temperature, density and pressure which decreases with height as in figure 1.5. It consists mainly of hydrogen and helium and less than 2 % of heavier elements. Since the core continually fuses hydrogen to helium, the abundances of helium is much higher near the core than in the outer regions, while it is the opposite case for hydrogen. Kosovichev (1995, 1996) applied helioseismology to estimate how the abundances of hydrogen and helium depend on the distance from the core, as shown in figure 1.6.

The battery of the Sun lies in *the core*. It has a temperature of $14.5 \cdot 10^6$ K and a pressure of $\sim 10^{17}$ $\mathrm{dyn/cm^2}$, causing hydrogen to be fused into helium by a process known as the proton-proton chain (and not the CNO cycle which requires an even higher temperature to be efficient). The process consists of several steps, but roughly it produces one helium nucleus (He^{2+}) and some positrons and

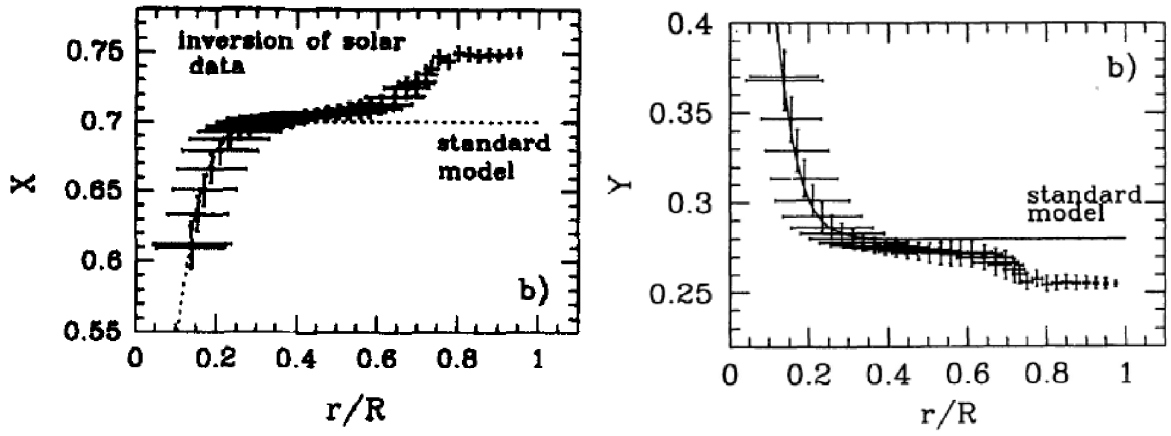

Figure 1.6: Measures of the abundance of hydrogen (left) and helium (right) inside the Sun, reprinted from papers by Kosovichev (1995, 1996).

neutrinos out of four H^+ ions[1] (or protons). The He nucleus has slightly less mass than the 4 H^+ ions, and the rest energy of this mass difference Δm is released as photons, with energy given by $E = \Delta mc^2$ (Einstein 1905). We must also count the photons produced when the positrons released during the pp-chain annihilates with electrons (there is roughly one electron for each proton). Since almost all of the energy released by the fusion processes in the core exits the Sun as electromagnetic radiation, the total energy per second released from the core due to the hydrogen fusion is approximately equal to the luminosity, that is $3.84 \cdot 10^{33}$ erg/s.

Outside the core, at a radius of $r \sim 0.2\ R_\odot$ is a *radiative zone*. Here, the photons produced in the core diffuse slowly outwards. According to Mitalas & Sills (1992), it takes about $1.7 \cdot 10^5$ years for an average photon to travel through the radiative zone. Because of the high density and pressure, the mean free path (averaged over the entire zone) is about 0.09 cm, which causes a travelling photon to be absorbed by an atom and then re-emitted in another direction almost every 10^{-12} s.

Above $r = 0.7\ R_\odot$, convective instability occurs. This means that if a parcel of gas starts to move upwards, the parcel will continue to rise, because it is buoyant,

$$\delta\rho_i < \delta\rho, \tag{1.1}$$

where $\delta\rho_i$ and $\delta\rho$ are the density changes inside the parcel and in the surrounding medium, respectively. Considering the temperature T, density ρ, pressure P, gravitational acceleration g and mean particle mass m in the fluid, we assume horizontal pressure equilibrium i.e. no excess pressure in horizontal direction, ideal gas law i.e. $P = \rho k_B T/m$ and hydrostatic equilibrium i.e. $\partial P/\partial r = -\rho g$ (which means that the gravitational force is balanced by the pressure gradient) to obtain the Schwarzschild condition for convective instability,

$$-\frac{\partial T}{\partial r} > \frac{\gamma - 1}{\gamma}\frac{gm}{k_B}, \tag{1.2}$$

[1]Because of the extremely high temperature, all atoms are completely ionized

where r is the radial coordinate, $\gamma = 5/3$ the adiabatic exponent and k_B the Boltzmann constant. The right-hand side term is known as the *adiabatic temperature gradient* (Priest 1982).

As already mentioned, this criterion is fulfilled above $r = 0.7\ R_\odot$, in the *convection zone*. As a consequence of the convective instability, parcels of heated gas are transported up towards the surface, then slowed down due to radiative cooling. The parcels keep moving horizontally along the surface until they are dense enough to sink again. The convective mechanism, rather than radiation, transports energy upwards through this zone.

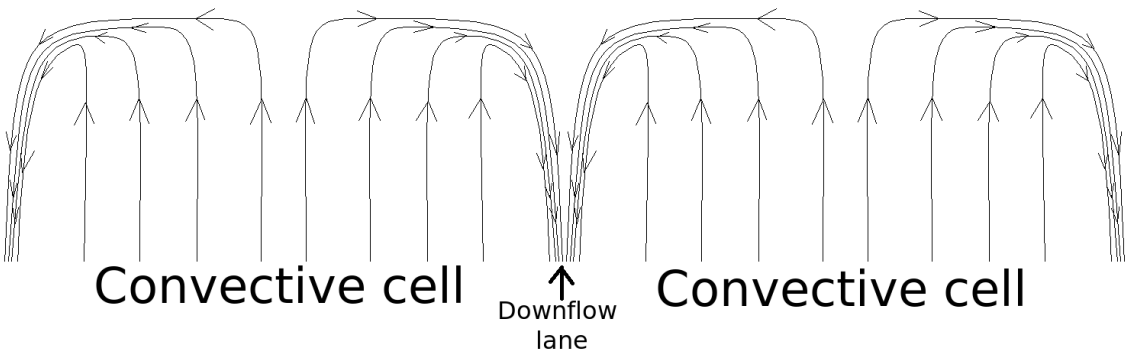

Figure 1.7: Two-dimensional sketch of (the top of) convective cells.

In convection, the upflows of heated plasma are organized in cells while downflows of cool and denser plasma are concentrated in thinner inter-lying lanes, as shown in figure 1.7, but with higher velocity than the upflows so that the total mass flux over a large convection pattern is zero. Convective cells appear in several sizes, all from 1-2 Mm (in upper convection zone, seen as *granulation* in the surface) to ~ 100 Mm (*giant cells*, extends through almost the entire depth of the convection layer but not visible on the surface), according to Stix (2004).

1.2.2 An Overview of the Solar Atmosphere

The solar atmosphere is usually divided into four layers, from innermost to outermost, these are known as the *photosphere*, the *chromosphere*, the *transition region* and the *corona*. Each layer can be characterized by how the *temperature* behaves. Let us therefore consider figure 1.8(a) which shows the modeled temperature in the solar atmosphere as function of height obtained from a numerical simulation (using Bifrost, described in the next chapter). Starting at $z = -1$, the temperature decreases relatively slowly, but around $z = 0$, there is a 200-300 km thick region where it decreases quite rapidly. This is the *photosphere*, where the bulk of the visible light becomes optically thin, causing the fluid to undergo radiative cooling. Above $z =$ 200-300 km is a region of relatively constant mean temperature (or decreasing and then increasing slowly with height) which is called *chromosphere*. It extends up to heights between 1.5 Mm and 3.0 Mm above the photosphere,[2] depending on the local fluid dynamics. The region where the temperature increases rapidly with height, from $T = 2 \cdot 10^4$ K to $T \sim 10^6$ K, is the *transition region*. It extends from $z \sim$ 1.5-3.0 Mm to $z \sim$ 2.5-3.5 Mm, depending

[2]When discussing regions above the photosphere in this thesis, the photosphere simply refers to $z = 0$.

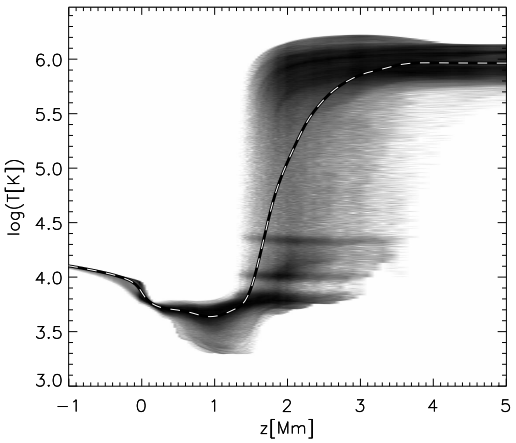

(a) Temperature in the Solar Atmosphere

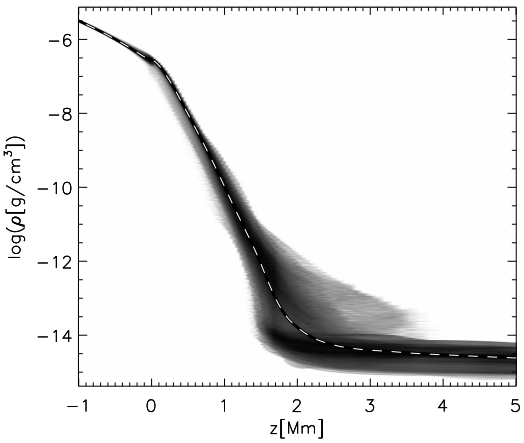

(b) Density in the Solar Atmosphere

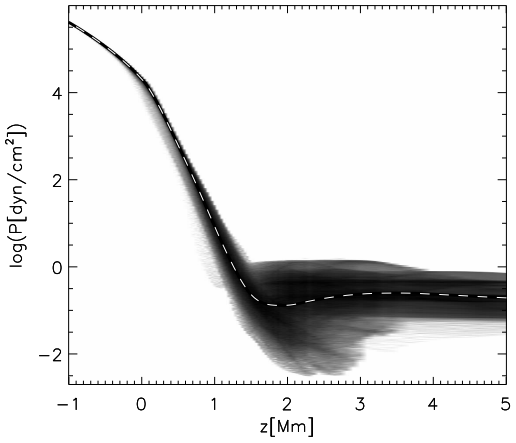

(c) Pressure in the Solar Atmosphere

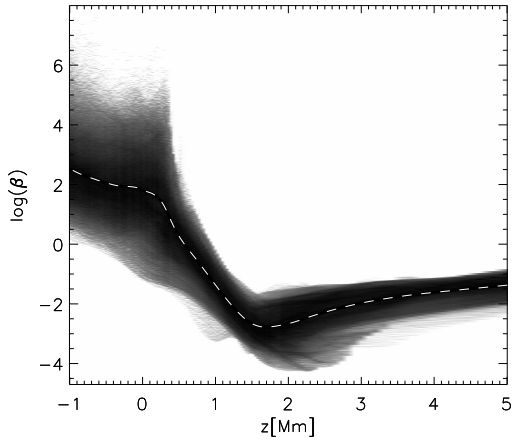

(d) Plasma β in the Solar Atmosphere

Figure 1.8: Histograms of temperature, density, pressure and plasma β as function of height in the solar atmosphere, obtained from a BIFROST simulation. The (negative) intensity in each histogram represents the log frequency of each specific value of the plotted variable at each specific height (hence histogram). Over-plotted is the horizontal averages of the same measures as function of height.

(again) on the local fluid dynamics. Finally, the outermost layer is the *corona*, which goes from $z \sim$ 2.5-3.5 Mm and outwards, characterized by a high and nearly constant temperature (of order 1 MK).

In addition to temperature, it is also interesting to study the *density* and the (gas) *pressure*. These two quantities are plotted in figure 1.8(b) and figure 1.8(c), respectively. Both quantities decrease with height. The decreasing pressure can be seen directly from the fact that the Solar Atmosphere is more or less in *hydrostatic equilibrium*,

$$\frac{\partial P}{\partial z} = -\rho g \tag{1.3}$$

Combining this with the ideal gas law, $P = \frac{\rho}{\overline{m}} kT$ while assuming a slowly varying temperature, which is mostly true except from the transition zone, we obtain the following equation

$$\frac{\partial \ln \rho}{\partial z} = -\frac{g\overline{m}}{kT}, \tag{1.4}$$

i.e. the density decreases with height. It is also easy to show that the density will decrease with height in the transition zone. Omitting the assumption of slowly varying temperature, we have

$$\frac{\partial \ln \rho}{\partial z} = -\frac{\partial \ln T}{\partial z} - \frac{g\overline{m}}{kT}, \tag{1.5}$$

and since the temperature in the transition zone increases with height, we will still have a negative right-hand side.

In the case of a slowly varying temperature, integrating eq. (1.4) over height gives

$$\rho = \rho_0 e^{-\frac{g\overline{m}}{kT}(z-z_0)} = \rho_0 e^{-\frac{z-z_0}{H_\rho}} \tag{1.6}$$

where H_ρ is the *density scale height*, defined as $H_\rho \equiv \left(\frac{\partial \ln \rho}{\partial z}\right)^{-1}$, i.e. the height you have to travel upwards before the density is reduced by a factor of e. When the temperature is only slowly varying, as in the chromosphere, the pressure will also follow a similar exponential function with a pressure scale height $H_P \equiv \left(\frac{\partial \ln P}{\partial z}\right)^{-1} = H_\rho = \frac{kT}{g\overline{m}}$. Using the solar surface gravitational acceleration $g = GM_\odot / R_\odot^2 = 2.74 \cdot 10^4$ cm/s^2, a typical chromospheric temperature $T = 6000$ K and a mean particle mass $m \sim m_H \sim 1.5 \cdot 10^{-27}$ g,[3] we get $H_\rho = H_p \sim 1 - 200$ km. We also get a similar estimate of the scale height by measuring the slope of the horizontally averaged pressure and density in the chromosphere in figures 1.8(b) and 1.8(c).

As mentioned earlier, the Sun has *magnetic fields*, which play an important role on the plasma in the atmosphere. Its presence might either decrease or increase the temperature significantly, depending on the field topology, as well as affecting the density and the large scale velocities in the fluid. A magnetic field $\mathbf{B}$ exerts a (magnetic) pressure on the surrounding fluid, similar to the gas pressure, given by

$$P_B = \frac{B^2}{2\mu} \tag{1.7}$$

[3]The hydrogen mass is $1.67 \cdot 10^{-27}$ g, but since a significant fraction of the particles are ionized, the abundance of free electrons leads to a (slightly) less mean particle mass, and therefore $1.5 \cdot 10^{-27}$ g is a good estimate here.

where μ is the vacuum permeability. Its gradient is the *magnetic pressure force* (per volume), $\nabla P_B = \frac{1}{\mu}\left[(\mathbf{B}\cdot\nabla)\,\mathbf{B} - (\nabla\times\mathbf{B})\times\mathbf{B}\right]$ where the first term is the *magnetic tension force*, and the second term is the *Lorentz force*, $\mathbf{j}\times\mathbf{B}$. We often want to know whether the fluid velocity fields are driven by the magnetic fields or the other way round. Therefore we define the *plasma* β, defined by $\beta = P/P_B$, i.e. the ratio between the gas pressure and the magnetic pressure. If $\beta >> 1$, the velocities in the plasma drives the magnetic field, but if $\beta << 1$, the magnetic fields drives the plasma velocities.

A histogram of the plasma β is shown in figure 1.8(d). Below the surface, in the convective layer, wee see that $\beta >> 1$. The magnetic fields are in fact generated by the turbulent velocities in the that region. In the photosphere and lower chromosphere, β is both above and below 1, so the magnetic fields are some places driven by the fluid velocities and other places the other way round. From the upper chromosphere and upwards, $\beta << 1$, so the plasma motions here are more or less driven by the magnetic fields.

In the solar atmosphere, we distinguish between *quiet Sun* (QS) regions and *active regions* (AR). Active regions are characterized by high magnetic activity, and the magnetic field is strong enough to modify the granulation (a photospheric pattern discussed later in this section). It features amongst other phenomena *sunspots* and *pores* where the magnetic field strength can reach up to 4000 G, *plage* where the plasma is acting turbulently and *flares* which are high energy bursts. The Quiet Sun, on the other hand, is characterized by weaker magnetic fields, and the magnetic field structure consists mainly of magnetic bright points organized in a magnetic *network* which comprises the pattern seen in chromospheric lines (a phenomenon called *supergranulation*, described briefly later in this section), as seen in figure 1.9.

1.2.3 Observations and Simulations of the Photosphere

This thesis focuses on the solar atmosphere, and it is therefore important to have some physical knowledge each region of the solar atmosphere in particular, from innermost to outermost. This section presents what we know about the photosphere, based on observations and numerical simulations.

If we look directly, or through an optical telescope, at the Sun, we see the *solar surface*, at $r = R_\odot$, which marks the bottom of the solar atmosphere. The surface is often defined as the layer where the optical depth for light with wavelength 5000 Å, as seen from space, equals 1. As already mentioned, the *photosphere* is located here, with a thickness of 1-200 km and characterized by a rapid temperature decrease from about 8000 K to 5-6000 K. The density in this region is about $2\cdot10^{-7}$ g/cm^3, and the pressure is about $2\cdot10^4\ \mathrm{dyn/cm^2}$.

The most important feature of the QS photosphere is the *granulation pattern*. In figure 1.10, this pattern is showed as a intensity plot of the continuum wavelengths in the visible spectrum, simulated with Bifrost. The pattern looks like a mosaic pattern as seen from above, composed of many cells fitting tightly together. These cells, known as *granules*, are in fact the top of (relatively small) convective cells in the upper convection zone, and they have a typical diameter of 700-1500 km. The "borders" which surrounds the cells, known as *intergranular lanes*, have a typical thickness of ~ 100 km. Up-flows of hotter gas (at velocities of 1-2 km/s) from the convection zone form the granule interiors in the photosphere. When this gas reaches the photosphere, it cools radiatively, decelerates and thereafter floats (at velocities of 2 km/s) along the surface towards the intergranular lanes. Finally,

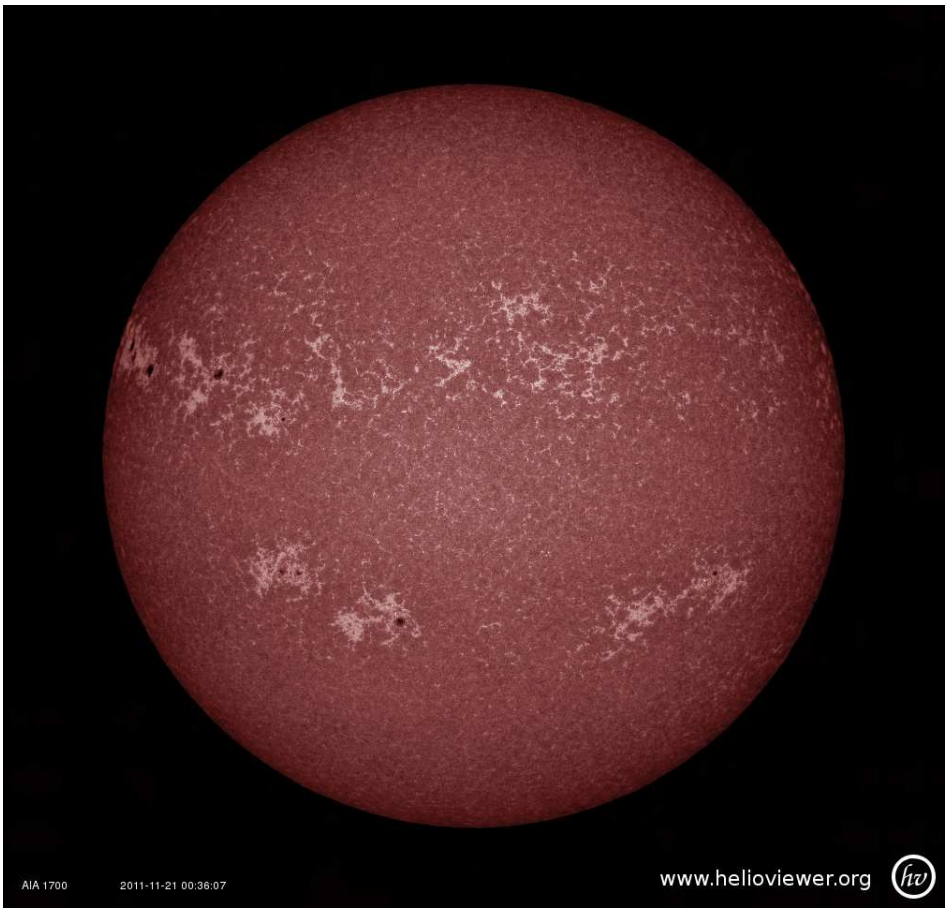

Figure 1.9: An image of the Sun, showing the chromospheric network (supergranulation) taken at Solar Dynamics Observatory (SDO) at continuum wavelength 1700 Å.

the gas becomes dense and cool enough to sink (at velocities of 4 km/s) along the lanes. Gas from 3-4 near-lying intergranular lanes comes together in the granular "vertices" and from there sink (almost) vertically in tubes with a typical thickness of ~ 100 km. Because of the high plasma β in the granules, the magnetic fields in the photosphere are concentrated in the intergranular lanes, while the magnetic fields in the granules are weaker. Since the underlying convective cells do not have uniform pressure, the cells are moving all the time. The average lifetime of one granule is $\sim$8 min, but some granules may live for up to 15 min (Priest 1982).

The photosphere also features cellular patterns similar to granulation but with larger cell structures, namely *mesogranulation* and *supergranulation*. Supergranulation was first observed by Hart (1954) as fluctuations in the velocity field on top of the mean rotational speed on the solar equator, and has later showed up in Dopplergrams, i.e. plots of the Doppler shifts on the solar surface, as a pattern similar to the granulation pattern but with cells that are $\sim$100 times as large. As summarized by Rieutord & Rincon (2010), this is (very briefly) what we know about supergranulation: supergranules have typical diameters of 10-30 Mm and typical lifetimes of 1.6 ± 0.7 days. The rms horizontal velocities on supergranular scales are $\sim$350 m/s, while the rms vertical velocities in the supergranular lanes are $\sim$30 m/s (which means that the upflows below the supergranules are slower than this, while the

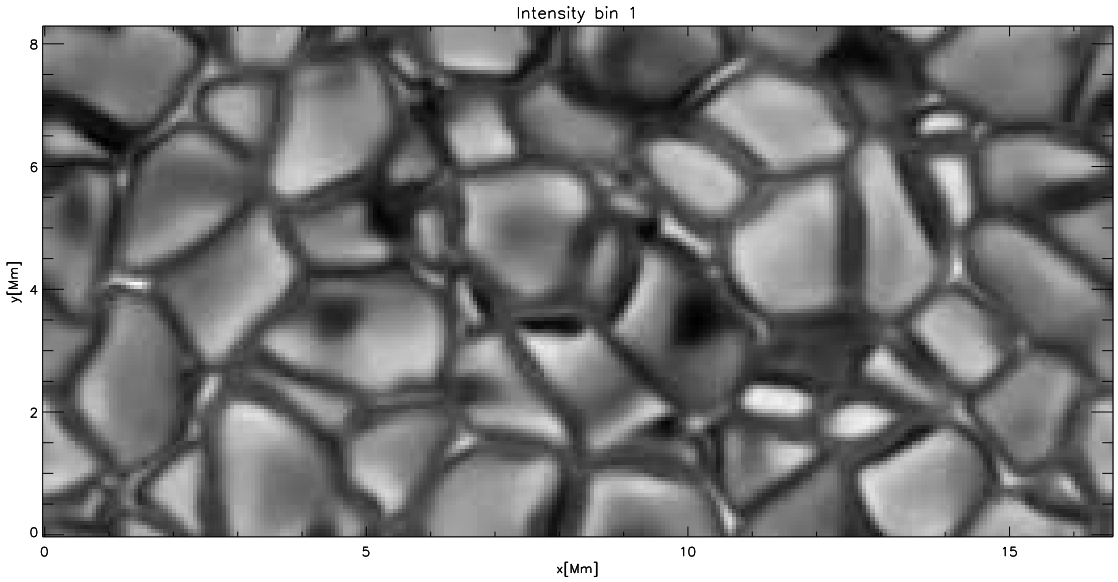

Figure 1.10: Simulated intensity plot of the continuum wavelengths in the visible specter, showing the granulation pattern in the photosphere.

downflows along the lanes are faster). Local helioseismology shows that supergranules are shallow structures with a depth of a few megameters. Several theories have been constructed about what causes supergranulation, but it seems most likely to be caused by large scale convection. In the chromosphere, supergranule boundaries show up in bright points, forming the chromospheric *network* in e.g. the Ca H and K lines, as shown in figure 1.9, which coincides with the QS magnetic network. The bright points in the network have field strengths of $\sim$1500-2000 G in the photosphere, while the regions inside the supergranules, known as the *internetwork*, has magnetic fields of $\sim$100 G (Socas-Navarro et al. 2004; Hasan et al. 2005; Wedemeyer-Böhm et al. 2009).

Mesogranulation was first observed by November et al. (1981) as a pattern of cellular flow with a spatial scale of 5-10 Mm, lifetime of $\sim$2 hours and rms vertical velocity amplitude of about 60 m/s. Recent works on this feature, e.g. Yelles Chaouche et al. (2011), state that there are no indications of convective flows at mesogranular scales. However, mesogranulation might be a result of a collective interaction between several granules.

Sunspots

A very important feature in the non-QS photosphere are *sunspots*. A sunspot is often circular of shape and consists of a central dark area known as the *umbra*, which is surrounded by a slightly brighter region known as *penumbra* as shown in figure 1.11 (where we also see the surrounding granulation pattern). According to Priest (1982), the umbra has a typical diameter of 10-20 000 km and a magnetic field which can reach up to magnitudes of about 4000 G. Because of this strong magnetic field, the magnetic pressure is also higher than in the QS, and therefore the gas pressure is lower in order to maintain pressure balance. Since the gas pressure is proportional to density and temperature, these two quantities are both lower in sunspots than in the QS. The typical temperature in a sunspot is

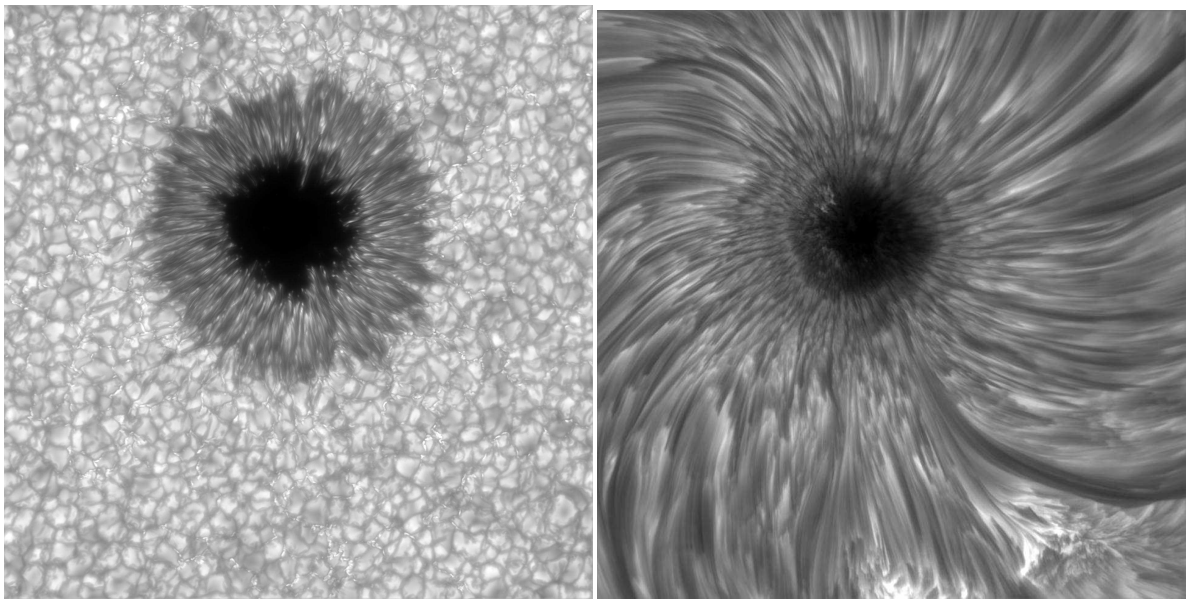

Figure 1.11: Two observational images of the same sunspot. Left panel is a photospheric image, showing how the sunspot "disturbs" the granulation pattern, taken at SST with an FWHM = 1 nm wide filter centered between the Ca H & K lines at 3954 Å. Right panel is a chromospheric image taken with CRISP in the line core of Hα.

3700 K, compared to the typical photospheric temperatures of 5-8000 K. This gives a radiative energy flux of only $1.2 \cdot 10^{10}\ \mathrm{erg\,cm^{-2}\,s^{-1}}$ which is about one fifth of the normal photospheric radiative flux. Since the density in sunspots is smaller than in the QS surface, the opacity is smaller as well, and therefore, when we look at a sunspot, we see deeper into the Sun than we do in the QS sun plasma. In other words, sunspots are cavities on the Solar surface.

Sunspots appear in active regions, usually as pairs with opposite polarities, where the strong magnetic field exits upwards from one sunspot, makes a loop and enters the companion sunspot. There are single sunspots as well, e.g. a sunspot where the magnetic field that exits the sunspot is spread into all directions and reenters the surface in smaller *pores*. Since the Sun rotates from east to west (as seen from Earth), we refer to the west-most sunspot in a sunspot pair as the *leading spot* or *p-spot* (preceding) and the east-most spot as the *following* or *f-spot*. The appearance of sunspots follows 11-year cycles which can be characterized by three (all empirical) rules, formulated by Hale & Nicholson (1938):

- *Hale-Nicholson's rule*: During one sunspot cycle, the majority of the leading sunspots on the northern hemisphere have the same polarity, while the leading sunspots on the southern hemisphere have the opposite polarity. In the next cycle, all polarities are reversed. This gives a *total magnetic cycle* on 22 years
- *Joy's rule*: The center of gravity of the leading sunspot tends to lie closer to the equator than the following sunspot
- *Spörer's rule*: Sunspot groups tend to emerge at progressively lower latitudes as a cycle progresses. The latter rule is demonstrated in figure 1.12 as a "butterfly diagram".

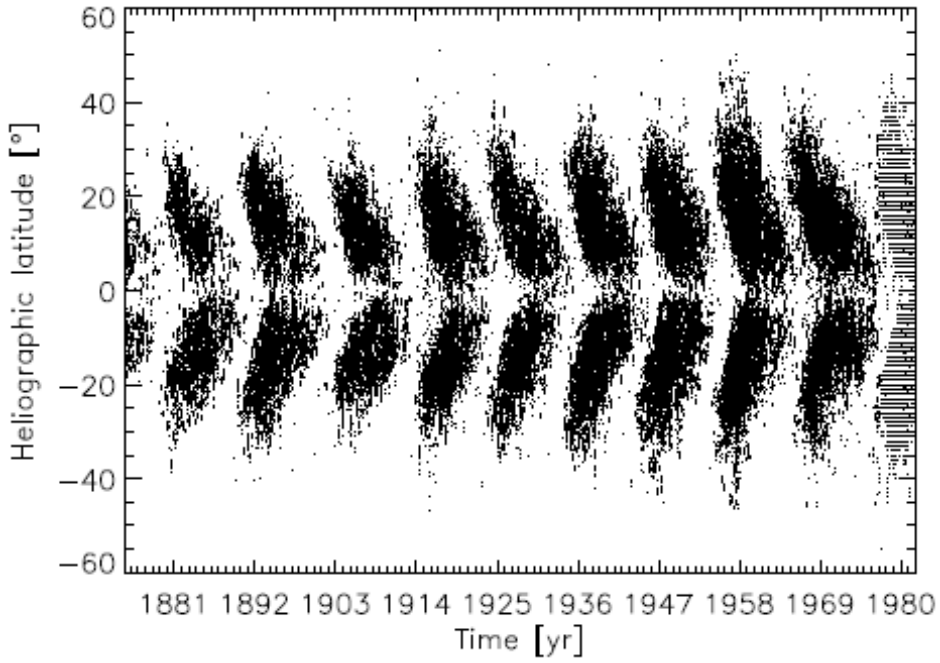

Figure 1.12: A "butterfly diagram" showing the appearances of sunspots as function of time and latitude, reprinted from Major (2004)

Magnetic Fields in the QS Photosphere

Magnetic fields also play an important role in the QS photosphere. Since the intergranular lanes, as well as the granules, are in constant motion, and since the foot-points of the magnetic fields which emerge from the surface are concentrated in the lanes, the magnetic foot-points are also shifted around on the surface. This can cause two initially vertical and parallel magnetic field lines to start twisting around each other (which causes a tangential discontinuity in the magnetic field known as a current sheet, which will be discussed later in this chapter), creating a vertically propagating Poynting flux which increases as the magnetic field lines are twisted further around each other. When the Poynting flux propagates upwards, it will reach into the corona in the form of twisted field lines. When the magnetic tension force, $(\mathbf{B} \cdot \nabla)\mathbf{B}$, in the twisted field lines becomes too high, the field lines will break and reconnect, and the energy which was stored in the twisted lines is transferred into thermal energy by dissipating currents into the surrounding medium. This rapid energy dissipation gives rise to a powerful energy burst known as a *nanoflare* (Parker 1988). This is one of the leading ideas for explaining the coronal heating.

1.2.4 Chromosphere

Above the photosphere lies the *chromosphere*, going from $z \sim$ 100-200 km to $z \sim$ 1.5-3.0 Mm (depending on the local fluid dynamics) with a temperature that varies slowly between 4000 K and 7000 K, but can reach below 2000 K in some extreme cases (Leenaarts et al. 2011). This atmospheric layer is transparent in the continuum of visible light, but can be studied in some spectral lines which

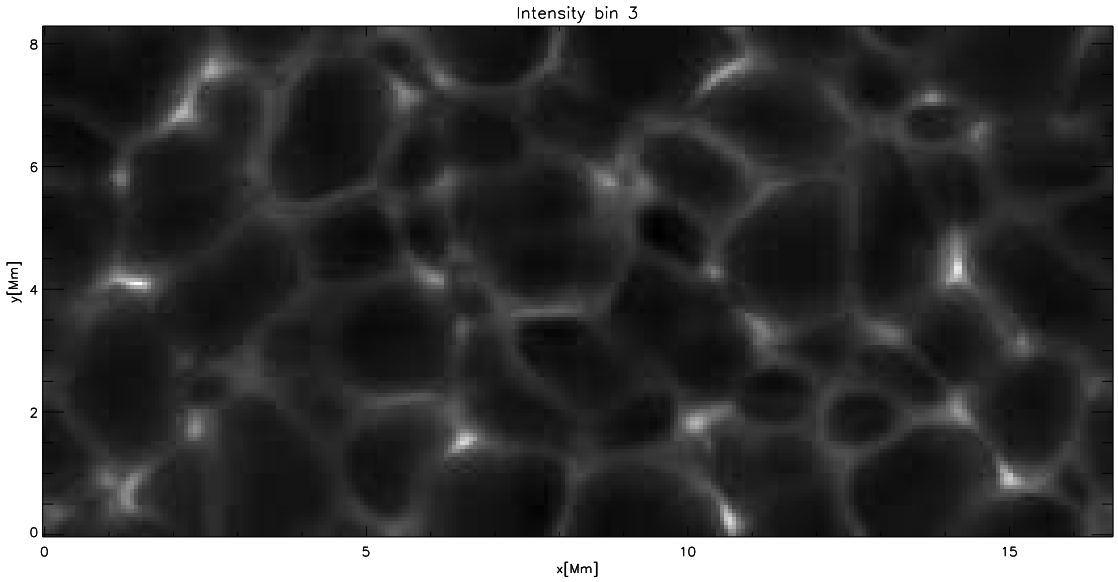

Figure 1.13: Simulated intensity plot of the wings of chromospheric lines, showing the reversed granulation pattern in the lower chromosphere.

are produced mainly in the chromosphere. Khokhlova (1959) states that the chromosphere is opaque enough at the center of the Ca II H and K lines that most of the radiation we obtain from these line centers are emitted in the chromosphere. Several scientists (Sotnikova 1978; Kneer & von Uexkuell 1985; Aquilano et al. 2003) have also used the Hα line as a source of information on the chromosphere. Studies of these lines has amongst other things revealed the chromospheric *network* (shown in figure 1.9) very clearly (Priest 1982). The lower chromosphere is also characterized by the *reversed granulation pattern*, shown in figure 1.13, which is an imprint of the underlying granulation pattern, but where the imprints of the granules is darker than the lanes. Several scientists have tried to find an explanation for this, and the most recent and plausible explanation, given by Cheung et al. (2007) based on theories which dates back to Nordlund (1984), states that the horizontally moving gas in the lower chromospheric region above a granule interior undergoes adiabatic expansion and radiative heating. The former decreases the temperature in the gas, while the latter increases it to a *radiative equilibrium temperature*, still lower than the temperature in the underlying granules. The gas in the region above an intergranular lane, on the other hand, undergoes adiabatic compression, because gas from both sides come together, increasing the temperature. Therefore, the temperature in the lower chromospheric region above an intergranular lane is hotter than the region above a granule interior, leading to a higher intensity in chromospheric lines along the intergranular lanes.

In the chromosphere, the scale heights for the density and for the pressure both stay at $\sim 100 - 200$ km. In the middle chromosphere, at $z \sim 1.0$ Mm, the plasma β is of order ~ 1, but as the gas pressure keeps decreasing rapidly with height while the magnetic pressure decreases more slowly, the plasma β hence decreases with height and is $<< 1$ in the upper chromosphere.

We can also gain physical knowledge about the chromopshere by studying limb features such as *prominences* and *spicules*. Prominences are located in the corona, but consists of plasma that has parameters comparable to those in the chromosphere (Galsgaard & Longbottom 1999), in other words,

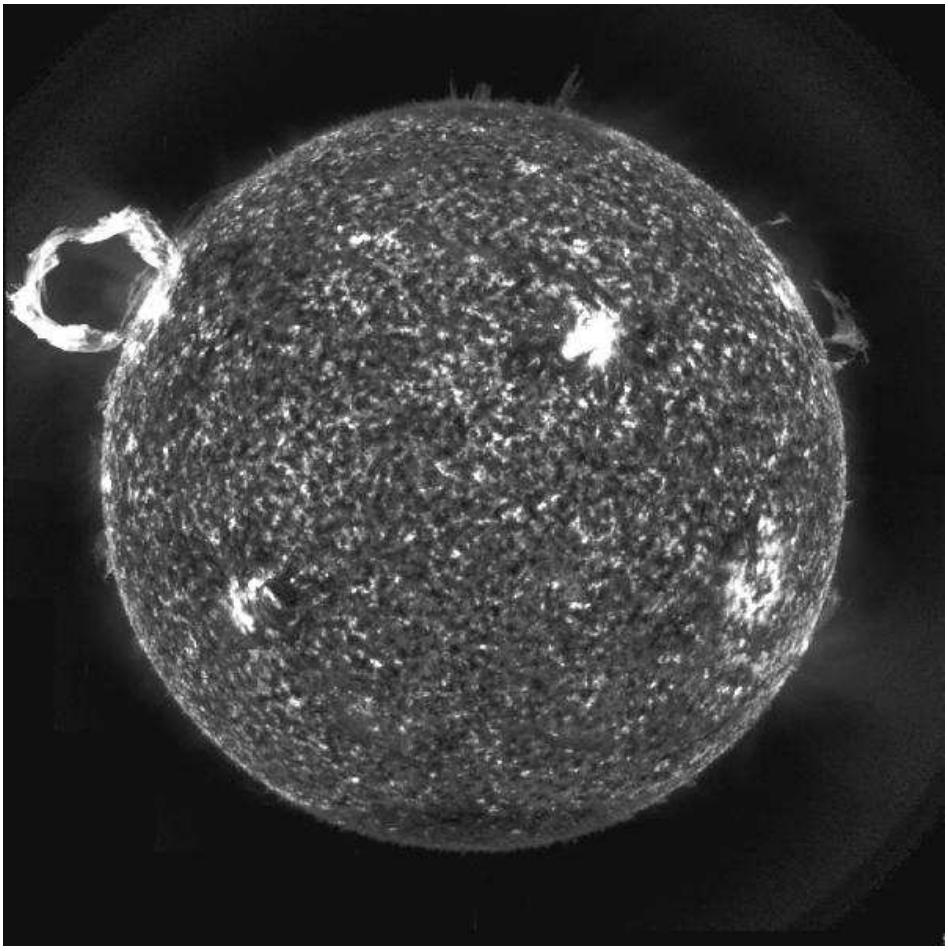

Figure 1.14: Image of a Sun including a large prominence, taken by the Atmospheric Imaging Assembly (AIA) at the Solar Dynamics Observatory (SDO) in the wavelength band centered at 304 Å.

they are extensions of the chromosphere into the corona. They can extend to heights over many thousands of kilometers, and the largest that has been observed has a height of 700 Mm. Figure 1.14 shows a prominence. Spicules are jets of plasma ejected from the chromospheric part of the QS network and reach velocities between 20 and 300 km/s and can reach up to coronal heights (5-10 000 km) before fading or falling down. We distinguish between two different kinds of spicules, namely *type I* and *type II* spicules. According to de Pontieu et al. (2007), type I spicules appear to rise up from the limb and fall back again. They have typical velocities of 10-40 km/s, lifetimes of 3-7 min and heights up to 5-6 Mm above the limb. These are created when photospheric oscillations and convective motions leak into the chromosphere along magnetic flux concentrations (e.g. the magnetic network) where they form shock waves that drive jets of plasma upwards (Hansteen et al. 2006). The same features exist on the solar disk where they are seen as *mottles* in the QS regions and *dynamic fibrils* in active regions, above *plage*, which are magnetic bright spots in the vicinity of sunspots. Type II spicules start with upward motion, but then fade rapidly instead of falling back, as seen in the Hinode Ca II H passband. They have typical velocities of 50-150 km/s and lifetimes of $\sim$10-100 s. Their typical heights can be up to 10 Mm in coronal holes, while they only reach 1-2 Mm in regions above AR plage and something in-between above the QS network. On the solar disk, a similar

feature is observed as rapid blue-ward excursions (RBEs) in the Ca II 8542 Å and Hα lines, according to Rouppe van der Voort et al. (2009). It is very likely that type II spicules and RBEs are due to magnetic reconnection, which may occur due to braiding of strong magnetic field lines. According to De Pontieu et al. (2009), type II spicules are likable to play a significant role in coronal heating and may represent the lowest lying nanoflares

1.2.5 Transition Region and Corona

Above the chromosphere is the narrow *transition region*, where the temperature jumps from about 10^4 K to 10^6 K. The height where this region occurs depends highly on the atmospheric feature and is highly dynamic in time. Examples are shown in figure 1.15, which shows the temperature profile in four selected columns in the modeled solar atmosphere. The height where $T = 10^5$ K varies from $z = 1.7$ Mm to $z = 2.3$ Mm, and the same result is also obtained while using data from all columns in the simulated atmosphere and computing the average and standard deviation of the height where $T = 10^5$. In all four columns used in figure 1.15, the temperature jumps from $3 \cdot 10^4$ K to $3 \cdot 10^5$ K in a height scale of $\sim 10 - 100$ km and from $3 \cdot 10^5$ K to $\sim 10^6$ K in a height scale of a few megameters. This wide span of heights where the transition region occurs explains why the transition region seemed much broader at the average temperature profile in figure 1.8(a). The density also changes rapidly in this region, but in the other direction: it decreases from 10^{-11} g/cm^3 to 10^{-15} g/cm^3. The pressure only decreases slightly. The transition region is mainly observed in extreme ultraviolet(EUV) emission lines from He II, C III, C IV, O III, O IV and O VI, since this region is where the temperature is high enough for the above-mentioned ionized states to be dominant (Feldman et al. 2010).

The outermost layer of the solar atmosphere is known as the *corona*, which comes from Greek and means crown. Originally, this layer was only seen during a solar eclipse, where one could see it as a white crown surrounding the darkened solar disk. Nowadays, coronagraphs are used, i.e. telescopes with a small occulting disc that creates an artificial solar eclipse for the observer, making the corona viewable. The solar corona can also be viewed directly in *soft X-rays*, because the contribution to this radiation from the lower atmosphere is negligible (Priest 1982). The temperature in the corona is more than 1 MK, and the density is of order 10^{-15} g/cm^3. These facts bring us to the problem dealt with in this thesis, *the coronal heating problem*.

Finally, before going into the problem of this thesis, I have reprinted a two-dimensional sketch of the QS atmosphere from Wedemeyer-Böhm et al. (2009), see figure 1.16. It includes both granulation and supergranulation as well as the magnetic network which coincides with the supergranular lanes. The magnetic field lines are plotted by solid lines, and fields from neighbouring supergranular lanes come together and form a *canopy*. Magnetic fields with foot-points in the internetwork are plotted with dashed lines and forms small canopies as well. This is a very simplified illustration, and the structure of the QS atmosphere becomes much more complicated in three dimensions, but the magnetic structure will still include a canopy above each supergranule. The figure also illustrates where features like spicules and fibrils are generated.

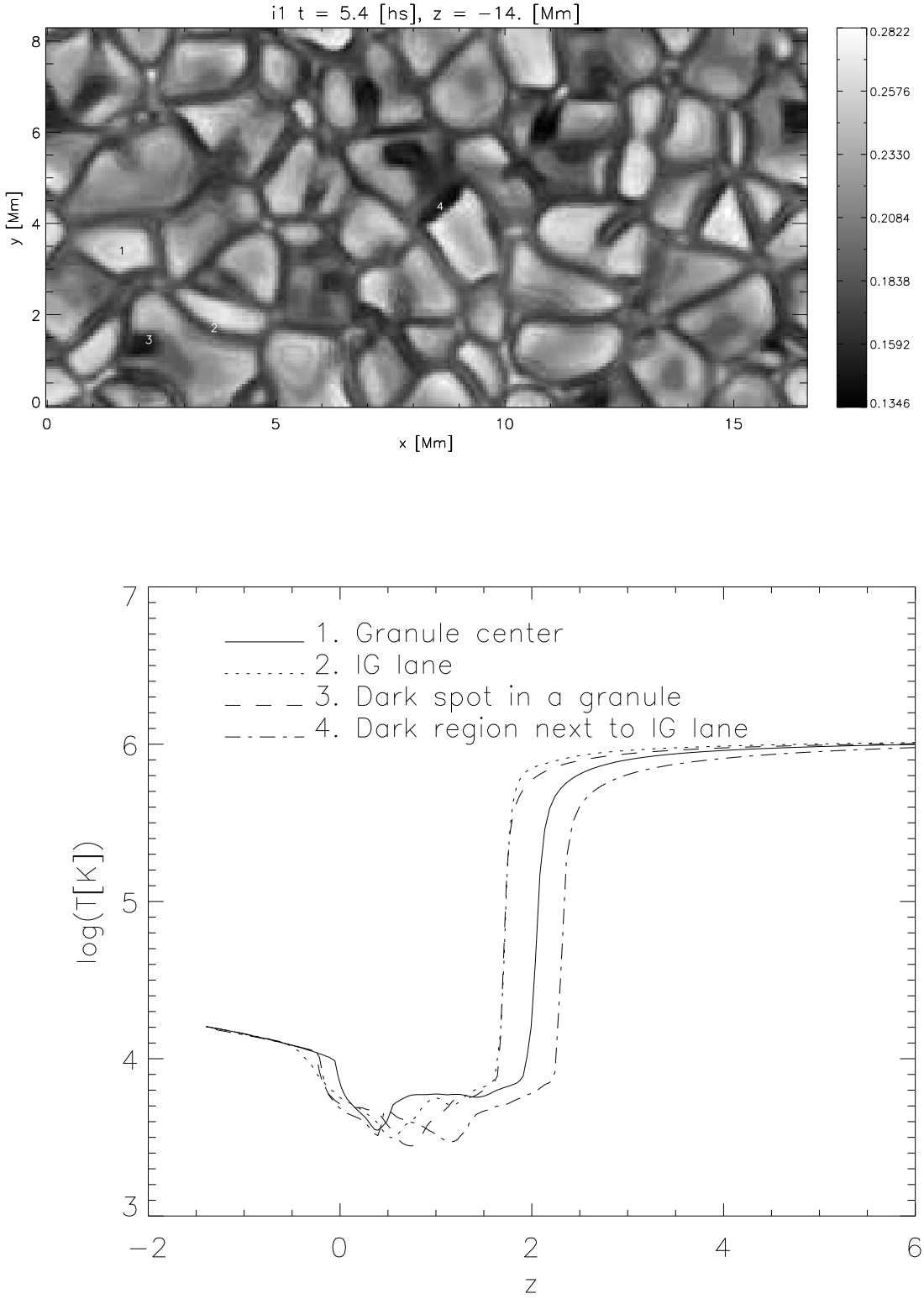

Figure 1.15: Temperature as function of height in 4 different columns in a numerical model of the Solar Atmosphere, simulated with Bifrost, showing the different heights (in Mm) where the transition region occurs. The figure indicates what region in the photosphere each column is located around, even though there is probably no 1-1 connection between that and the height of the transition region. Upper panel shows an intensity plot of the photosphere, where the numbers shows where each of the for columns lies.

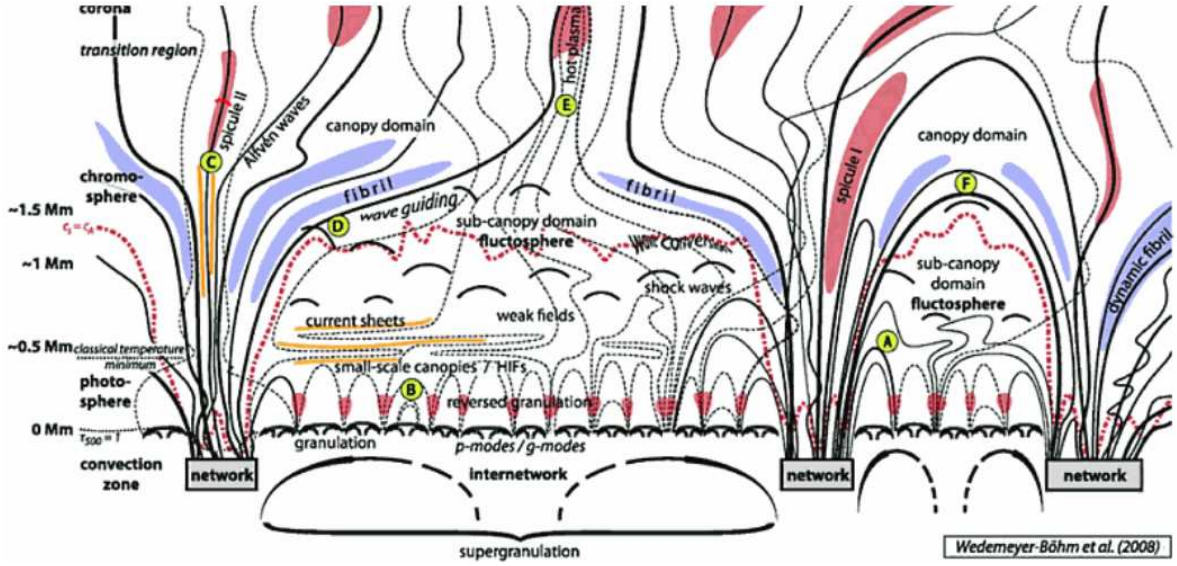

Figure 1.16: A two-dimensional sketch of the quiet-Sun atmosphere, reprinted from Wedemeyer-Böhm et al. (2009).

1.3 The Coronal Heating Problem

To understand the mechanism that heats the corona up to more than 1 MK is a problem that has puzzled astronomers for more than sixty years. Several theories have been suggested and dismissed, a few plausible models remain under scrutiny.

One traditional model suggests that the convection in the convection zone produces sound waves, gravitational waves and magnetohydrodynamic (MHD) waves which propagates upwards and dissipate their energy into the overlying atmospheric layers. It has been concluded that only Alfvén waves can reach up to the corona, while the other waves are dissipated and/or refracted before they reach that far (Parker 1988).

Another theory which has been suggested by Parker (1988) is based on the idea that the (X-ray) corona is a superposition of a large number of *nanoflares*, which are tiny and intermittent impulsive bursts of energy. Parker suggests here that nanoflares are generated this way: Convective motion at the bottom of the photosphere shuffles the magnetic foot-points around. This may cause two near-lying magnetic field lines which originally was vertical to twist around each other. Tangential discontinuities will then occur between neighbouring field lines, which generates current sheets (Galsgaard & Nordlund 1996). The strength of the current sheets increases with time until the stressing of the twisted magnetic field is high enough (just like a rubber band which is twisted too much) to cause the twisted field lines to "break" and reconnect, releasing an impulsive burst of energy, which is the nanoflare. The stressing of the magnetic field which eventually bursts out in a nanoflare occurs within widths comparable to the diffusion length, which in the solar photosphere is of order 10 m (de Wijn et al. 2009). This mechanism for coronal heating has been a promising candidate, but according to Aschwanden & Charbonneau (2002), it seems that the energy dissipated in the observed distribution of microflares and nanoflares is too small to be the dominating component. In both observations and simulations, however, we are restricted to a lower cutoff nanoflare energy, and when increased technology allows

us to see nanoflares at even lower energies, we might see a significant increase of the heat input from this mechanism.

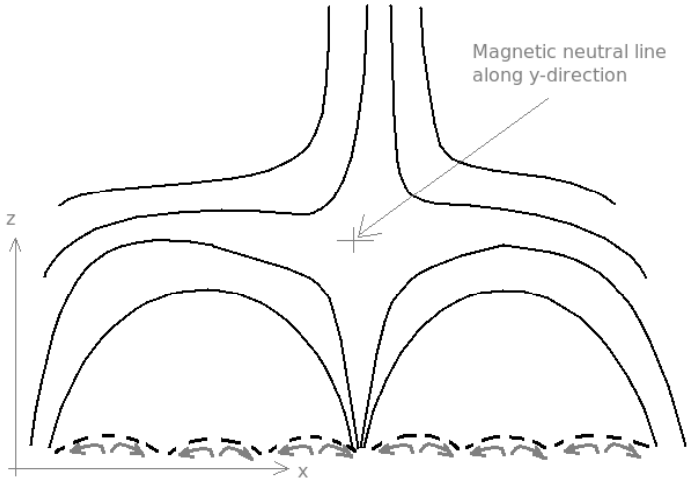

Figure 1.17: An xz-outcut of a possible magnetic field configuration in the QS atmosphere, showing a magnetic neutral point. The field is initially uniform in the y-direction.

A third plausible candidate for the coronal heating is a hierarchy of *current sheets*. According to Priest (1982), a current sheet is a tangential discontinuity in the magnetic field i.e. a non-propagating boundary between two fluids, where the magnetic field on each side of boundary is tangential to the boundary, but may be oriented in different directions and/or have different magnitude, generating a current density $\mathbf{j} = \nabla \times \mathbf{B}/\mu$. Current sheets are created in several ways in the solar atmosphere:

1) When the magnetic field is stressed due to convective motions, it collapses into tiny current sheet (width of order 10 m), which eventually burst out in a nanoflare, as discussed earlier.

2) When topologically separate parts of a magnetic configuration are pushed together (by the fluid motion), this causes large gradients in the magnetic field which leads to the generation of a current sheet, which in this case may extend over several megameters. If this happens in an evolving AR field, a *solar flare* can be generated

3) When discontinuities arise near a magnetic neutral point/line, current sheets can be generated nearby this point/line (which can extend over several megameters). As an example, consider a magnetic field in the xz-plane as shown in figure 1.17, which is initially uniform in y-direction. It features a magnetic neutral line, marked by the "+" symbol, along the y-direction. On the different sides of the line, the fluid might have different motions which might push the magnetic field in different ways, so the magnetic field on opposite sides of the neutral line will be tilted in different directions. This give rise to tangential discontinuities in the magnetic fields, i.e. current sheet generation.

Galsgaard & Nordlund (1996) state that the formation of current sheets causes magnetic reconnection which drives supersonic and super-Alfvénic jet flows, which further causes generation of smaller-scale current sheets. This "hierarchy" of current sheets extends to ever smaller size as the numerical resolution increases, i.e. there might be large amounts of current sheets even thinner than the smallest

(numerical and/or observational) resolution used in models today which still needs to be discovered. Therefore, the hierarchy of current sheets is a possible candidate for the coronal heating.

Gudiksen & Nordlund (2005) used numerical simulations to show that moving the foot-points of the magnetic field in a way consistent with the observed photospheric velocity fields leads to a heat input in the corona that is within the observational limits. The simulations did not deal directly with nanoflares, but rather an *ab initio* approach to the coronal heating, using only observed facts, such as the observed average velocity field and realistic magnetic fields in the photosphere, to compute the heat input dissipated by this mechanism. Nanoflares *are* an effect of moving magnetic foot-points around in the photosphere, but even though nanoflares might not dissipate enough heat into the corona to account for the entire coronal heating, the mechanism of shuffling magnetic foot-points might cause other effects which together with nanoflares dissipate a sufficient amount of heat into the corona. The exact amount of heat which is dissipated into the corona by moving the magnetic foot-points around in the photosphere will depend on how complex the structure of the photospheric magnetic field is.

1.3.1 The Aim of this Thesis

The aim of this thesis is to study atmospheric models with different magnetic field configurations in the photosphere to see how this affects the heating of the corona. The models that are studied represent regions in the QS atmosphere located along the photospheric internetwork, where the average magnetic field strength (in the photosphere) is of order 100 G. The magnetic fields in the photospheric internetwork are concentrated in the intergranular lanes (where the fields can be more than 1 kG of magnitude) and probably organized a pattern of upward- or downward-oriented fields spread randomly along the pattern of intergranular lanes (Socas-Navarro et al. 2004; Hasan et al. 2005; Wedemeyer-Böhm et al. 2009). This pattern of upward- and downward-oriented fields are often referred to as a magnetic “salt-pepper pattern” (where the salts are the downward fields, while the peppers are the upward fields). In this thesis will deal with different kinds of salt-pepper patterns in order to find a correlation between the complexity of the photospheric magnetic field and the amount and location of heat dissipated into the corona.

2

MODEL

In order to study the coronal heating and its dependence of the magnetic field structure in the solar atmosphere, we solve the MHD equations numerically for a cube of solar atmosphere using the Bifrost code, described in details by Gudiksen et al. (2011). We write the MHD equations as

$$\frac{\partial \rho}{\partial t} = -\nabla \cdot \rho \mathbf{u} \tag{2.1}$$

$$\frac{\partial \rho \mathbf{u}}{\partial t} = -\nabla \cdot (\rho \mathbf{u}\mathbf{u} - \tau) - \nabla P + \mathbf{J} \times \mathbf{B} + \rho \mathbf{g} \tag{2.2}$$

$$\mu \mathbf{J} = \nabla \times \mathbf{B} \tag{2.3}$$

$$\mathbf{E} = \eta \mathbf{J} - \mathbf{u} \times \mathbf{B} \tag{2.4}$$

$$\frac{\partial \mathbf{B}}{\partial t} = -\nabla \times \mathbf{E} \tag{2.5}$$

$$\frac{\partial e}{\partial t} = -\nabla \cdot e\mathbf{u} - P \nabla \cdot \mathbf{u} + Q \tag{2.6}$$

where $\rho, \mathbf{u}, e$ and $\mathbf{B}$ are the density, the fluid velocity, the internal energy and the magnetic flux density, respectively. $\tau, P, \mathbf{J}, \mathbf{g}, \mu, \mathbf{E}, \eta$ and Q are the stress tensor, the gas pressure, the current density, the gravitational acceleration, the vacuum permeability, the electric field strength, the magnetic diffusivity and the heat input. The latter quantity usually contains several terms, e.g. Joule dissipation, viscous dissipation, heating from Spitzer conduction and a radiative heating/cooling.

In addition to the MHD equations, the temperature T and pressure P is related to the internal energy e and density ρ by an *equation of state* (EOS). A typical EOS is the *ideal gas law*, $P = \frac{\rho k_B T}{\bar{m}}$, where T is related to e and ρ with the equation $e = \frac{3}{2}\frac{\rho k_B T}{\bar{m}}$. The ideal gas law is only completely valid for a gas of randomly-moving non-interacting particles. It is a good approximation for relatively high temperatures and lower densities (lower pressure), but it fails for dense and cool gases where interaction forces and molecular size become important. The ideal gas law is generally not valid in the solar atmosphere, because the gas have *internal degrees of freedom*, and in the models studied in this thesis, *EOS tables* are used instead to compute T and P from e and ρ. The EOS tables are generated with the Uppsala Opacity Package (Gustafsson et al. 1975). To calculate atomic level populations, the table generator assumes *local thermodynamic equilibrium* (LTE). LTE is a condition which includes several assumptions, but in few words it means that the state of the gas (i.e. ionization degree, populations of the different excited states of each chemical element) can be described by

only e (and ρ). Perfect LTE requires *detailed balance* i.e. each atomic reaction which takes place is balanced by the exact opposite reaction, e.g. a specific photo-excitation of an atom have to be balanced by the corresponding deexcitation. In the convection zone, photosphere and chromosphere, LTE is a good to middling approximation. In the corona, on the other hand, LTE is not valid, so the state of the gas must be described by *rate equations* for each excited state of each element. However, the calculation of the state of the coronal gas is simplified by the following fact: all upward transitions in an atom (ionization, excitation) are (approximately) due to collisions, while all downward transitions are due to radiation. To satisfy detailed balance, collisional ionization has therefore to be balanced by radiative recombination, and collisional excitation has to be balanced by spontaneous deexcitation.

Bifrost is built on several generations of previous numerical codes, amongst other the (Copenhagen) Stagger Code (Nordlund & Galsgaard 1995) and Oslo Stagger Code (Martínez-Sykora et al. 2008, 2009). The main improvement from the older Stagger codes to Bifrost is that instead of requiring shared memory architecture (a system of multiple processors which have access to one large block of memory) as the older codes did, Bifrost is an MPI (Message Passing Interface) parallel code able to run on distributed memory architecture (a system where each processor has its own private memory).

2.1 Spatial Discretization, Staggered Mesh

To discretize the spatial derivatives which occurs at the right-hand sides of the MHD equations, Bifrost applies a sixth order accurate method, which calculates the partial derivative of a function by using the three nearest neighbor points on each side. Starting at one specific point, applying the derivative operator will shift the evaluation point a half grid length in the direction we differentiate with respect to. The two possible shift directions and three spatial dimensions gives us 6 different derivative operators, $\partial^{\pm}_{[xyz]}\left(f(x,y,z)\right)$. E.g. the operator which returns the derivative of f with respect to x, shifted a half-step *forward* in the x direction, is given by

$$\partial^{+}_{x}(f_{i,j,k}) = f'_{i+\frac{1}{2},j,k} = \tag{2.7}$$

$$\frac{a}{\Delta x}(f_{i+1,j,k} - f_{i,j,k}) + \frac{b}{\Delta x}(f_{i+2,j,k} - f_{i-1,j,k}) + \frac{c}{\Delta x}(f_{i+3,j,k} - f_{i-2,j,k}), \tag{2.8}$$

$$a = \frac{1}{2} - b - c, \quad b = -\frac{1}{16} - 3c, \quad c = \frac{3}{256}, \tag{2.9}$$

while the operator which calculates the derivative a half-step *backward* in the x direction is given by

$$\partial^{-}_{x}(f_{i,j,k}) = f'_{i-\frac{1}{2},j,k} = \tag{2.10}$$

$$\frac{a}{\Delta x}(f_{i,j,k} - f_{i-1,j,k}) + \frac{b}{\Delta x}(f_{i+1,j,k} - f_{i-2,j,k}) + \frac{c}{\Delta x}(f_{i+2,j,k} - f_{i-3,j,k}). \tag{2.11}$$

$$\tag{2.12}$$

Because of the half-point shifts which the derivative operators cause, we will also need six corresponding interpolation operators, $T^{\pm}_{[xyz]}$. E.g. the interpolation that shifts the evaluation point a half-step

forward in the x direction is given by

$$T_x^+(f_{i,j,k}) = f_{i+\frac{1}{2},j,k} = \tag{2.13}$$

$$a(f_{i,j,k} + f_{i+1,j,k}) + b(f_{i-1,j,k} + f_{i+2,j,k}) + c(f_{i-2,j,k} + f_{i+3,j,k}) \tag{2.14}$$

$$a = 1 - 3b + 5c, \quad b = -\frac{1}{24} - 5c, \quad c = \frac{3}{640} \tag{2.15}$$

while the interpolation that shifts the evaluation point a half-step backward in the x direction is given by

$$T_x^-(f_{i,j,k}) = f_{i-\frac{1}{2},j,k} = \tag{2.16}$$

$$a(f_{i-1,j,k} + f_{i,j,k}) + b(f_{i-2,j,k} + f_{i+1,j,k}) + c(f_{i-3,j,k} + f_{i+2,j,k}). \tag{2.17}$$

$$\tag{2.18}$$

As mentioned, Bifrost applies a *staggered mesh*. This means the following: For each cube in the three-dimensional Cartesian grid, we choose the location of the evaluation points for the different variables at strategic points at the cube in such a way that minimizes the need for interpolating. Therefore ρ and e are volume centered, **B** and ρ**u** are face centered, and **E** and **J** are edge centered, as shown in figure 2.1 (Nordlund & Galsgaard 1995).

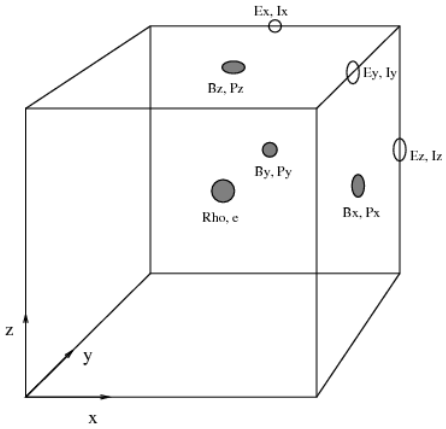

Figure 2.1: Sketch of the staggered mesh, reprinted from Nordlund & Galsgaard (1995). `Px, Py, Pz` are here the components of ρ**u**, and `Ix, Iy, Iz` the components of **J**.

2.2 Artificial Diffusion

With numerical approximations come different kinds of approximation errors. Some of these errors can be magnified for each timestep, and need to be *diffused* away in order to maintain a stable simulation . Therefore, we need to include *artificial diffusion* terms on the right-hand sides of equations (2.1)-(2.6). In general, a variable $a(x,t)$ (using only one dimension for simplicity) should have a differential equation on the form

$$\frac{\partial a}{\partial t} = f(x,t) + \frac{\partial}{\partial x}\left(D\frac{\partial a}{\partial x}\right), \tag{2.19}$$

where the first term on the right-hand side is the normal right-hand side of the differential equation (including spatial derivatives) while the second term is the diffusive term. The diffusion coefficient D is then defined in a way so it is large when the fluid acts in a way which might cause numerical errors which increase in time, and otherwise small. In order to ensure this, the diffusion coefficient must consist of several terms, which we will have a look at in the next paragraphs.

One case where the truncation error grows rapidly in time is when a variable consists of variations with wave-numbers near the Nyqvist wavenumber, $k \sim k_N = \pi/\Delta x$, because the numerical propagation speed of these waves decreases as k approaches k_N, which gives rise to phase errors. Therefore, the diffusion coefficient consists of a *wave viscosity* term on the form $\nu_1 c_f$ where $c_f = \sqrt{\frac{B^2+\gamma P}{\rho}}$ is the speed of fast mode waves, and ν_1 is of order 0.1. Thus, the diffusion coefficient increases when very fast propagating waves arise. Since the phase error is large for wave-numbers near the k_N and negligible for smaller wave-numbers, we want the diffusive term to scale with the wavenumber. If we use second order diffusive terms, the damping length for waves scales as k^{-2}, giving a wave diffusion which, according to Nordlund & Galsgaard (1995), does not increase significantly with the wavenumber. It can be shown that the next possible diffusive term that behaves qualitatively correct is a fourth order diffusion operator. This gives a wave damping length which scales as k^{-4}, which ensures waves with wave-numbers near k_N to die out rapidly while waves with smaller wave-numbers, which have negligible phase errors, can survive for longer times. In order to have a fourth order diffusive term, it is necessary to include a factor in the diffusion coefficient which scales with the third order spatial derivatives, and therefore a *quenching operator* is included, discussed later in this section.

A second case which gives rise to numerical errors which grow in time is when physical properties are advected with high velocities. To keep this advection stable, it is therefore necessary to include an *advective viscosity* on the form $\nu_2|\mathbf{u}|$, where ν_2 is of order 0.5. This term is also multiplied by the quenching operator in the expression for the diffusion coefficient, because the advection is generally stable when the variations of the physical quantities in the fluid are of small wave-numbers, while variations of larger wave-numbers can more easily make high-velocity advection unstable.

A third case which might cause numerical errors to grow is when shocks occur, especially when the shock front has a width comparable to the numerical grid size. To make sure that the shocks are numerically resolvable, we include a *shock viscosity* term, $\nu_3|\nabla_x^1 u_x|_-$, where ν_3 is of order 1.0. ∇_x^1 denotes a first order gradient in the x-direction, and $|\ldots|_-$ denotes the absolute value of the $negative$ contributions. In other words, the shock viscosity scales as the negative contributions to the velocity gradients. This is because shock fronts always have large negative gradients, since the velocity gradient in a shock front points in opposite direction of the direction which the shock propagates. In this way, numerically unresolvable shocks will be heavily diffused until the width of the shock front is larger than a few grid zones.

As already discussed, it is desirable to include a factor in the diffusion coefficient which scales with the third order derivatives. Therefore, a *quenching operator* is introduced, defined by

$$Q_x(g) = \max_{x\pm1}\left(\frac{|\Delta_x^2 g|}{|g| + \frac{1}{q_{\max}}|\Delta_x^2 g|}\right), \tag{2.20}$$

where Δ_x^2 denotes a second order difference (proportional to a second derivative) between neighboring points in the x-direction, and $\max_{x\pm1}$ denotes the maximum over the three nearest grid points.

The factor which is put into the diffusion coefficient is given by $Q_x\left(\frac{\partial a}{\partial x}\right)$, which scales as the third derivative, going to 1 as the third derivative goes to zero and going to the maximum quenching number $q_{\max}$ as the third derivative gets big. In Bifrost, we use $q_{\max} = 8$.

Putting all the terms discussed above together, the continuity equation (2.1) in one dimension with a diffusive term is given by

$$\frac{\partial \rho}{\partial t} = -\frac{\partial}{\partial x}(\rho u_x) + \frac{\partial}{\partial x}\left[\nu_\rho \Delta x \left(\nu_1 c_f + \nu_2 |\mathbf{u}| + \nu_3 |\Delta_x^1 u_x|_-\right) Q_x\left(\frac{\partial \rho}{\partial x}\right)\frac{\partial \rho}{\partial x}\right] \tag{2.21}$$

where ν_ρ is a coefficient which scales the total mass diffusion, usually of order 0.1. For three dimensions, we add similar diffusive terms where we the x's are replaced by y's and z's. The diffusive terms in the energy equation (2.6) are very similar. The x-component of the momentum equation (2.2) with the diffusive terms (I now take into account all three dimensions because of the cross-terms between the different dimensions) is given by

$$\begin{aligned}\frac{\partial(\rho u_x)}{\partial t} =& \frac{\partial}{\partial x}\left(\tau_{xx} - \rho u_x^2 - P\right) + \frac{\partial}{\partial y}\left(\tau_{xy} - \rho u_x u_y\right) + \frac{\partial}{\partial z}\left(\tau_{xz} - \rho u_x u_z\right) \\ &+ (\mathbf{J}\times\mathbf{B})_x + \rho g_x\end{aligned} \tag{2.22}$$

where

$$\tau_{ij} = \begin{cases} \rho \Delta x_i \left(\nu_1 c_f + \nu_2 |\mathbf{u}| + \nu_3 |\Delta_i^1 u_i|_-\right) Q_i\left(\frac{\partial u_i}{\partial x_i}\right)\frac{\partial u_i}{\partial x_i}\ , & i = j \\ \left.\begin{array}{l}\rho\Big[\Delta x_i \left(\nu_1 c_f + \nu_2 |\mathbf{u}| + \nu_3 |\Delta_i^1 u_i|_-\right) Q_i\left(\frac{\partial u_j}{\partial x_i}\right)\frac{\partial u_j}{\partial x_i} \\ + \Delta x_j \left(\nu_1 c_f + \nu_2 |\mathbf{u}| + \nu_3 |\Delta_j^1 u_j|_-\right) Q_j\left(\frac{\partial u_i}{\partial x_j}\right)\frac{\partial u_i}{\partial x_j}\Big]\end{array}\right\} & i \neq j \end{cases} \tag{2.23}$$

for the i-th and j-th dimension.

We also have magnetic diffusion, which (in x-direction) consists of the following two terms

$$\eta_x^{(1)} = \frac{\Delta x}{Pr_{\mathrm{M}}}(\nu_1 c_f + \nu_2 |\mathbf{u_x}|) \tag{2.24}$$

$$\eta_x^{(2)} = \nu_3 \frac{\Delta x^2}{Pr_{\mathrm{M}}} |\nabla_\perp \cdot \mathbf{u}|_- \tag{2.25}$$

where Pr_{M} is the magnetic Prandtl number, that scales the ratio of viscous to magnetic hyperdiffusion. Here, $\nabla_\perp \cdot \mathbf{u}$ means the divergence of the component of the velocity which is perpendicular to the magnetic field. The diffusion terms are put into the resistive part of the electric field in equation (2.4):

$$E_x^{(\eta)} = \left\{\frac{1}{2}\left(\eta_y^{(1)} q_y(J_x) + \eta_z^{(1)} q_z(J_x)\right) + \frac{1}{2}\left(\eta_y^{(2)} + \eta_z^{(2)}\right)\right\} J_x \tag{2.26}$$

$$E_y^{(\eta)} = \left\{\frac{1}{2}\left(\eta_z^{(1)} q_z(J_y) + \eta_x^{(1)} q_x(J_y)\right) + \frac{1}{2}\left(\eta_z^{(2)} + \eta_x^{(2)}\right)\right\} J_y \tag{2.27}$$

$$E_z^{(\eta)} = \left\{\frac{1}{2}\left(\eta_x^{(1)} q_x(J_z) + \eta_y^{(1)} q_y(J_z)\right) + \frac{1}{2}\left(\eta_x^{(2)} + \eta_y^{(2)}\right)\right\} J_z \tag{2.28}$$

2.3 Time Stepping

Equipped with the necessary diffusive terms in addition to the derivative and interpolation operators for the staggered mesh, we are ready to do the time stepping, the left-hand side of the MHD equations. In Bifrost, this can be done two ways: A third-order Runge-Kutta method or a third-order Hyman method. In this project, we use the Hyman method, described by Hyman (1979). It is a third order predictor-corrector scheme modified for variable time steps. Starting with

$$\frac{\partial f}{\partial t} = F\left(t, f(t)\right), \tag{2.29}$$

where $F\left(t, f(t)\right)$ is the right-hand side of one of the PDE's, solved with the derivative and interpolation operators described in section 2.1, the predictor step is given by

$$f_{n+1}^{(*)} = a_1 f_{n-1} + (1 - a_1) f_n + b_1 F_n \tag{2.30}$$

Then we calculate the right-hand sides of the PDE's again by using the "predicted" solutions $f_{n+1}^{(*)}$, and we use the results $F_{n+1}^{(*)}$ to do the corrector step, given by

$$f_{n+1} = a_2 f_{n-1} + (1 - a_2) f_n + b_2 F_n + c_2 F_{n+1}^{(*)} \tag{2.31}$$

where

$$a_1 = r^2 \tag{2.32}$$
$$b_1 = \Delta t_{n+1/2}(1 + r) \tag{2.33}$$
$$a_2 = 2(1 + r)/(2 + 3r) \tag{2.34}$$
$$b_2 = \Delta t_{n+1/2}(1 + r^2)/(2 + 3r) \tag{2.35}$$
$$c_2 = \Delta t_{n+1/2}(1 + r)/(2 + 3r) \tag{2.36}$$
$$r = \Delta t_{n+1/2}/\Delta t_{n-1/2} \tag{2.37}$$
$$t_n = t_{n-1} + \Delta t_{n-1/2}, \quad t_{n+1} = t_n + \Delta t_{n+1/2} \tag{2.38}$$

Finally, the length of the time-step itself is determined by several limitations. First, we must make a requirement that makes sure that information is only transported over a fraction of one grid length for each time step, i.e.

$$(|\mathbf{u}| + c_f)\Delta t/\Delta x \leq C \tag{2.39}$$

which is known as the Courant condition, where $0 < C < 1$. We use $C \approx 0.15 - 0.30$ to make sure the time stepping is inside the limits of stability.

We have similar conditions considering the diffusive terms:

$$\max(\eta, D) f \Delta t/\Delta x^2 \leq C \tag{2.40}$$

where f is a "safety factor" that depends on the expression used for the quenching operator. In the Hyman scheme that Bifrost uses, $f = 17.36$. D is here the diffusive terms which occurs in the equations for $\frac{\partial \rho}{\partial t}$, $\frac{\partial \rho \mathbf{u}}{\partial t}$ and $\frac{\partial e}{\partial t}$, given (for the x-component) as

$$\Delta x \left(\nu_1 c_f + \nu_2 |\mathbf{u}| + \nu_3 |\Delta_x^1 u_x|_- \right), \tag{2.41}$$

while η is the magnetic diffusion $\eta^{(1)} + \eta^{(2)}$.

Finally, Bifrost requires that

$$\max(\left| \frac{\partial \rho}{\partial t} \right| / \rho, \left| \frac{\partial e}{\partial t} \right| / e) \Delta t \leq C \tag{2.42}$$

which means that the timestep will be decreased if the ρ or e changes with a fraction higher than C.

2.4 Boundary Conditions

Five different models have been evolved during this thesis, given the names C1x1, C2x1, C2x2, C4x2 and C4x3. All of them have boundary conditions which are similar to those described by Martínez-Sykora et al. (2008). The computational box, where a part of the QS atmosphere is modeled, is a Cartesian grid with dimensions of $16.6 \times 8.3 \times 15.8$ Mm^3, divided into $256 \times 128 \times 160$ grid points. The box reaches from the upper convection zone, at a depth of 1.4 Mm below the photosphere (defined to be $z = 0$) to a (coronal) height of 14.4 Mm above the photosphere, including the upper convection zone, photosphere, chromosphere, transition region and (lower) corona.

The boundary conditions for the four "side-walls" of the box are determined by *periodicity*. To demonstrate what this is, think that you are inside the box and walk forwards in the x-direction till you are at the last yz-plane in the box; then you go one step further in the x-direction, out of the box, and you find yourself in a yz-plane with the same physical properties as the first yz-plane in the box. It works the same in the y-direction. In practice, this means that we can put several copies of the same computational box side by side in the xy-plane without losing continuity. We'll then get a self-repeating pattern in the xy-plane, and that is not a bad approximation of the quiet-Sun internetwork inside one cell in the magnetic network.

Non-periodic boundary conditions are implemented on upper and lower boundary by adding ghost zones beyond these boundaries and treating them according to a chosen boundary. The upper and lower boundary have 5 ghost zones each. At the lower boundary, the average temperature are maintained by keeping the inflowing entropy fixed. The boundary is otherwise kept open to allow fluid to enter and leave if required. The upper boundary is also kept open, but with a temperature gradient set to zero to keep conductive flux from leaving or entering through this boundary. To avoid reflection of outgoing waves that reach the upper boundary, characteristic equations are used in this boundary. Except for the temperature, the hydrodynamic variables are set by characteristic extrapolations in the upper ghost zones. However, in some of the models the vertical fluid velocity in the upper ghost zones is ramped to zero instead of being extrapolated to maintain stability, see table 2.1.

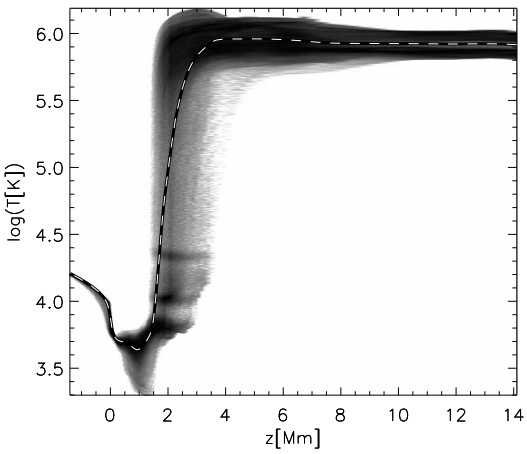

(a) Initial temperature

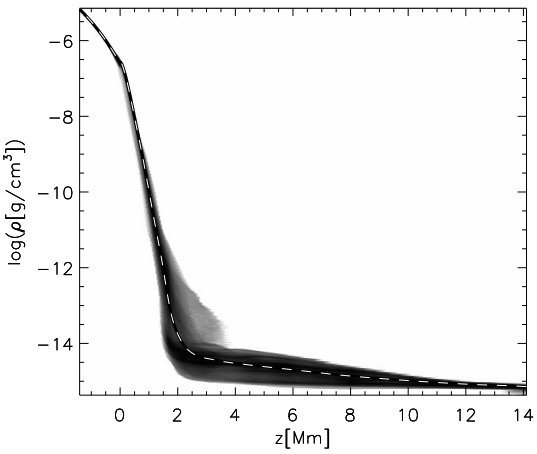

(b) Initial density

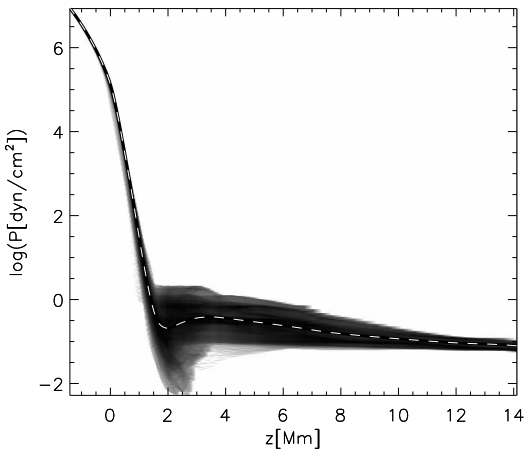

(c) Initial pressure

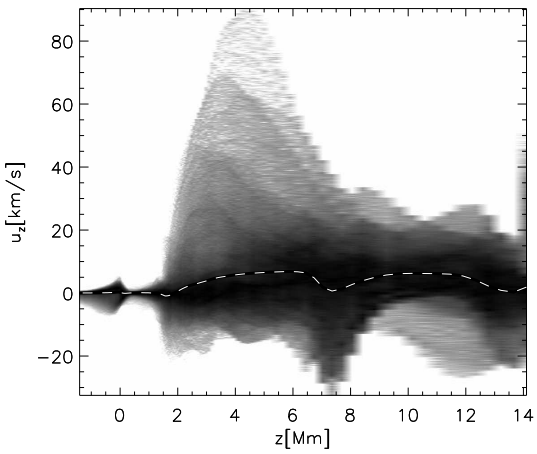

(d) Initial vertical velocity

Figure 2.2: Initial structure of hydrodynamic variables in the models used in this thesis. The grey-scale plots are histograms where the darker points corresponds to the more frequent values of the variable for each specific height. The grey-scale is logarithmic. The horizontally averaged variables are plotted as *dashed lines*.

Model	Handling of u_z in upper ghost zones
C1x1	Extrapolate
C2x1	Extrapolate
C2x2	Extrapolate
C4x2	Flat
C4x3	Flat

Table 2.1: Condition for the vertical velocity at upper boundary. More details about the different models are given in next section and next chapter.

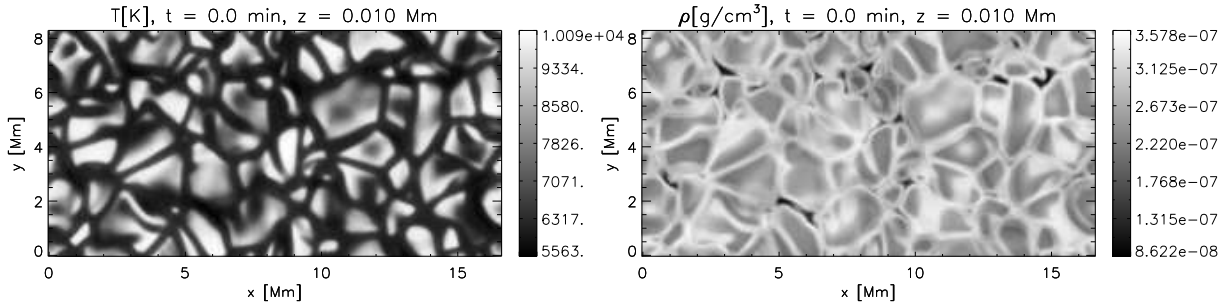

(a) Initial vertical velocity in the photosphere

(b) Initial vertical velocity in the photosphere

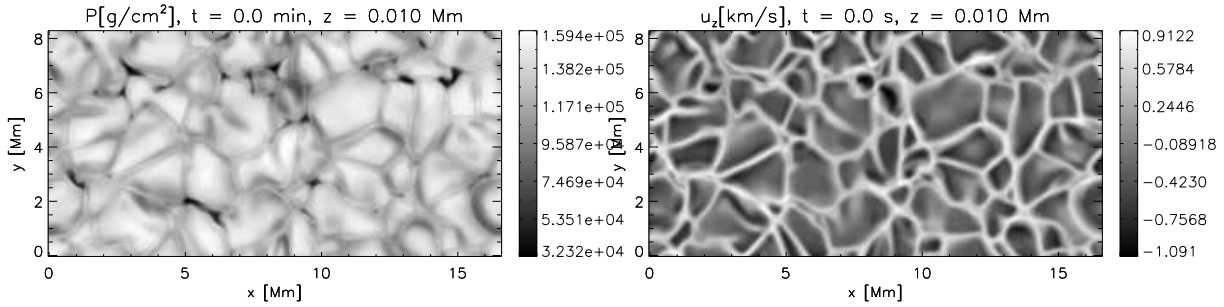

(c) Initial vertical velocity in the photosphere

(d) Initial vertical velocity in the photosphere

Figure 2.3: Initial structure of hydrodynamic variables in the photosphere.

2.5 Initial Conditions

In the five models evolved during this thesis, the initial condition for the hydrodynamic variables (density, fluid velocity, internal energy) are taken from a model which has already been running for a while, evolved by Hansteen et al. (2010). The initial structure of the temperature, density, pressure and vertical velocity are shown in figure 2.2. Lower boundary ($z = -1.4$ Mm) has an average temperature of $\sim 16\,100$ K, an average density of $6.7 \cdot 10^{-6}\ \mathrm{g/cm^3}$ and an average pressure of $8.7 \cdot 10^{6}\ \mathrm{dyn/cm^2}$. Going upwards, we see a structure similar to the QS atmosphere described in the introduction, from the upper convection zone, through the photosphere, chromosphere, and transition region to the corona, where both temperature, density and pressure are relatively constant with height. The temperature is around $\sim 0.8 - 1.0$ MK in the uppermost last 5 Mm, and the density and pressure decreases only slowly with height and reach $7.2 \cdot 10^{-16}\ \mathrm{g/cm^3}$ and $8.0 \cdot 10^{-2}\ \mathrm{dyn/cm^2}$ at upper boundary.

The fluid velocity in the sub-coronal zones is mostly of order $\sim 1-5$ km/s, while the coronal velocities are of order $\sim 10 - 20$ km/s (only vertical component of the fluid velocity is plotted here, but the horizontal component behaves similarly). The velocity in the photosphere (figure 2.3(d)) and below has a granular structure with upflows in granules and downflows in intergranular lanes. Temperature, density and pressure also have a granular structure in the photosphere, as seen in figure 2.3, where the temperature and pressure is higher in the granules than in the lanes, while the density is highest in the lanes.

The only quantity which is initially different from the Hansteen et al. (2010) model is the magnetic field. The aim in this thesis is to experiment with different magnetic topologies and see how it affects the coronal heating and temperature. Therefore the different models have magnetic fields with different degrees of complexity. The initial magnetic field inside the modeled atmosphere is generated by setting up an array for the vertical component of the magnetic field at lower field boundary, then calculate the other two components of the magnetic field and extrapolate each component into the entire cube by using *potential field extrapolation*.

Setting up the Vertical Component of the Magnetic Field at Lower Boundary

The initial condition for the vertical magnetic component, B_z, at lower boundary in each of the five models evolved in this thesis (in addition to a standard model described later) is shown in figures 3.15 and 3.16 in the end of next chapter. In four of these models, the initial condition for B_z at lower boundary looks like a "checkerboard" pattern, where the white "tiles" contains a circular concentrations of downward-oriented magnetic fields, and the black ones have equally strong concentrations of upward-oriented fields. These circular concentrations of vertical magnetic fields is referred to as magnetic *poles* in the rest of this thesis. The numbers after the C in the model name specifies how many chess tiles there are in each direction. C2x1 has a magnetic bipole at the lower boundary, composed of two poles of oppositely oriented vertical magnetic fields, while C2x2 has a magnetic quadrupole at the lower boundary, and C4x2 and C4x3 have chess patterns of 4x2 and 4x3 tiles of upward- and downward-oriented fields at the lower boundary. All models have a weak vertical background field of $\sim$ 1-10 G as well. The magnitude of the the magnetic field in the poles at lower boundary (in the "chess tiles") is set in a way so that the mean value of $|B_z|$ in the photosphere will be of order ~ 100 G. To ensure this, the models with magnetic fields of higher complexity needs higher magnetic

field strengths in the poles at lower boundary. Model C1x1 does not contain any circular poles of magnetic fields, but rather a magnetic field which is initially homogeneous and vertical (i.e. one chess tile), with a magnitude of ~ 100 G. The model is referred to as a magnetic monopole model. A brief overview of the main differences in the initial magnetic fields is given in table 2.2.

Model	No. of magnetic poles at lower boundary	Mean distance between poles at lower boundary	Max $\lvert B_z \rvert$ at lower boundary
C1x1	0	–	100 G
C2x1	2	8.3 Mm	600 G
C2x2	4	6.3 Mm	1.35 kG
C4x2	8	4.2 Mm	1.90 kG
C4x3	12	2.8 Mm	3.17 kG

Table 2.2: Initial properties of the different models

Potential Field Extrapolation

Knowing the vertical component of the magnetic field at lower boundary, we calculate the Fourier transform of this quantity as a function of horizontal wave numbers k_x and k_y. A curl-free magnetic field ($\nabla \times \mathbf{B} = 0$) is assumed, because this will yield the magnetic field configuration with the lowest possible energy. Furthermore, the Fourier transform of each component of the magnetic field is set to decrease with height and horizontal wavenumber as $e^{-\sqrt{k_x^2+k_y^2}z}$, which means that small-scale variations in the magnetic field will diminish rapidly with height, and only variations with wavelengths comparable to the box size will be exist in the upper boundary. This exponential rule, together with the curl-free field assumption, makes sure that we obtain a divergence-free magnetic field ($\nabla \cdot \mathbf{B} = 0$) if we neglect numerical errors. Using these assumptions, the Fourier transformed horizontal components of the magnetic field at lower boundary can be obtained, and then the Fourier transformed magnetic field in all the above-lying layers. Finally, the inverse Fourier transform is applied to obtain the magnetic field for each layer. Because of numerical errors in this routine, the magnetic field which is obtained is not completely divergence-free, and therefore an additional $\nabla \cdot \mathbf{B}$-cleaning routine need to be applied sporadically.

3

RESULTS

The goal of this thesis is to gain more knowledge on how the heating of the solar corona is connected to the complexity of the magnetic field in the photosphere. While the first chapter reviewed our theoretical background about stars and the sun in particular, leading to the problem investigated in this thesis, and the second chapter described the numerical method which is used in attempt to solve that problem, the aim of this chapter is to analyze six different numerical models of the QS atmosphere in order to reach the goal of this thesis. One of these models is imported from Hansteen et al. (2010) and will be used as a *standard model*. It is the model which Hansteen et al. refers to as B1, and it will therefore have the same name in this thesis. The other five models have been evolved during working with this thesis, and the results in each of those models will be compared to the results of the standard model and finally compared to each other.

Below is a short list of terms which will be actively used during analysis of the results and need therefore to be defined:

- *Magnetic pole*, defined as a concentration of a vertical magnetic field in the photosphere (or the lower boundary) oriented in one specific direction (upwards or downwards). Thus, the magnetic field inside one magnetic pole is oriented either upward or downward, but not in both directions.
- The *complexity* in the photospheric magnetic field (or sometimes just called the complexity in the magnetic field): this term tells us about how complicated the magnetic field configuration is in the photosphere. The complexity can be measured by measuring *density of magnetic poles* in the photosphere, or measuring the *typical separation distance* between magnetic poles in the photosphere. The complexity is thus proportional to the former quantity and inversely proportional to the latter. We distinguish between the *initial* complexity and the *effective* complexity of the magnetic field. The effective complexity tells us how complex the photospheric field tends to be as the simulation stabilizes and is proportional to the initial complexity as long as the typical separation distance between magnetic poles do not get short enough to cause some of the poles "drown" below the photosphere or merge together with another pole.
- Magnetic *canopy*: in most parts of the solar atmosphere, the magnetic fields that emerge from the photosphere in separate regions connect together above the photosphere in loops. Wedemeyer-Böhm et al. (2009) refers to the region in the atmosphere where those magnetic loops occur as a canopy, a term originally introduced by Gabriel (1976). Magnetic loops also occur in several of the models studied in this thesis, and the uppermost height where those

loops occur in this thesis is defined as the *canopy height*. The region below a magnetic canopy is referred to as the *sub-canopy region*.

- *Current sheet* (Galsgaard & Nordlund 1996), defined as a tangential discontinuity in a magnetic field, which can give rise to relatively strong currents. In the analysis of the results, we distinguish between large-scale current sheets (current sheets wider than $\sim$0.5 Mm) and the tiny current sheets ($\sim$100 km) caused by the convective stressing of magnetic fields which eventually burst out as nanoflares, described below.

- *Hierarchy of current sheets*: when a series of weaker current sheets arise near a stronger current sheet, this is usually referred to as a hierarchy of current sheets(Galsgaard & Nordlund 1996). In this thesis, the term exclusively concerns large-scale current sheets. The *complexity of the hierarchy* of current sheets tells us about how many weak current sheets that are generated nearby each of the strong "main" current sheets.

- *Nanoflare* (Parker 1988): When near-lying magnetic field lines twist around each other due to convective motion, the magnetic field get stressed. When the stress becomes too high, the twisting of the field lines collapses into a tiny current sheet which eventually causes the twisted magnetic field to reconnect. The reconnection dissipates the energy originally stored in the twisted lines into the surrounding medium in an explosive burst which is referred to as a nanoflare. It is not possible to detect a physical nanoflare in particular in these models, because the stressing of the magnetic field which causes a nanoflare occurs within widths comparable to the diffusion length, which in the solar photosphere is of order 10 m (de Wijn et al. 2009). In the code, however, the diffusion length is larger than the grid length, which is about $\sim$60 km. Therefore, a nanoflare in the models studied in this thesis will be defined as the (relatively) tiny burst with a width of order 100 km which occurs due to the stressing of the field. In the models where magnetic fields from below the photosphere connect together above the photosphere in a canopy, the generation of nanoflares is likely to be much less frequent above this canopy than below, because the fields above the canopy are both weaker and less directly connected to the convective motions in the photosphere. Thus, the coronal heating due to nanoflares are likely to increase when increasing the height of the canopy (above the TR).

3.1 Presenting the Physical Properties of Interest

Below is a short description of the physical properties which are analyzed in this thesis and how they are presented. It includes both three-dimensional plots, two-dimensional xy-plots, "function-of-time"-plots and "function-of-height"-plots. In all three-dimensional plots, the photosphere is plotted in as a plane at $z = 0$ with a two-dimensional temperature plot showing the granulation. The location of the TR is also plotted in as the isosurface where the $T = 0.1$ MK. The purpose of plotting the photosphere and the TR is to give the reader an idea of where the different regions of the modeled atmosphere are located.

3.1.1 Magnetic Fields

The magnetic field is is the only physical property which is initially set to be different in each model. Thus, each model is "identified" by its magnetic field configuration, and it is therefore natural to start studying each model by having a look at its magnetic fields. Since the initial magnetic fields are put into the models by "brute force", it needs some time (at least a few minutes) to adjust itself into equilibrium with the fluid dynamics, especially in the photosphere and below, where the plasma β is high. Therefore, in most of the plots, the magnetic fields are evaluated after a certain amount of simulated solar time.

The magnetic fields in each model are presented in the following way:

- Three-dimensional plots of magnetic field lines are given, showing what the magnetic fields look like at the end of each simulation.
- Two-dimensional plots of the vertical component of the initial magnetic field at lower boundary are given, since this is the only free parameter (while the rest of the initial magnetic field is generated by potential field extrapolation), as discussed in section 2.5. The resulting structure of the vertical magnetic component in the photosphere at $t = 30.0$ min is shown in a similar way. The plots can be found at the end of this chapter, in figures 3.15 and 3.16.
- Horizontal averages of the (absolute values of the) vertical and horizontal components of the magnetic field, as well as magnetic field inclination and magnetic energy density, are evaluated at $t = 30.0$ min in each simulation. The plots can be found at the end of this chapter, in figures 3.17 and 3.18.

3.1.2 Temperature Structure

Since we want to study how the coronal heating depends on the magnetic field configuration, it is convenient to study the resulting temperature in each model. The temperature structure in each model are therefore presented the following way:

- Three-dimensional colour-plots of the temperature are given, evaluated at the end of each simulation, plotted together with magnetic field lines.
- To see how the coronal temperatures evolves with time, the average temperature in the entire region above $z = 3.0$ Mm is computed as a function of time. The plots can be found at the end of this chapter, in figures 3.19 and 3.20.
- Histograms of the temperature as function of height are given, evaluated at the end of each simulation. The plots can be found at the end of this chapter, in figures 3.19 and 3.20.

3.1.3 Joule Heating

Joule heating, or Ohmic heating, is defined by

$$Q_{\mathrm{J}} = \mathbf{E} \cdot \mathbf{J} = \eta J^2, \tag{3.1}$$

and is similar to the heating dissipated in electric circuits. Twisting of magnetic field lines (due to convective shuffling in the photosphere) and other tangential discontinuities in the magnetic field can transport energy from the photosphere to the corona through current sheets (Galsgaard & Nordlund 1996). These current sheets dissipate energy in the form of Joule heating to the surrounding medium, sometimes in short bursts called nanoflares. Therefore, the Joule heating is the component of the coronal heating which is likely to depend most on the magnetic field configuration and will therefore be studied in this chapter.

The average Joule heating is computed in five selected regions of the solar atmosphere, described briefly below:

- Region 1: $z = 0.5 - 1.0$ Mm which is more or less the *middle chromosphere*. In a very few cases, the transition region might reach down to these heights.
- Region 2: $z = 1.0 - 1.5$ Mm which is more or less the *upper chromosphere*, though it might contain some coronal matter in cases where the TR height is low enough.
- Region 3: being defined as the region where the temperature is between $20\ 000$ and $300\ 000$ K, this region represents generally the *lower TR*. However, if the coronal model is cool enough, this region might be the entire TR (or even include parts of the corona).
- Region 4: being defined as the region where the temperature is between $300\ 000$ and $700\ 000$ K, this region represents generally the *upper TR*. However, if the coronal model is cool enough, this region will rather represent the base of the corona or even the entire corona.
- Region 5: $z = 3.0 - 12.0$ Mm, i.e. the bulk of the modeled corona. It can contain fragments of the upper chromosphere (and TR) in the (few) cases where the TR reaches above $z = 3.0$ Mm.

The average Joule heating in these five regions are referred to as $Q_{\rm J}^{(1)}$, $Q_{\rm J}^{(2)}$, $Q_{\rm J}^{(3)}$, $Q_{\rm J}^{(4)}$ and $Q_{\rm J}^{(5)}$. Time-evolution of these values is shown at the end of this chapter, in figures 3.21 and 3.22. These plots are the most important results in this thesis, because they are used to study the correlation between the complexity in the photospheric magnetic field and the resulting Joule heating in the chromosphere and the corona.

Since Joule heating is closely related to current density, three-dimensional plots of the current density are also given, evaluated at the end of each simulation. The purpose is to have a look at the resulting current sheet structure in each model, since a hierarchy of current sheets is a possible coronal heating mechanism (Galsgaard & Nordlund 1996). The current density is given in the units of a *typical chromospheric current density*, $J_{\rm chr}^{\rm B1}$, defined as the mean current density in the middle chromosphere ($z = 0.5 - 1.0$ Mm) in the standard model, averaged over the time period after the physical properties of the standard model middle chromosphere have stabilized.

3.2 The Standard Model B1

3.2.1 Magnetic Fields

The magnetic field configuration in the standard model is shown in figure 3.1. In contrast to the models simulated during this thesis, this model has relatively chaotically organized magnetic fields. Below

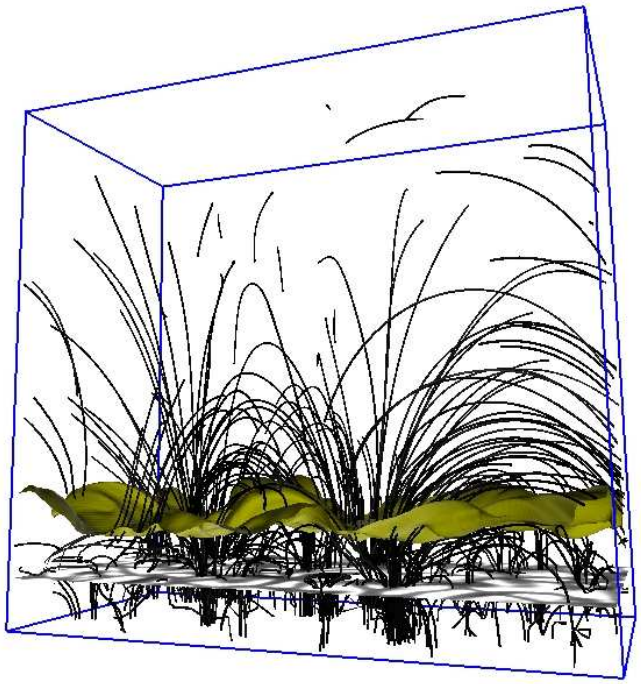

Figure 3.1: Three-dimensional plot of the magnetic field in the standard model, evaluated at $t = 60.7$ min. The horizontal plane with the granulation pattern marks the location of the photosphere, while the above-lying curved surface marks the center of the TR ($T = 10^5$ K).

the photosphere, the magnetic fields are concentrated in a few randomly located poles of upward- and downward-oriented fields. Above the photosphere, fields from the different poles bend outwards and connect together in loops. The loops are located all from right above the TR up to heights of ~ 10 Mm above the photosphere.

A closer look on the vertical magnetic field in the photosphere is given in figure 3.15(b). The poles of upward- and downward-oriented fields are concentrated in the intergranular lanes, while the granules are almost magnetically neutral. This cutout of the photosphere contains 5, maybe 6, magnetic poles, separated by typical distances of 4-5 Mm.

The horizontal averages of the vertical and horizontal component of the magnetic field at $t = 30.0$ min, as well as the inclination of the magnetic field relative to the vertical axis and the magnetic energy density, are plotted in figures 3.17 and 3.18 at the end of this chapter. The vertical magnetic component is of order 200 G near the lower boundary and decreases with height to less than 1 G near the upper boundary. The horizontal component decreases more slowly with height, going from about 150 G at lower boundary to ~ 2 G at the upper boundary, but with a slight increase near the photosphere, where the field inclination is relatively high due to the fact that the field is constantly shuffled around by the convective motion. The field is more or less horizontal near the upper boundary, since the field here is characterized by the top of magnetic loops. The magnetic energy density decreases with height, going from about $\sim 0.5\ \mathrm{erg\ cm^{-3}}$ at the lower boundary to $\sim 10^{-5}\ \mathrm{erg\ cm^{-3}}$ at the upper boundary.

3.2.2 Temperature Structure

Figure 3.2(a) shows a three-dimensional colour-plot of the temperature together with the magnetic field structure in the standard model. This is a relatively hot model with much activity. The corona has temperatures of order $\sim$1.4-1.8 MK with some cooler coronal loops of $\sim$1.0 MK which are aligned with magnetic loops. The cooler loops can possibly be caused by cooler gas from below the corona (where the temperature also is $\sim$1.0 MK) which is transported up along the magnetic loops, or they can be caused by radiative cooling. A large heating event with a temperature rising to 1.9 MK occurs right above the TR, near one of the side-walls, as seen in figure 3.2(a). Only one of the five models evolved in this thesis (C2x1) has a high level of coronal activity comparable to this model, but even that model has a simpler coronal structure than this (even though that model obtains much hotter corona).

As shown in 3.19(a), the mean temperature in the corona starts around 0.9 MK and increases with time and ends up near 1.5 MK after 60 min (where it possibly stabilizes). The temperature histogram in figure 3.19(b) shows that the height of the TR varies all from about 1.2 Mm to 2.5 Mm above the photosphere. The temperature profile below the TR behaves quite as expected: the temperature in the chromosphere ranges from 2000 K to 6-7000 K, while the photospheric temperature ranges from 5000 K (intergranular lanes) to 8-9000 K (granules), and the temperature right below the photosphere is higher than 10 000 K, increasing nearly adiabatically with depth.

3.2.3 Joule Heating

From the time-evolution plots of the mean Joule heating in the five selected regions in this model, given in figure 3.21, we see first that the Joule heating in the chromosphere ($Q_{\rm J}^{(1)}$ and $Q_{\rm J}^{(2)}$ for the model B1) starts at a relatively low value, increases rapidly in the first 15-20 min (more or less), then decreases during the next 5-10 min until it stabilizes around 0.055 erg s^{-1} cm^{-3} in the middle chromosphere and 0.02 erg s^{-1} cm^{-3} in the upper chromosphere. The Joule heating in the TR ($Q_{\rm J}^{(3)}$ and $Q_{\rm J}^{(4)}$) increases in the first 5-10 min before it stabilizes at around 0.023 erg s^{-1} cm^{-3} in the lower TR and 0.014 erg s^{-1} cm^{-3} in the upper TR. The coronal Joule heating ($Q_{\rm J}^{(5)}$) increases in the first 5 min and stabilizes around 0.011 erg s^{-1} cm^{-3}. These results will be used to compare with the results from the models evolved in this thesis.

A three-dimensional colour-plot of the current density in this model is given in figure 3.2(b). The region where the large heating event occurs (as mentioned shortly in the temperature section) seems to generate current sheets with currents of chromospheric (i.e. relatively high) values. Weaker current sheets do also occur nearby these strong current sheets. In the other regions of the corona, it is hard to detect single current sheets, probably because the chaotically organized magnetic fields generates a superposition of many chaotically current sheets, which results in a very chaotic current structure.

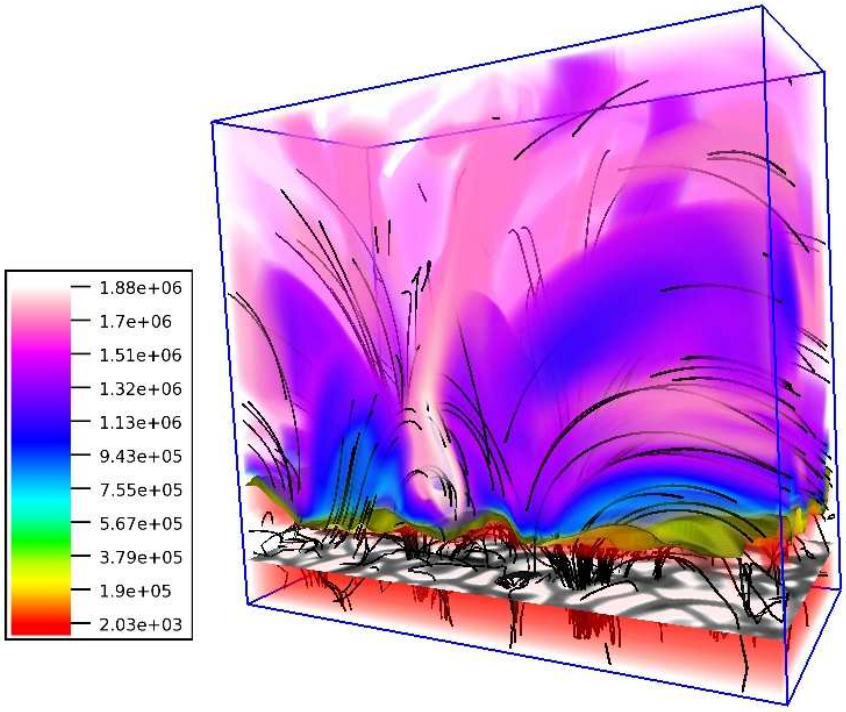

(a) B1, temperature and magnetic fields at $t = 60.7$ min. NOTE: Different colour scaling than in the temperature plots for the other models.

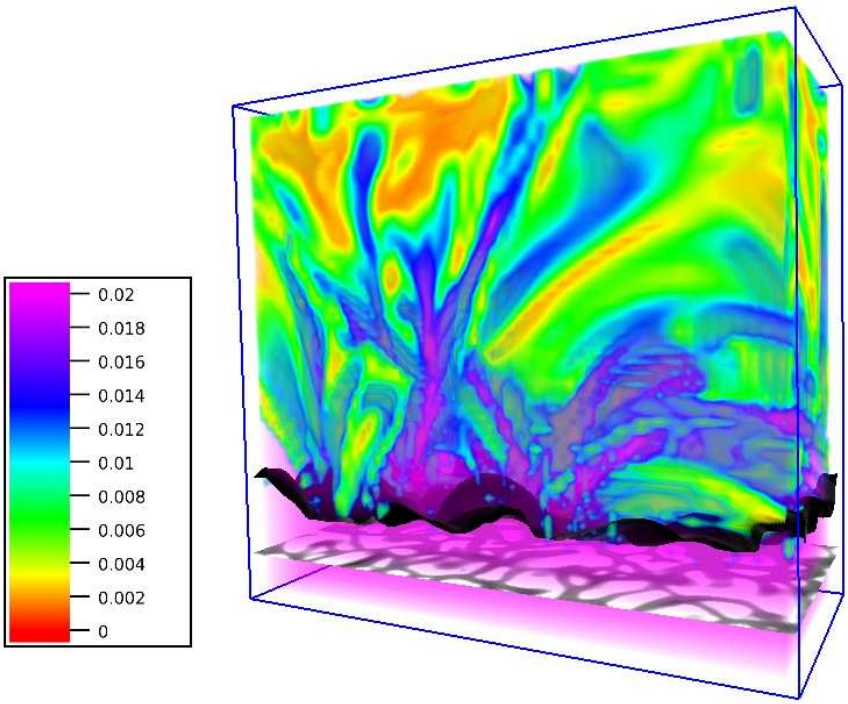

(b) B1, current density relative to the typical chromospheric current density, $J/J_{\rm chr}^{\rm B1}$, at $t = 60.7$ min. Current densities much higher than the peak value in this plot occurs near the TR and below, but is ignored to make the *coronal* currents more visible.

Figure 3.2: Three-dimensional plot of (a) temperature and magnetic field and (b) current density in the standard model. The horizontal plane with the granulation pattern marks the location of the photosphere, while the above-lying curved surface marks the center of the TR ($T = 10^5$ K).

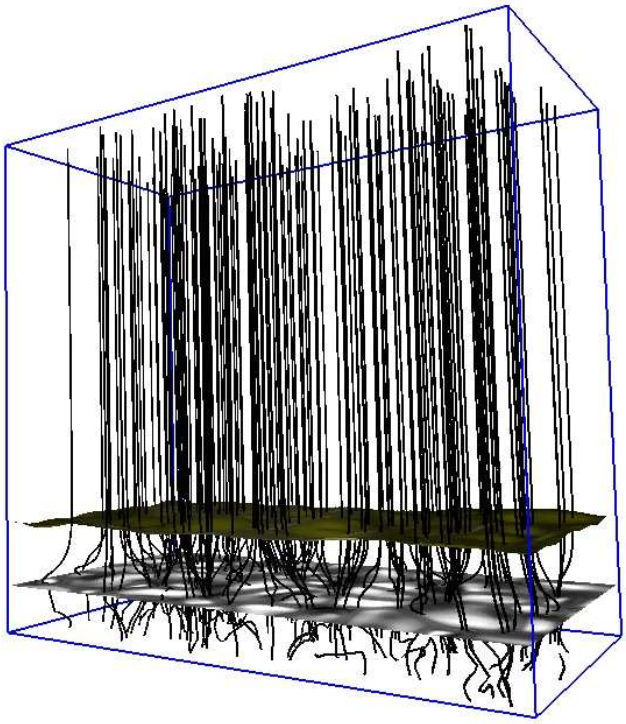

Figure 3.3: Three-dimensional plot of the magnetic field in model C1x1, evaluated at $t = 35.0$ min. The horizontal plane with the granulation pattern marks the location of the photosphere, while the above-lying curved surface marks the center of the TR (defined here as $T = 50\ 000$ K).

3.3 The Magnetic Monopole Model C1x1

3.3.1 Magnetic Fields

The magnetic field in this model is initially homogeneous and vertical, and, as shown in figures 3.3 and 3.15(d), it remains fairly stable through the entire simulation, except for the region around the photosphere and below, where the magnetic field is forced into the intergranular lanes and shuffled around due to convective motion.

Figure 3.17 shows that the vertical magnetic component is more or less about 100 G in the entire atmosphere, which is half the corresponding value in the standard model lower boundary and more than 100 times that in the standard model upper boundary, making this model the one with the strongest (vertical) magnetic field in the corona (as well as the model with the smallest level of magnetic activity). The horizontal component (figure 3.18) has values comparable to the vertical component below the surface but decreases rapidly with height until it is less than 1 G at upper boundary. This model is also the one with the smallest magnetic energy density at the lower boundary (about a third of that in the standard model) and the largest magnetic energy density in the corona ($\sim 0.02\ \mathrm{erg\ cm^{-3}}$, i.e. about 2000 times the value at the standard model upper boundary) due to the uniformly strong coronal magnetic field.

3.3.2 Temperature Structure

As one can see in figures 3.4(a) and 3.19(d), this model ends up with a relatively low coronal temperature, ranging between 0.08 and 0.4 MK. As in the other models, the mean coronal temperature starts at about 0.9 MK, but decreases slowly with time and is about 0.45 MK after 30 min before it suddenly drops below 0.2 MK within the next 5 min (figure 3.19(c)). Thus, the corona ends up with a mean temperature of less than 1/7 of what the standard model coronal temperature reaches. The height of the TR is more or less constantly located around 2.0 Mm above the photosphere, with deviations no larger than about 200 km. The chromospheric temperatures have also a smaller range than in the standard model, from about 3000 K to 5-6000 K. Below the chromosphere, the temperature behaves in a manner quite similar to the standard model temperature.

3.3.3 Joule Heating

From the time evolution plots of the Joule heating in the five selected regions in this model, given in figure 3.21, one can see that the Joule heating in each region starts with the same values as in the standard model. In the middle chromosphere, the Joule heating decreases rapidly the first 2-3 min and stabilizes around $0.015\ \mathrm{erg\,s^{-1}\,cm^{-3}}$ which is slightly more than 1/4 of that in the standard model. The Joule heating in the upper chromosphere decreases even more rapidly within the same time and stabilizes around only $\sim 10^{-4}\ \mathrm{erg\,s^{-1}\,cm^{-3}}$ (less than 1/200 of that in the standard model). The TR Joule heating ($Q_{\mathrm{J}}^{(3)}$) stabilizes around $\sim 10^{-5}\ \mathrm{erg\,s^{-1}\,cm^{-3}}$ after 5 min, and the coronal Joule heating (both $Q_{\mathrm{J}}^{(4)}$ and $Q_{\mathrm{J}}^{(5)}$ in this model) stabilizes around $\sim 1.7 \cdot 10^{-5}\ \mathrm{erg\,s^{-1}\,cm^{-3}}$ after 20 min ($\sim$1/1000 of that in the standard model). The fast stabilization of the Joule heating is probably due to the relatively low level of magnetic activity in this model. This model is clearly the one which has the lowest amount of Joule heating in all regions of the atmosphere, having almost no Joule heating in the TR and the corona. This is not unexpected, since an atmosphere with an almost homogeneous magnetic field will have very little magnetic activity which can generate Joule heating. Because of the shuffling of magnetic fields in the photosphere, a small number of nanoflares per time unit will probably be generated, but not enough to heat the corona up to temperatures above 1 MK.

As shown in figure 3.4(b), no generation of large scale current sheets (>0.5 Mm) seems to be present in this model, only some vertical arms of weak currents which reach from the chromosphere and into the corona. These arms are probably a superposition of (tiny) current sheets due to the convective twisting of the magnetic field which eventually burst out in nanoflares.

3.4 The Magnetic Bipole Model C2x1

3.4.1 Magnetic Fields

This model is a bipole model, which means that this atmospheric box has two poles of (almost) vertical magnetic fields which go from lower boundary through photosphere and bend out into the chromosphere and corona, as seen in figure 3.5 (and 3.15(f)). Magnetic field lines from the innermost sides of the two poles (the sides which faces the center of the box) loop together in the chromosphere,

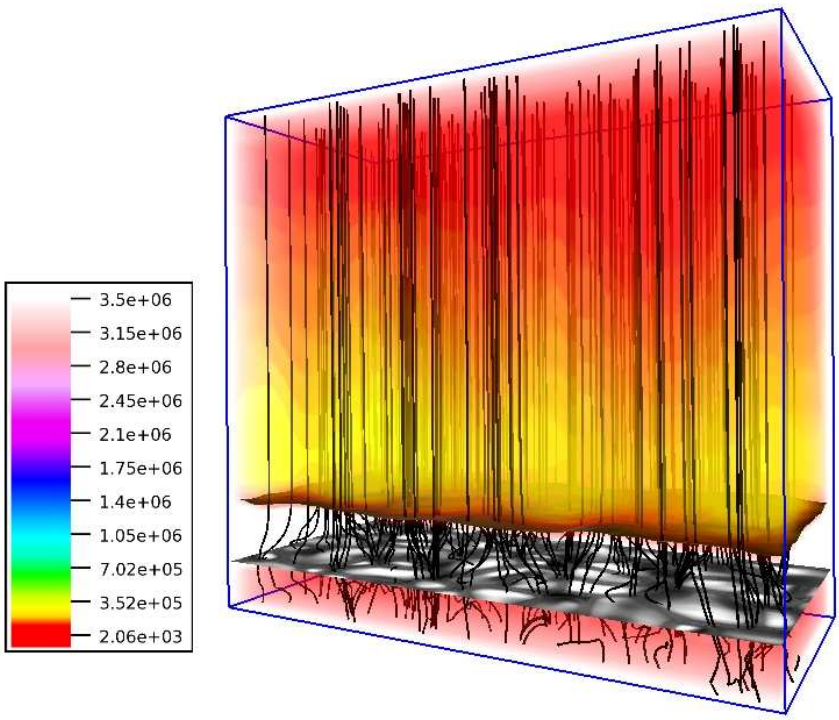

(a) C1x1, temperature and magnetic fields at $t = 35.0$ min.

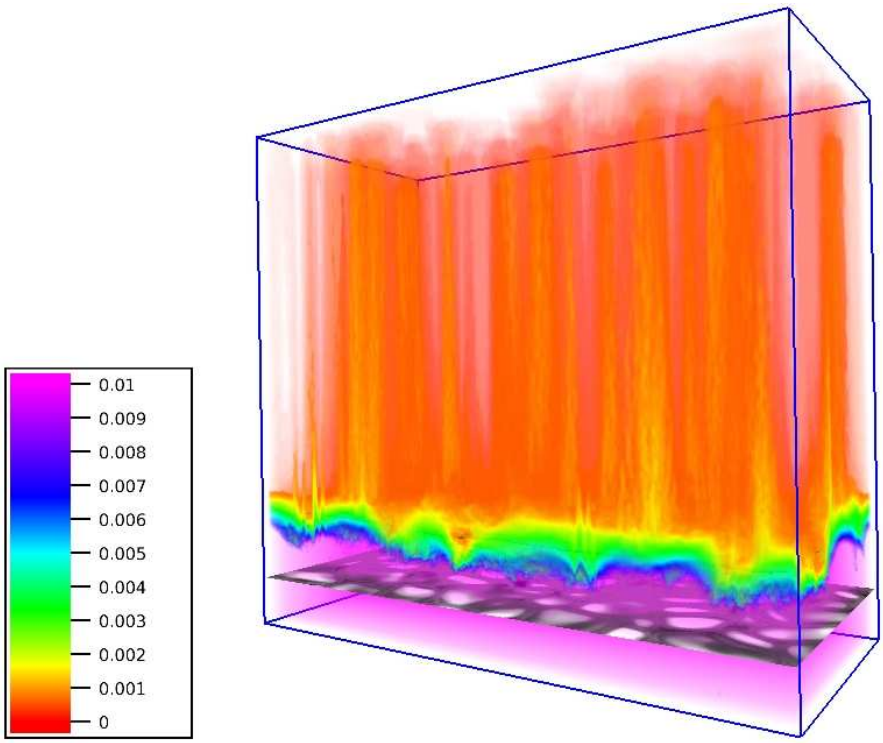

(b) C1x1, current density relative to the typical chromospheric current density, $J/J_{\rm chr}^{\rm B1}$, at $t = 35.0$ min. Current densities much higher than the peak value in this plot occurs near the TR and below, but is ignored to make the *coronal* currents more visible.

Figure 3.4: Three-dimensional plot of (a) temperature and magnetic field and (b) current density in model C1x1. The horizontal plane with the granulation pattern marks the location of the photosphere, while the above-lying curved surface marks the center of the TR (defined here as $T = 50\,000$ K).

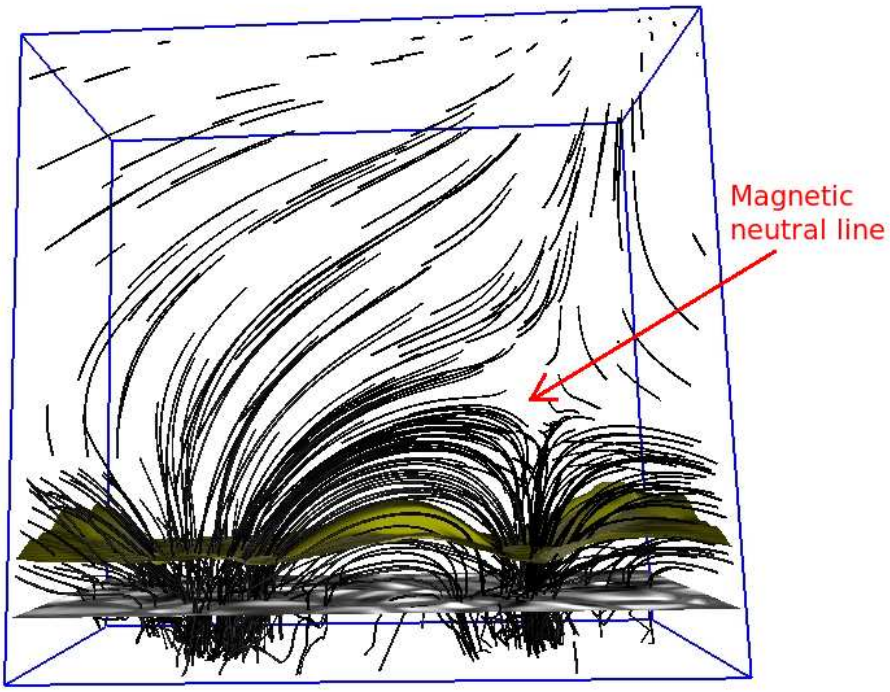

Figure 3.5: Three-dimensional plot of the magnetic field in model C2x1, evaluated at $t = 40.0$ min. The horizontal plane with the granulation pattern marks the location of the photosphere, while the above-lying curved surface marks the center of the TR ($T = 10^5$ K).

while field lines a bit closer to the center of each pole loop together in the corona. Field lines which emerge in the photosphere near the centre of each pole do not loop together, but keep going upwards (but not entirely vertically) through the corona. Field lines at the outwards facing side of each pole loop together with field lines from poles outside this box (remember that this box is periodic in the horizontal directions). The magnetic loops reach up to the canopy height which in this model is located about 5.6 Mm above the photosphere. Fields which do not loop together in the canopy, or in the sub-canopy region, continue upwards (but not exactly vertically) through the corona. Right above the pole to the right in figure 3.5, there is a *magnetic neutral line* going in the y-direction (i.e. the horizontal direction parallel to the shortest sidewall) which, as we will see later, generates strong current sheets and heats the corona very rapidly.

As seen in figures 3.17 and 3.18, both the vertical and horizontal components of the magnetic field at the lower boundary are approximately 200 G on average i.e. almost the same as in the standard model (the horizontal component is just a bit larger here). The magnetic energy at the lower boundary is thus only slightly larger than in the standard model. Since a significant part of the magnetic fields which emerge from the photosphere loop together in the sub-canopy region, the coronal magnetic field (especially above the canopy) is much weaker in this model than in the magnetic monopole model while the mean magnetic field in the photosphere is almost equally strong in all models. More specifically, the magnetic field at the upper boundary in this model has an energy density of $\sim 4.0\,\mathrm{erg\ cm^{-3}}$ which is 1/5 of that in the magnetic monopole model, but still 400 times that in the standard model.

3.4.2 Temperature Structure

As seen in figure 3.6(a), this model obtains a much warmer corona than all the other models, reaching a mean temperature of 2.8 MK after 40 min (figure 3.19(e)), where it seems to start stabilizing, i.e. almost twice the mean temperature which the standard model obtained after 60 min. The peak temperature occurs around the magnetic neutral line, mentioned in the discussion of the magnetic fields, which is likely to be the main generator of coronal heating in this model. Apart from this, the temperature is higher than 1.7 MK in the entire corona, more or less, and higher than 2.5 MK at all heights above $z =$5-6 Mm.

The location of the TR seems to be slightly aligned with the above-lying magnetic loops, and the TR height, according to figure 3.19(f), varies from about 1 Mm to 2.5 Mm above the photosphere (similar to the standard model, except that the TR height in the standard model varies more randomly with x and y). The temperature profile below the TR is similar to that of the standard model.

3.4.3 Joule Heating

By studying the time evolution of the Joule heating in this model, as given in figure 3.21, we see first that the Joule heating in middle chromosphere increases with time during the first 10 min and stabilizes around $0.04\ \mathrm{erg\ s^{-1}\ cm^{-3}}$ i.e. slightly more than 2/3 of that in the standard model. In the above-lying zones, the Joule heating is still increasing at the end of this simulation at $t = 40$ min. At that point, the Joule heating in upper chromosphere and TR ($Q_{\mathrm{J}}^{(4)}$) are both about $0.03\ \mathrm{erg\ s^{-1}\ cm^{-3}}$ i.e. slightly larger than the corresponding values which the standard model stabilized around. The Joule heating in the corona is at this point about $0.003\ \mathrm{erg\ s^{-1}\ cm^{-3}}$, which is almost three times the corresponding stabilization value in the standard model. Ideally this model should have run for a longer time, but because of a growing numerical error and a lack of time to fix that error, it was necessary to stop the simulation after 40 min of solar time. However, it is clearly that the Joule heating in the regions above middle chromosphere grows faster in this model than in any of the other models.

Figure 3.6(b) shows that this models has a lot of relatively strong currents in the corona. The region around the magnetic neutral line generates currents of magnitude comparable to the chromospheric currents, and large and relatively strong current sheets (coloured green in the figure) comes out of this region, heating the corona to higher temperatures than any of the other models. All in all, this model seems to have coronal currents of magnitudes comparable to that of the standard model, though not so randomly organized.

3.5 The Magnetic Quadrupole Model C2x2

3.5.1 Magnetic Fields

This model has a photospheric magnetic field which is “twice as complex” as in the previous model, as seen in figure 3.7 (and 3.15(h)), being concentrated in 4 poles of almost vertical fields which bend out above the photosphere and connect together in loops reaching up to the canopy located about 3.4

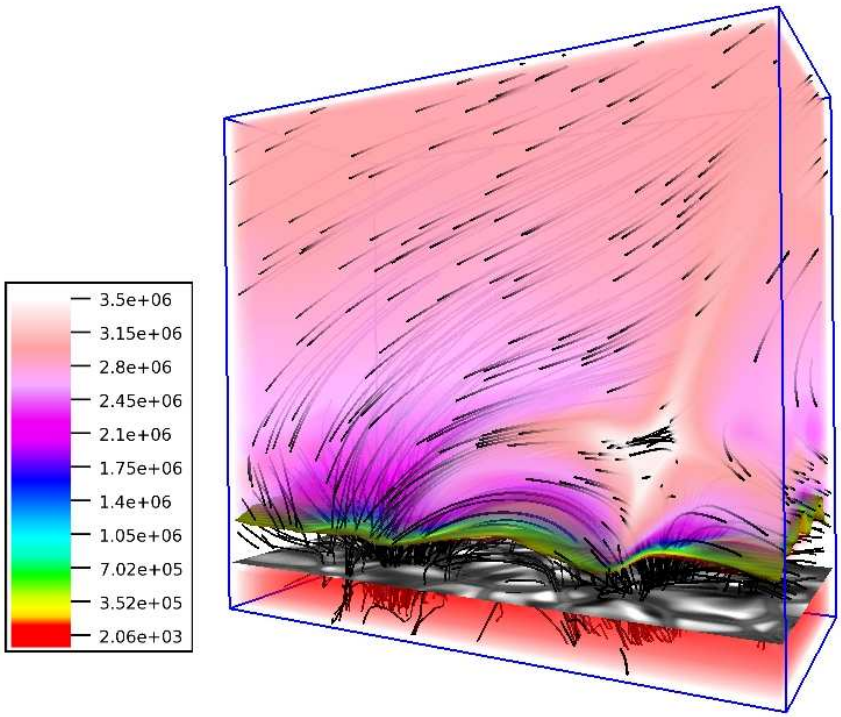

(a) C2x1, temperature and magnetic fields at $t = 40.0$ min.

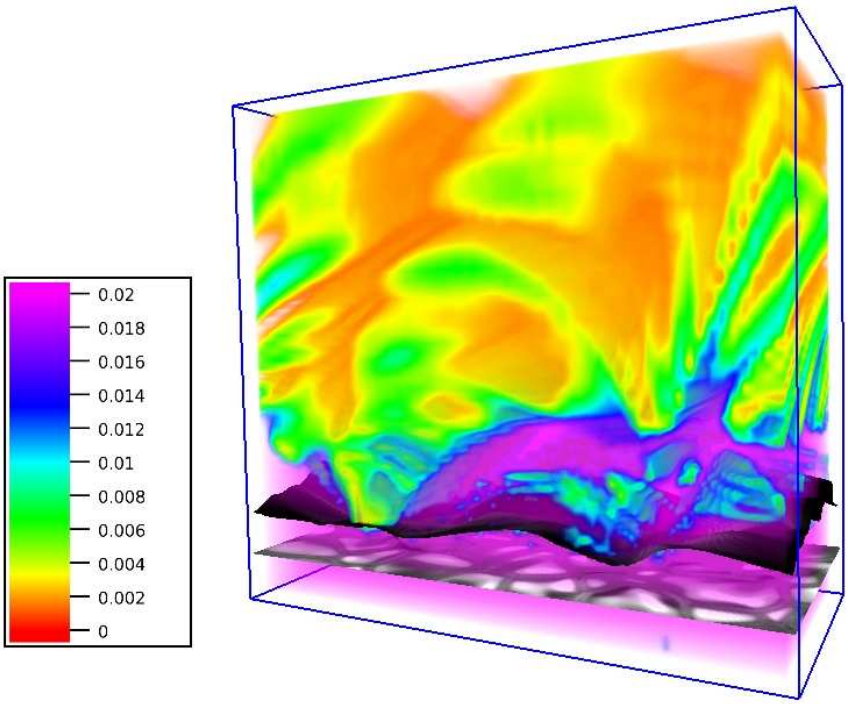

(b) C2x1, current density relative to the typical chromospheric current density, $J/J_{\rm chr}^{\rm B1}$, at $t = 40.0$ min. Current densities much higher than the peak value in this plot occurs near the TR and below, but is ignored to make the *coronal* currents more visible.

Figure 3.6: Three-dimensional plot of (a) temperature and magnetic field and (b) current density in model C2x1. The horizontal plane with the granulation pattern marks the location of the photosphere, while the above-lying curved surface marks the center of the TR ($T = 10^5$ K).

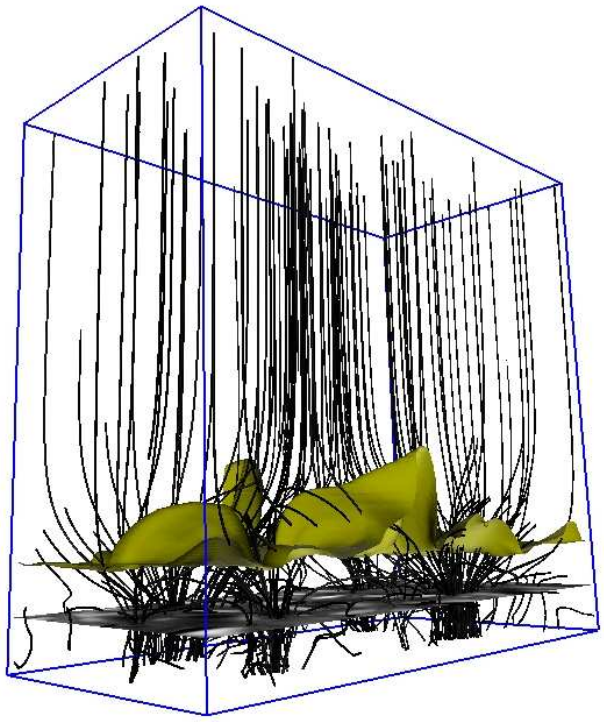

Figure 3.7: Three-dimensional plot of the magnetic field in model C2x2, evaluated at $t = 65.0$ min. The horizontal plane with the granulation pattern marks the location of the photosphere, while the above-lying curved surface marks the center of the TR ($T = 10^5$ K).

Mm above the photosphere (lying close to the TR). Above the canopy, the magnetic field is more or less vertical.

According to figures 3.17 and 3.18, the magnetic field at the lower boundary has a vertical component slightly larger than in the standard model (~ 250 G) and a horizontal component almost twice that in the standard model (~ 300 G), yielding a magnetic energy about twice as large as in the standard model ($\sim 1.0\,\mathrm{erg\ cm^{-3}}$). The average photospheric magnetic field is approximately equally strong as in the other models. Because this model has an even more complex photospheric (and chromospheric) magnetic field than the previous model, more of the magnetic field lines which emerge from the photosphere loop together, resulting in an even weaker coronal magnetic field, with a mean energy density of $\sim 1.0^{-3}\,\mathrm{erg\ cm^{-3}}$ i.e. 1/4 of the corresponding upper boundary value in the bipole model, but still 100 times that of the standard model (which has very weak magnetic fields at the upper boundary).

3.5.2 Temperature Structure

This model gets a much cooler corona than the bipole model, as seen in figure 3.8(a). Figure 3.20(a) shows that the mean coronal temperature decreases slightly the first 15 min and increases slowly with time during the next 20-30 min. Then, the temperature increases more rapidly and is about 1.80 MK after 65 min and still growing rapidly. Thus, this model has a mean coronal temperature a

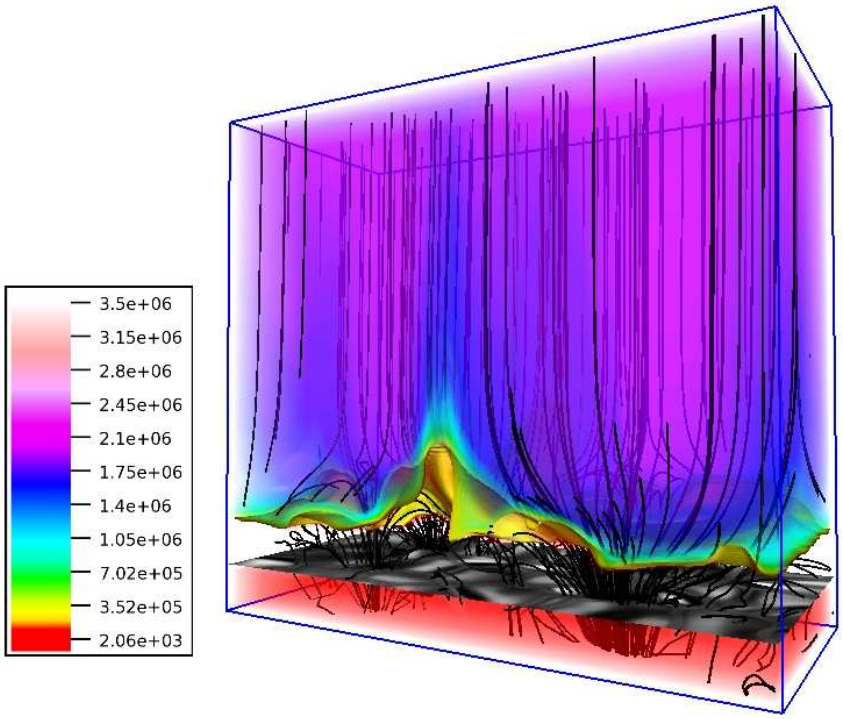

(a) C2x2, temperature and magnetic fields at $t = 65.0$ min.

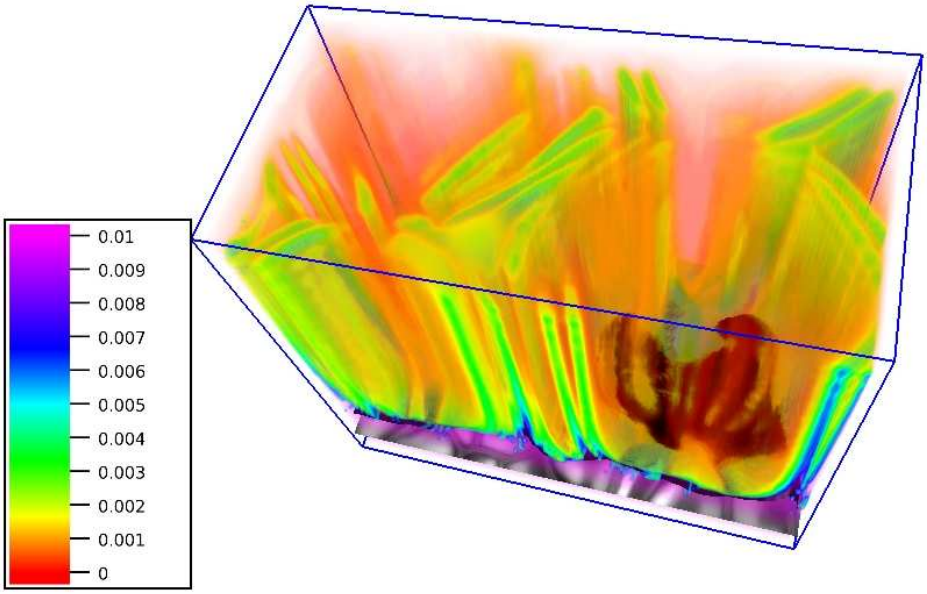

(b) C2x2, current density relative to the typical chromospheric current density, $J/J_{\mathrm{chr}}^{\mathrm{B1}}$, at $t = 65.0$ min. Current densities much higher than the peak value in this plot occurs near the TR and below, but is ignored to make the *coronal* currents more visible.

Figure 3.8: Three-dimensional plot of (a) temperature and magnetic field and (b) current density in model C2x2. The horizontal plane with the granulation pattern marks the location of the photosphere, while the above-lying curved surface marks the center of the TR ($T = 10^5$ K).

bit higher than that of the standard model after 60 min (still, less than the coronal temperatures the bipole model reaches after 40 min), and it increases more rapidly and will *presumably* stabilize at a higher significantly coronal temperature than the standard model (but that requires further simulation to be confirmed). As seen in figure 3.20(b), the height of the TR varies mostly between 1.2 Mm and 2.5 Mm above the photosphere, being especially high near the canopy above two of the poles and slightly aligned with the magnetic loops in the sub-canopy region. However, at the time this three-dimensional snapshot is taken, the TR height seems to reach up to 4.0 Mm above the photosphere near one of the poles. Below the TR, the temperature behaves similarly to the standard model temperature.

3.5.3 Joule Heating

From the time evolution of the Joule heating given in figure 3.21, we see that the Joule heating in middle chromosphere increases with time for 5 min until it stabilizes around $0.05\ \mathrm{erg\,s^{-1}\,cm^{-3}}$, which is slightly less than in the standard model. In both the upper chromosphere and lower TR, the Joule heating increases for about 25-30 min and stabilizes around $0.015\ \mathrm{erg\,s^{-1}\,cm^{-3}}$, i.e. slightly less than in the standard model. Since the coronal temperatures stays lower than 0.7 MK for the first 45 min, region 4 represents the entire corona in that period with a Joule heating less than $0.002\ \mathrm{erg\,s^{-1}\,cm^{-3}}$. As soon as the coronal temperatures gets higher than 0.7 MK, this region represents the upper TR, having a Joule heating about $0.01\ \mathrm{erg\,s^{-1}\,cm^{-3}}$ after 65 min and increasing rapidly. The coronal Joule heating increases constantly with time and is about $0.0003\ \mathrm{erg\,s^{-1}\,cm^{-3}}$ after 65 min, i.e. less than 1/3 of that in the standard model. This simulation should ideally have run for a longer time to see which values the Joule heating stabilizes at. However, we can conclude that this model obtains a much less coronal heating than the standard model and the magnetic bipole model, but still more than the monopole model.

Figure 3.8(b) shows that this model has a well-organized set of vertical current sheets. A few current sheets go diagonally between the regions above two of the opposite-lying magnetic poles (with the same polarity), and from these poles, current sheets also go diagonally out of this box towards other poles with the same polarity (remembering the periodicity of the box), while poles of the opposite polarity will lie in-between these current sheets. The current sheets are weaker than those seen in the bipole model, and they also have a simpler structure, which may be a reason why this model has much less coronal heating. Along each current sheet, the (almost vertical) magnetic field on one side of the sheet is tilted in a slightly different direction than on the other side, as seen in figure 3.9, which give rise to the strong currents inside the sheet. Closer analysis of the time evolution of the current density reveals that a series smaller (and weaker) current sheets appear from time to time (but not constantly) nearby and parallel to current sheets seen on this figure, i.e. a hierarchy of current sheets. The hierarchy of current sheets are shown in figure 3.14.

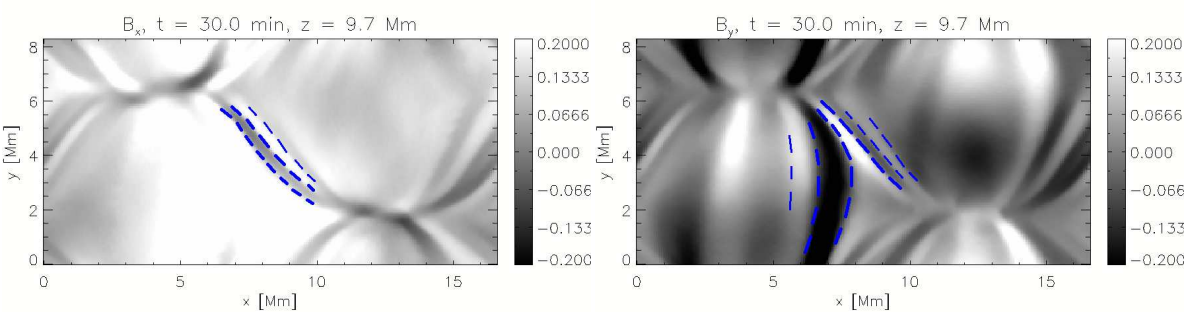

Figure 3.9: The horizontal components of the magnetic field (measured in gauss) in C2x2, $z = 9.7$, $t = 30.0$ min. The magnetic field behaves more or less like this throughout the corona. Some of the current sheets are marked with dashed lines.

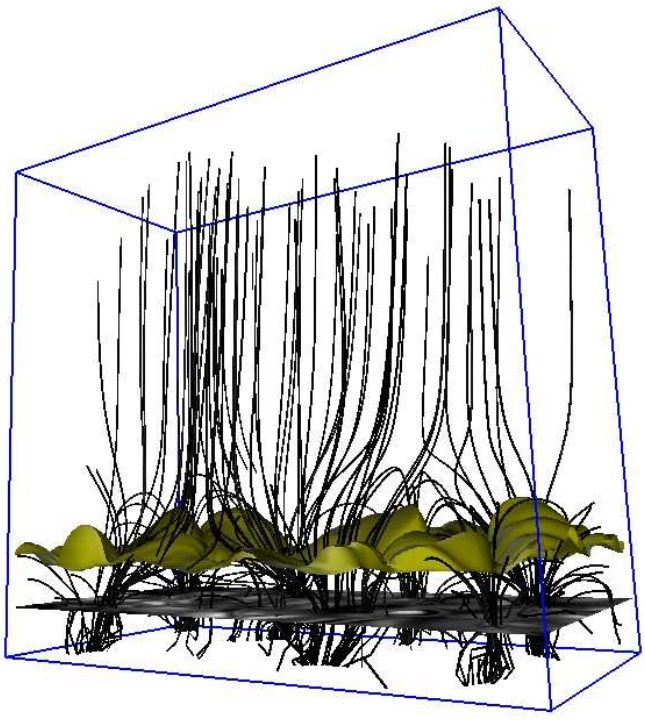

Figure 3.10: Three-dimensional plot of the magnetic field in model C4x2, evaluated at $t = 80.0$ min. The horizontal plane with the granulation pattern marks the location of the photosphere, while the above-lying curved surface marks the center of the TR ($T = 10^5$ K).

3.6 The Magnetic 8-pole Model C4x2

3.6.1 Magnetic Fields

Again, we double the photospheric magnetic complexity of the previous model to get this model with 8 poles of vertical magnetic fields in the photosphere, as seen in figures 3.10 and 3.16(b). Above the photosphere, the fields from the different poles bend out and connect together in loops reaching up to the canopy which here is located at 3.8 Mm above the photosphere, which is higher than in the previous model, despite the shorter mean separation distance between poles in the photosphere. Thus, the canopy is slightly above the transition region. As in the previous model, the magnetic field above the canopy in this model is more or less vertical.

According to figures 3.17 and 3.18, the lower boundary features a magnetic field even stronger than in the previous models, with an energy density more than 3 times that of the standard model (i.e. $\sim 1.5\ \mathrm{erg\,cm^{-3}}$). Again, the average photospheric field is approximately equally strong as in the other models, but the magnetic complexity which is even higher than in the quadrupole model results in an even weaker coronal magnetic field, with an energy density at the upper boundary of order $10^{-4}\mathrm{erg\ cm^{-3}}$, i.e. 1/10 of that in the quadrupole model and 10 times that in the standard model.

3.6.2 Temperature Structure

The coronal temperature in this model decreases slowly during the first 20-25 min before it starts increasing and is about 1.75 MK and still increasing after 80 min, as seen in figures 3.11(a) and 3.20(c). Comparing how the coronal temperature evolves in time in this model to the previous models, this model is likely to end up with a higher coronal temperature than than the standard model, but lower than the bipole and quadrupole models (unless the temperature in the quadrupole model stops increasing before this model does). The height of the TR varies between 1.2 Mm an 3.5 Mm above the photosphere, although it is mostly lower than 3.0 Mm. The temperature in the region below the TR behaves similar to the standard model temperature.

3.6.3 Joule Heating

From the time evolution of the Joule heating in figure 3.22, we see that the heating of middle chromosphere increases the first 10-15 min and then stabilizes around $0.06\ \mathrm{erg\,s^{-1}\ cm^{-3}}$ i.e. slightly more than in the standard model. The heating of the upper chromosphere increases during the first 40-50 min and ends up about $0.025\ \mathrm{erg\,s^{-1}\ cm^{-3}}$ after 80 min, i.e. similar to the value which the standard model stabilized around. The TR Joule heating increases throughout the entire simulation and ends up about $0.022\ \mathrm{erg\,s^{-1}\ cm^{-3}}$ in the lower TR and about $0.020\ \mathrm{erg\,s^{-1}\ cm^{-3}}$ in the upper TR after 80 min (i.e. similar to that in the standard model lower TR and a bit more than in the standard model upper TR). The coronal Joule heating increases also throughout the simulation, ending up about $0.00025\ \mathrm{erg\,s^{-1}\ cm^{-3}}$, i.e. 1/4 of that in the standard model.

From figure 3.11(b), we see that this model obtains a current sheet structure very similar to the quadrupole model, but because of the shorter distances between the poles of magnetic fields which emerge

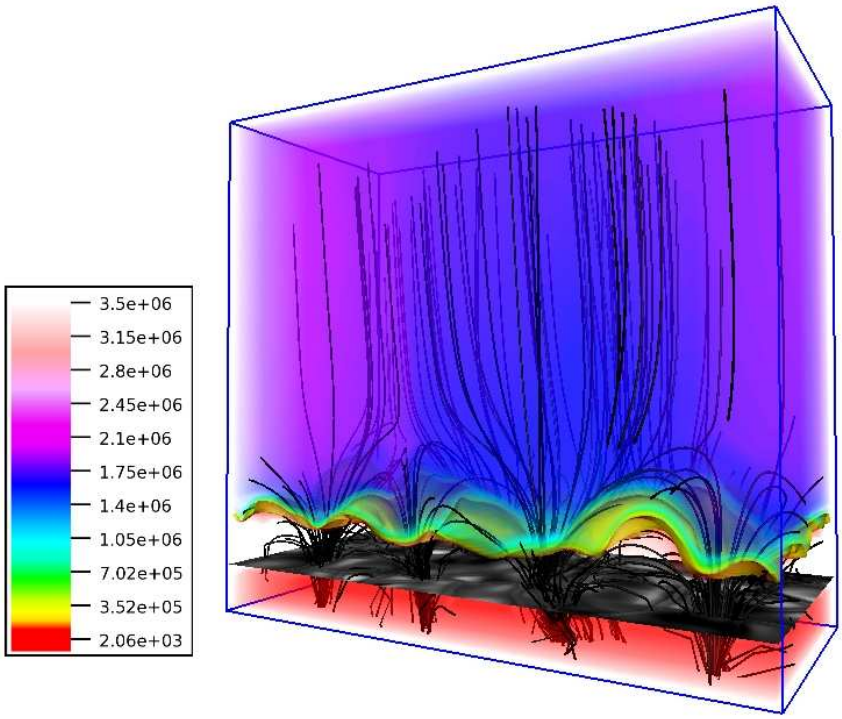

(a) C4x2, temperature and magnetic fields at $t = 80.0$ min.

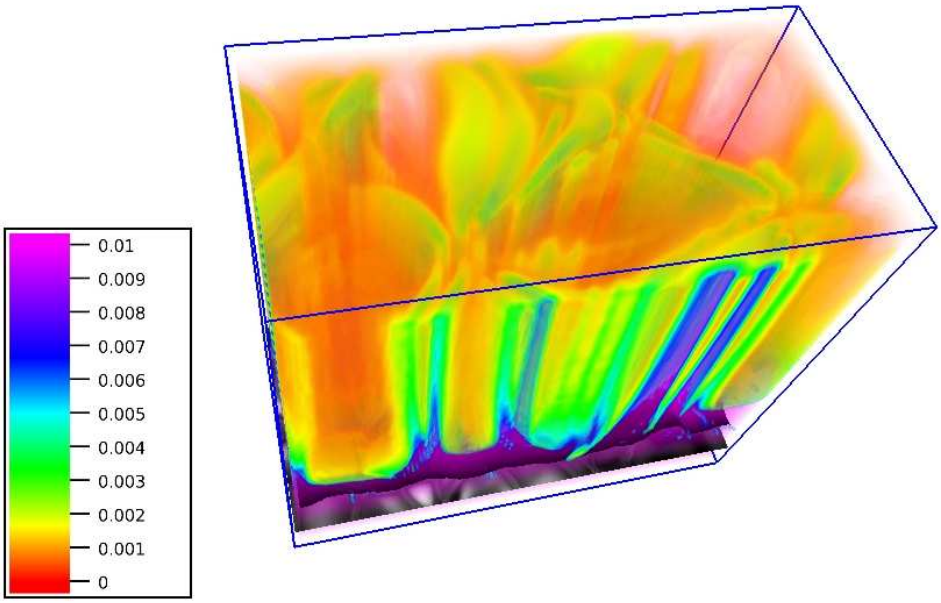

(b) C4x2, current density relative to the typical chromospheric current density, $J/J_{\rm chr}^{\rm B1}$, at $t = 80.0$ min. Current densities much higher than the peak value in this plot occurs near the TR and below, but is ignored to make the *coronal* currents more visible.

Figure 3.11: Three-dimensional plot of (a) temperature and magnetic field and (b) current density in model C4x2. The horizontal plane with the granulation pattern marks the location of the photosphere, while the above-lying curved surface marks the center of the TR ($T = 10^5$ K).

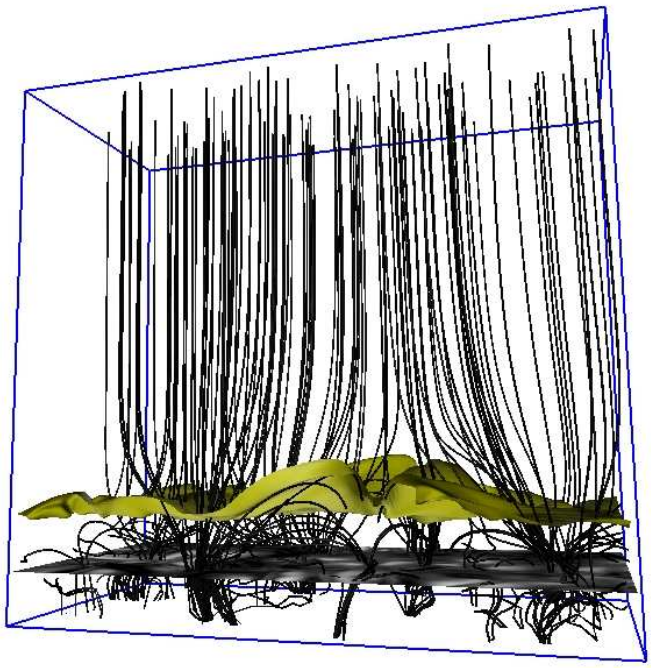

Figure 3.12: Three-dimensional plot of the magnetic field in model C4x3, evaluated at $t = 80.0$ min. The horizontal plane with the granulation pattern marks the location of the photosphere, while the above-lying curved surface marks the center of the TR ($T = 10^5$ K).

from the photosphere, the distance between the current sheets are correspondingly shorter. Closer studies of the time evolution of the current sheets reveal that this model does not get as complex hierarchy of current sheets as the quadrupole model does, and this may explain why this model has significantly less coronal heating. The structure of current sheets are shown (and compared to the quadrupole model) in figure 3.14

3.7 C4x3, a Model with (initially) 12 Magnetic Poles

3.7.1 Magnetic Fields

This model has initially 12 poles of vertical magnetic fields at the lower boundary, as seen in figure 3.16(c), and, as in the other models, these poles reaches into the photosphere where the magnetic fields are forced into the intergranular lanes, and follows the same pattern for a while (figure 3.16(d)). However, because the separation distance between the magnetic poles are almost comparable to the granule size, one of these poles seems to disappear at the later stages of the simulation, and another becomes quite weak. Additionally, because of the periodicity of the box, one or two of the poles which lies near one of the side-walls in the xz-plane (i.e. the two largest side-walls) seems to merge more or less together with poles of same polarity near the the opposite side-wall. That gives this model an *effective complexity* in the photospheric magnetic field which is slightly lower than in the

previous model. As seen in figure 3.12, magnetic fields from the different poles connect together in loops reaching up to the canopy which in this model is located 3.3 Mm above the photosphere. As in the previous two models, a weaker vertical magnetic field rises above the canopy.

As seen in figured 3.17 and 3.18, the magnetic field at lower boundary is even stronger than in the previous model, with an energy density more than 4 times that in the standard model. The field gets weaker with height, with the photospheric field being on average equally strong as in the other models, but with a coronal field which is stronger than in the previous model and only slightly weaker than in the quadrupole model, with an energy density about 60 times that in the standard model. The reason this model gets a stronger coronal field than the 8-pole model is probably because this model has an initial density of magnetic poles which is so high that a larger fraction of the field is forced to continue vertically through the corona than in the 8-pole model. Thus, the coronal field strength does not decrease monotonically with the complexity of the magnetic field in the photosphere (while the average photospheric field strength is kept constant), but reaches a minimum value for a certain complexity (near that of the 8-pole model) before it increases with complexity.

3.7.2 Temperature Structure

From figure 3.13(a), 3.20(e) and 3.20(f), we can see that, amongst those models which have a magnetic complexity (i.e. all except the magnetic monopole model), this is the one which has the coolest corona, reaching coronal temperatures between 0.8 MK and 1.0 MK and a mean coronal temperature of approximately 0.9 MK after 80 min, which is about 3/5 of the mean temperature which the standard model corona obtains after 60 min. The height of the TR varies between 1.5 Mm and 3.5 Mm above the photosphere, although it is mostly lower than 3.0 Mm. As in the other models, the temperature profile below the TR behaves mostly similar to that of the standard model.

3.7.3 Joule Heating

From the time evolution of the Joule heating in this model given in figure 3.22, we see that the heating of the middle chromosphere increases with time the first 15 min and then stabilizes around $0.055\ \mathrm{erg\,s^{-1}\,cm^{-3}}$, similar to the heating rate in the standard model middle chromosphere. The upper chromosphere has a heating rate which increases for the first 30 min, then stabilizes around $0.015\ \mathrm{erg\,s^{-1}\,cm^{-3}}$ i.e. slightly less than in the standard model. The heating of the TR increases slowly with time through the entire simulation (ignoring some oscillations) and ends up around $0.015\ \mathrm{erg\,s^{-1}\,cm^{-3}}$ in the lower TR (half of that in the standard model) and about 0.0025 in the upper TR (1/5 of that in the standard model). The coronal heating increases very slowly with time, ending up about $0.0001\ \mathrm{erg\,s^{-1}\,cm^{-3}}$ i.e. 1/10 of that in the standard model.

Figure 3.13(b) shows that the corona in this model also has a structure of vertical current sheets that is similar to that in the previous model. Closer analysis of the current sheets in this model reveals a hierarchy of current sheets almost as complex as in the quadrupole model. However, that analysis (not shown in any figure here) also reveals that the currents in the current sheets tend to be weaker, which may explain why this model has a lower coronal heating than both of the previous two models.

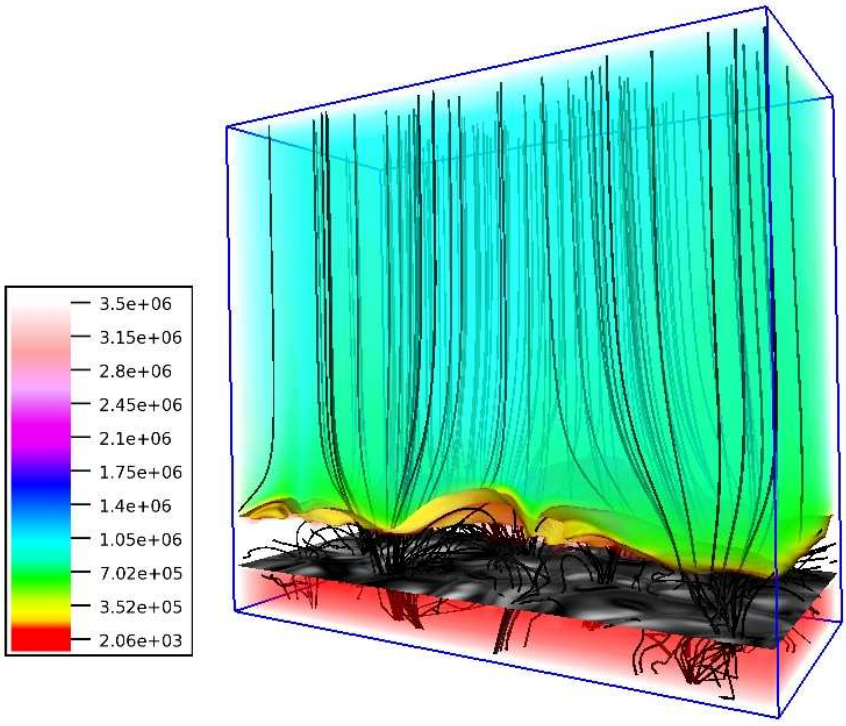

(a) C4x3, temperature and magnetic fields at $t = 80.0$ min.

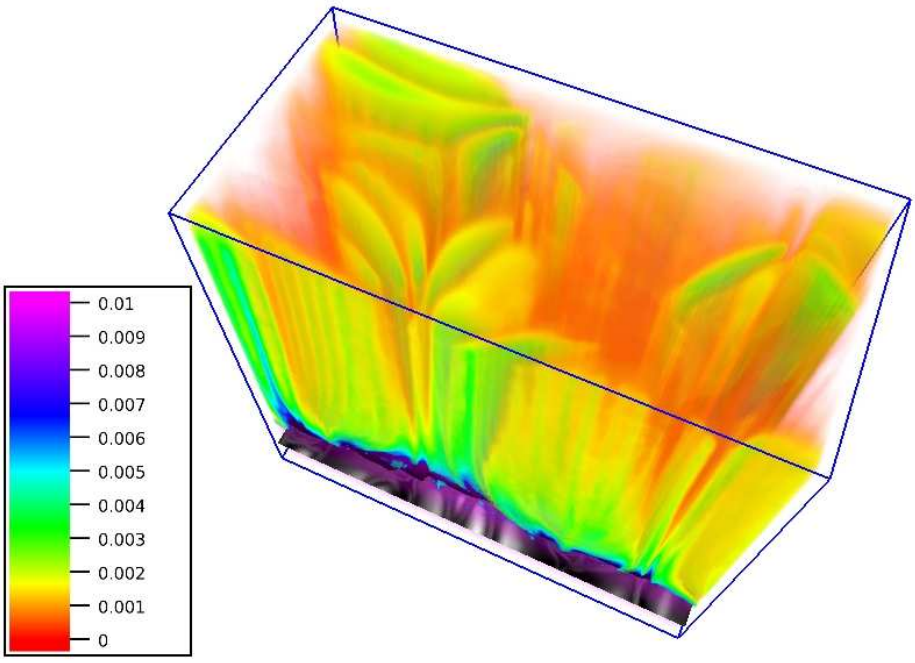

(b) C4x3, current density relative to the typical chromospheric current density, $J/J_{\rm chr}^{\rm B1}$, at $t = 80.0$ min. Current densities much higher than the peak value in this plot occurs near the TR and below, but is ignored to make the *coronal* currents more visible.

Figure 3.13: Three-dimensional plot of (a) temperature and magnetic field and (b) current density in model C4x3. The horizontal plane with the granulation pattern marks the location of the photosphere, while the above-lying curved surface marks the center of the TR ($T = 10^5$ K).

3.8 Comparing the Results of the Different Models

3.8.1 Magnetic Fields

All five models evolved in this thesis keep a relatively simple and organized magnetic field structure during the simulations, compared to the standard model. The simplest magnetic field structure is seen in the magnetic monopole model C1x1, where the field stays more or less vertical and homogeneous throughout the simulation, except the photospheric field which follows the granular pattern. The other four models have poles at lower boundary where concentrations of vertical fields rise up through the photosphere, bend outwards above the photosphere where parts of the fields from different poles connect together in loops which reach up to the *canopy*, while the rest of the fields continue almost vertically upwards above the canopy.

Closer analysis of the models (not shown in any figure here) reveals estimates of the canopy height in each model – defined as the height where the horizontal plane is tangent to the uppermost magnetic loops which bind together fields from the different poles – which are written in table 3.1. As expected, the highest canopy height occurs in the bipole model C2x1, where the separation distance between magnetic poles is highest, and as we see from figure 3.18, the magnetic field above the canopy in this model is much more inclined than on similar heights in the other models. The three models with magnetic fields of higher complexity have canopy heights near or within the transition region. However, the canopy height does not seem to decrease with increasing magnetic complexity within those three models. That can be caused by the fact that the fluid dynamics forces the magnetic canopy (which binds the different poles together) to lie near the TR (and that the TR tries to align itself with the canopy), causing the exact height of the canopy to be a bit random. The standard model have magnetic loops which is chaotically located all over the corona, and it is therefore futile to measure a specific canopy height in that model.

Model	Canopy height
C1x1	–
C2x1	5.6 Mm
C2x2	3.4 Mm
C4x2	3.8 Mm
C4x3	3.3 Mm

Table 3.1: Height above photosphere where the top of magnetic canopy occurs.

Comparing the plots of the horizontally averaged magnetic field components and especially magnetic energy density as function of height in figure 3.18, one can observe the following: the magnetic field at the lower boundary has an average which increases with the complexity in a way that ensures the mean magnetic field strength in the photosphere to be approximately the same in all models. Because the fraction of the field emerging through the photosphere which connects together in loops increases with the density of magnetic poles for densities less than that of the 8-pole model, the magnitude of the remaining magnetic field above the canopy decreases with the complexity in the photospheric field for all models except model C4x3 which has a stronger coronal field than the 8-pole model.

Considering the periodicity of the box and imagining putting several boxes together, the magnetic monopole model will correspond to a larger area of homogeneous magnetic fields (a “quiet quiet-

Sun" region). Such kind of homogeneous vertical fields occur in an active region-phenomenon known as *plage*, but plage regions tends to be warmer the surrounding QS regions, in contrast to what we saw in the monopole model. There is currently no good explanation for the high temperatures which occurs in plage. The magnetic field configuration in the bipole model will correspond to a line of magnetic poles bound together in magnetic loops which reach into the corona. The supergranular lanes, where magnetic fields are much stronger than in the internetwork, might consist of such lines of magnetic poles. The three models of higher magnetic complexity will all correspond to grids of magnetic poles, bound together in loops reaching up to a canopy near the TR, but with different grid sizes. Such grids of magnetic poles may represent a simplified version of the salt-pepper pattern of magnetic fields in the QS internetwork. The standard model represents a more realistic salt-pepper pattern of magnetic fields in the internetwork.

3.8.2 Temperature Structure

The model which in which we find the lowest coronal temperature is definitely the magnetic monopole model, which ends up with a mean temperature about 0.2 MK. That model has also the most constant location of the TR. The opposite extreme is the bipole model, which after 40 min reaches a mean coronal temperature of almost 15 times that in the monopole model ($\sim$3.0 MK) and temperatures up to 3.5 MK in a smaller region. That model also has the highest temperature variance in the corona (all between 1.7 MK and 3.5 MK).

The three models of higher magnetic complexity reach temperatures in between those of the monopole model and the bipole model. Those three models also have the highest variance in the TR height. Amongst those models, the quadrupole model, which has the lowest density of magnetic poles in the photosphere, has the highest coronal temperature, reaching 1.7 MK after 63 min when it is still increasing rapidly. The coronal temperature in the 8-pole model reaches 1.2 MK within the same time interval and continues to increase, but slower than the quadrupole model. The model C4x3 reaches a coronal temperature of 0.6 MK at that time and continues to increase, but more slowly than in the previous two models, and it seems to end up with the coolest corona of those three models. Thus, amongst those three models, the resulting coronal temperature seems to decrease with the *initial* complexity in the photospheric magnetic field (C4x3 had initially the highest photospheric complexity).

The standard model ends up with a coronal temperature slightly lower than in the 8-pole model despite having a much higher coronal Joule heating. We must remember that the coronal temperature might be affected by other factors than the Joule heating. A possible mechanism which keeps the coronal temperature in this model down could be cooler gas which is transported up to coronal heights in coronal loops, or it could be radiative cooling.

3.8.3 Joule Heating

Table 3.2 shows the mean Joule heating which each region in each model ends up with. By using this and figures 3.21 and 3.22 to compare the Joule heating in each model, it is clearly that the Joule heating in the middle chromosphere increases more or less with the effective complexity in the photospheric magnetic field (where C4x3 had a lower effective complexity than the 8-pole model). In all of the above-lying regions, the magnetic bipole model seems to have the highest amount of Joule heating,

and especially in the corona, the Joule heating is much higher than in the other models. Of the three models of higher magnetic complexity, the 8-pole model has the highest amount of Joule heating in the upper chromosphere and TR, while the quadrupole model has the highest coronal Joule heating. Model C4x3 has an almost equal amount of Joule heating as the quadrupole model in the upper chromosphere, but has a lower amount of Joule heating than both the quadrupole and 8-pole model in the above-lying regions. Thus, the coronal Joule heating decreases with the initial complexity in the photospheric magnetic field amongst those three models. The magnetic monopole model has a Joule heating, in the upper chromosphere and above, which is much lower than in all of the other models.

The large amount of Joule heating in the magnetic bipole model, which heats the corona up to temperatures of 2.5-3.5 MK, is most probably due to the strong current sheets which are generated in the region near the magnetic neutral line and reach out through large parts of the corona. It is also possible that the generation of nanoflares due to twisting and reconnection of magnetic fields is present below the canopy, heating the sub-canopy corona (since the canopy lies relatively high up in the corona).

The corona in the three models of higher magnetic complexity, which contain "grids" of magnetic poles, are all heated by a corresponding grid of vertical current sheets which go diagonally between the magnetic poles with the same polarity (while the poles of opposite polarity lies in the middle of each "grid zone"), as seen in the three-dimensional plots of the current density earlier in this chapter. Of these models, the quadrupole model gets the largest amount of coronal heating, even though the 8-pole model have a tighter grid of current sheets (due to a higher complexity in the photospheric field) with currents approximately equally strong as in the quadrupole model. This may be explained by the fact that the quadrupole model seems to obtain a more complex *hierarchy* of weaker current sheets within each "current sheet grid zone" than the 8-pole model does, as seen in figure 3.14. The model C4x3, which has a lower effective complexity in the photospheric magnetic field than the 8-pole model, also seems to get a bit more complex hierarchy of current sheets within each "grid zone", but the currents in this model are weaker than in the other two "magnetic grid"-models, which may explain why this model gets less coronal Joule heating. The reason why the strongest current sheets in this model are weaker than in the other two similar model may be explained the following way: this model has an initially too high complexity in the photosphere (12 poles), with separation distances comparable to a typical granule size. Therefore, some of the loops that bind fields from different poles together happens to lie very near the photosphere and eventually "drown" beneath the photosphere, making the photospheric field much weaker than in the other models at the latter stages of the simulation. Thus, even though having a lower density of magnetic poles in the photosphere than the quadrupole 8-pole model, which leads to a larger hierarchy of current sheets, the field is much weaker, and therefore the current sheets which are generated in the corona are too weak to heat it more than in the 8-pole model. Another factor which can play a role here is the generation of nanoflares, which is more likely to happen below the canopy than above. The canopy in the quadrupole and 8-pole models reach a bit higher into the corona than in the model C4x3 (where the canopy is mostly below the TR) and thus makes it more probable for nanoflares to reach into the corona and heat it.

The reason the magnetic monopole model has much less coronal heating than the other models is due to the absence of strong currents. The fact that the corona still manage to maintain a temperature in the order of 10^5 K may be explained by the generation of weak nanoflares, since the vertical fields in this model might twist around each other (due to convective motion) and reconnect all the time.

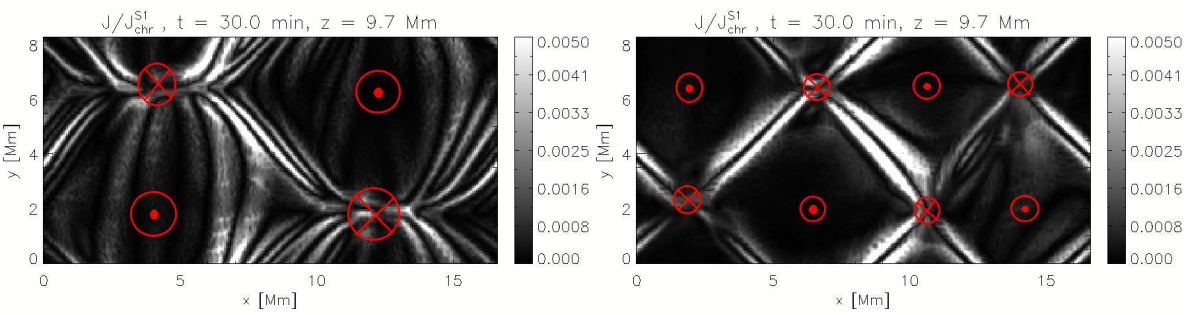

Figure 3.14: Current density, relative to the typical chromospheric current density, in C2x2 (left panel) and C4x2 (right panel), $z = 9.7$ Mm, $t = 30.0$ min. The currents behave similar to this throughout the entire corona. The horizontal locations of poles of upward- and downward-oriented fields (in the photosphere) are marked by $\odot$ and $\otimes$, respectively.

Model	$\langle Q_{\rm J}^{(1)} \rangle$[erg/s]	$\langle Q_{\rm J}^{(2)} \rangle$[erg/s]	$\langle Q_{\rm J}^{(3)} \rangle$[erg/s]	$\langle Q_{\rm J}^{(4)} \rangle$[erg/s]	$\langle Q_{\rm J}^{(5)} \rangle$[erg/s]
B1	$5.4 \cdot 10^{-2}$	$2.4 \cdot 10^{-2}$	$2.3 \cdot 10^{-2}$	$1.4 \cdot 10^{-2}$	$1.1 \cdot 10^{-3}$
C1x1	$1.3 \cdot 10^{-2}$	$1.0 \cdot 10^{-4}$	$1.1 \cdot 10^{-5}$	$1.7 \cdot 10^{-5}$	$1.7 \cdot 10^{-5}$
C2x1	$4.2 \cdot 10^{-2}$	$3.0 \cdot 10^{-2}$ (*)	$2.9 \cdot 10^{-2}$ (*)	$3.1 \cdot 10^{-2}$ (*)	$3.1 \cdot 10^{-3}$ (*)
C2x2	$5.2 \cdot 10^{-2}$	$1.6 \cdot 10^{-2}$	$1.3 \cdot 10^{-2}$	$1.0 \cdot 10^{-2}$	$3.0 \cdot 10^{-4}$ (*)
C4x2	$6.3 \cdot 10^{-2}$	$2.6 \cdot 10^{-2}$	$2.1 \cdot 10^{-2}$	$1.7 \cdot 10^{-2}$ (*)	$2.5 \cdot 10^{-4}$ (*)
C4x3	$5.6 \cdot 10^{-2}$	$1.5 \cdot 10^{-2}$	$1.5 \cdot 10^{-2}$	$2.6 \cdot 10^{-3}$ (*)	$1.2 \cdot 10^{-4}$ (*)

Table 3.2: The mean Joule heating which each model ends up with in each of the 5 selected regions. In the cases where the Joule heating has not yet stabilized, marked with (*), the heating is evaluated over the last 5-10 min. Otherwise, the heating is an average over the period after it gets more or less stable.

Model	$\frac{\langle Q_{\rm J}^{(1)} \rangle}{\langle Q_{\rm J}^{(1,{\rm B1})} \rangle}$	$\frac{\langle Q_{\rm J}^{(2)} \rangle}{\langle Q_{\rm J}^{(2,{\rm B1})} \rangle}$	$\frac{\langle Q_{\rm J}^{(3)} \rangle}{\langle Q_{\rm J}^{(3,{\rm B1})} \rangle}$	$\frac{\langle Q_{\rm J}^{(4)} \rangle}{\langle Q_{\rm J}^{(4,{\rm B1})} \rangle}$	$\frac{\langle Q_{\rm J}^{(5)} \rangle}{\langle Q_{\rm J}^{(5,{\rm B1})} \rangle}$
C1x1	0.25	0.004	0.0005	0.001	0.0015
C2x1	0.77	1.3 (*)	1.2 (*)	2.1 (*)	2.8 (*)
C2x2	0.96	0.66	0.55 (*)	0.71 (*)	0.27 (*)
C4x2	1.2	1.1	0.91 (*)	1.2 (*)	0.23 (*)
C4x3	1.0	0.64	0.65 (*)	0.18 (*)	0.11 (*)

Table 3.3: The mean Joule heating which each model ends up with in each of the 5 selected regions, relative to the mean Joule heating in the corresponding region in the standard model. In the cases where the Joule heating has not yet stabilized, marked with (*), the heating is evaluated over the last 5-10 min. Otherwise, the heating is an average over the period after it gets more or less stable.

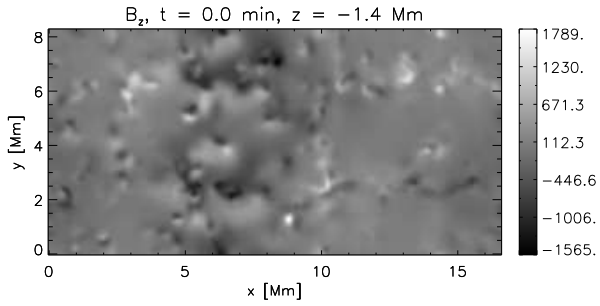

(a) Model B1, B_z at lower boundary at $t = 0$ s.

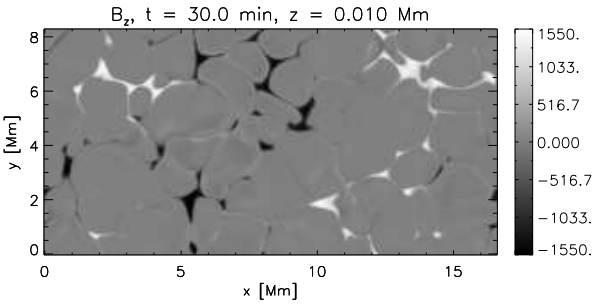

(b) Model B1, B_z in the photosphere at $t = 30.0$ min.

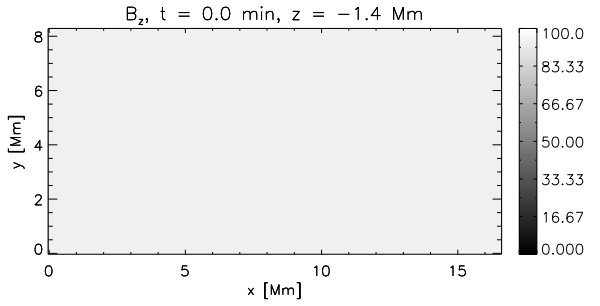

(c) Model C1x1, B_z at lower boundary at $t = 0.0$ min.

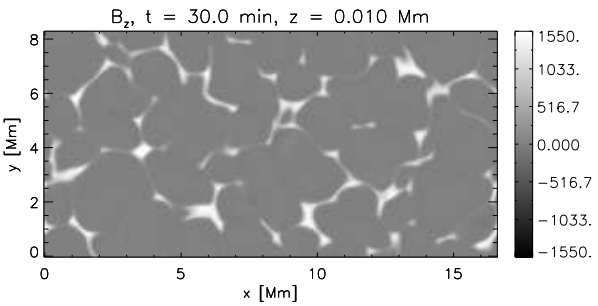

(d) Model C1x1, B_z in the photosphere at $t = 30.0$ min.

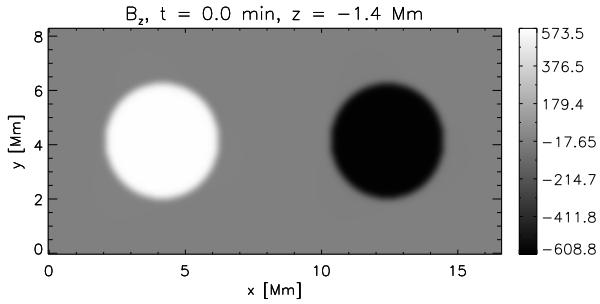

(e) Model C2x1, B_z at lower boundary at $t = 0$ s.

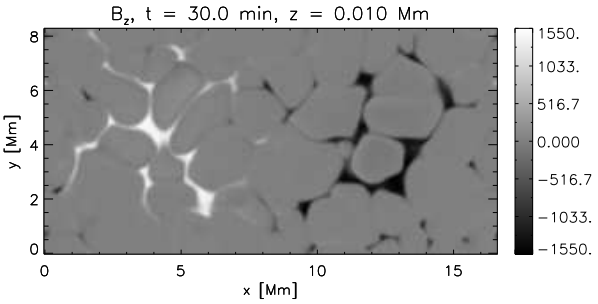

(f) Model C2x1, B_z in the photosphere at $t = 30.0$ min.

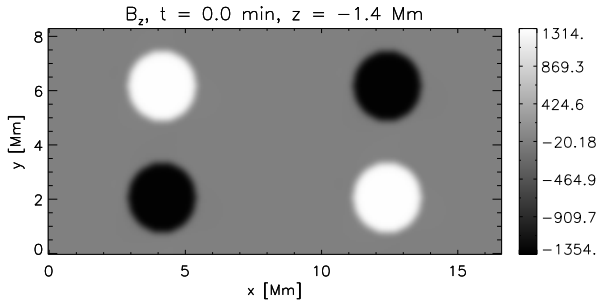

(g) Model C2x2, B_z at lower boundary at $t = 0$ s.

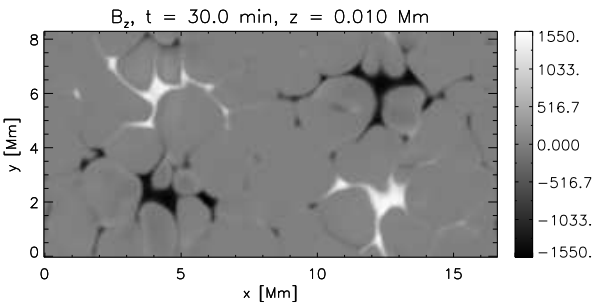

(h) Model C2x2, B_z in the photosphere at $t = 30.0$ min.

Figure 3.15: Initial B_z at the lower boundary and B_z in the photosphere after some relaxation time, measured in gauss.

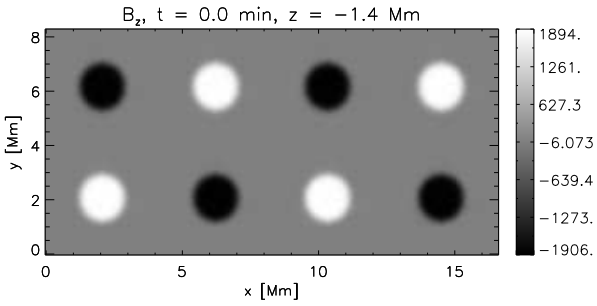

(a) Model C4x2, B_z at the lower boundary at $t = 0$ s.

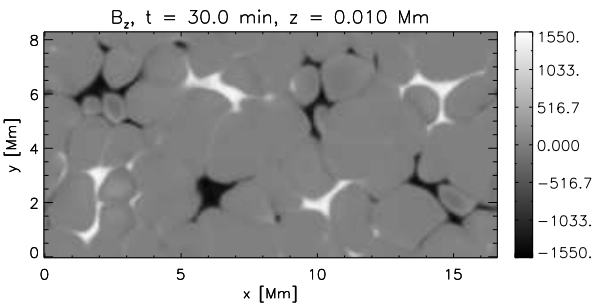

(b) Model C4x2, B_z in the photosphere at $t = 30.0$ min.

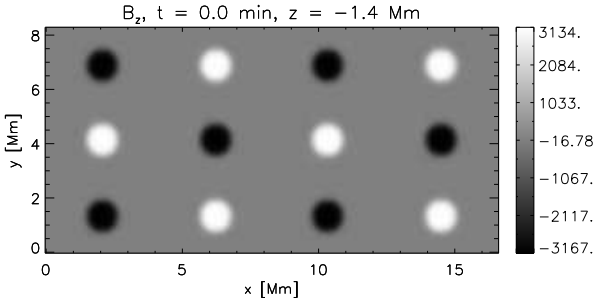

(c) Model C4x3, B_z at the lower boundary at $t = 0$ s.

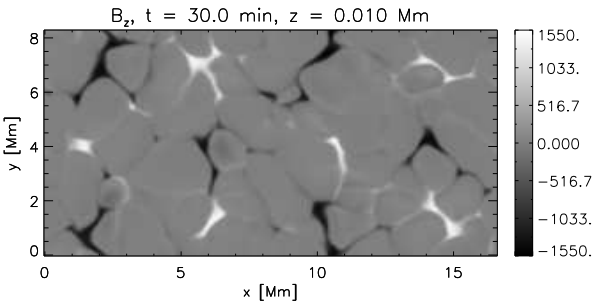

(d) Model C4x3, B_z in the photosphere at $t = 30.0$ min.

Figure 3.16: Initial B_z at the lower boundary and B_z in the photosphere after some relaxation time, measured in gauss.

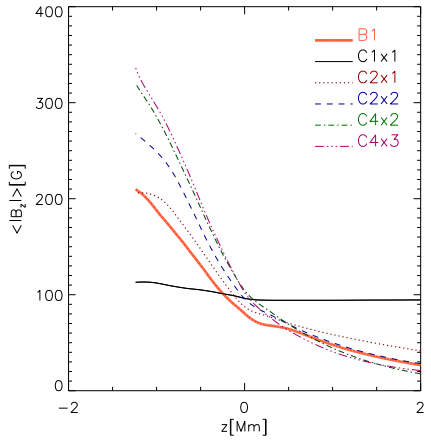

(a) Mean $|B_z|$ in the lower depths.

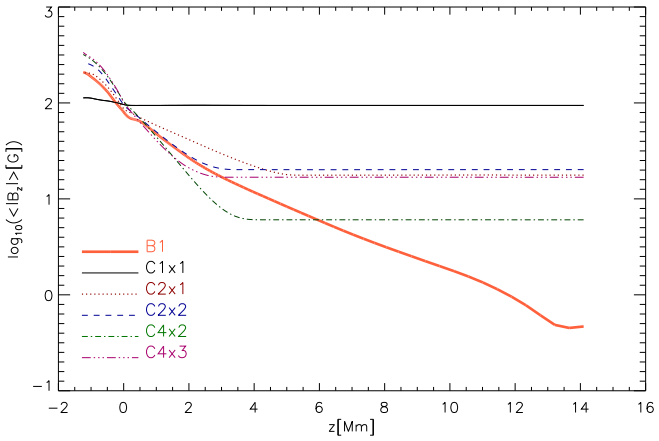

(b) Log mean $|B_z|$.

Figure 3.17: Plots of mean $|B_z|$ as function of height at $t = 40.0$ min.

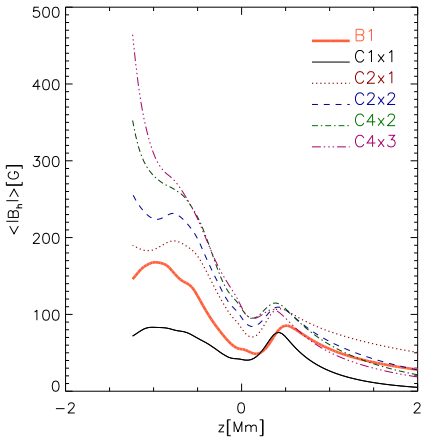

(a) Mean B_h in the lower depths.

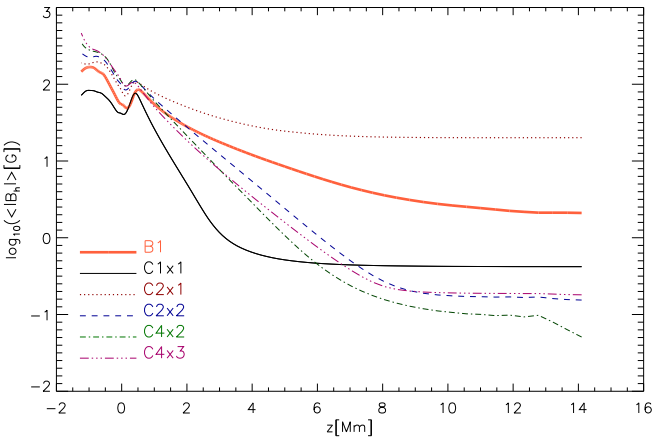

(b) Log mean B_h.

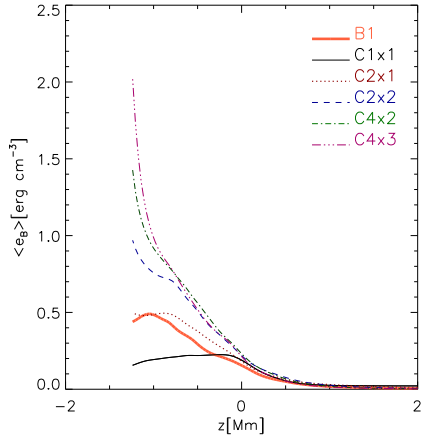

(c) Mean e_B in the lower depths.

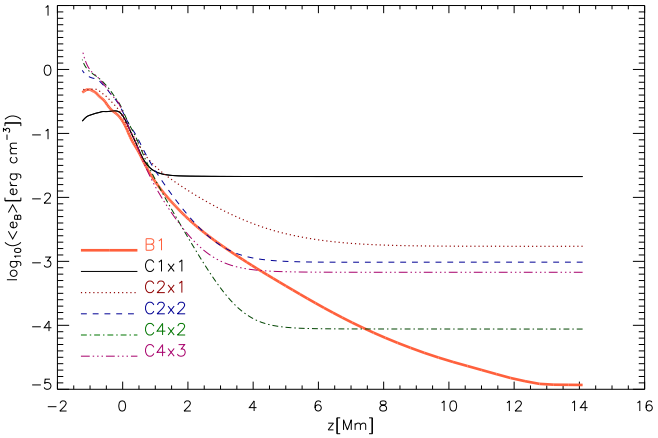

(d) Log mean e_B.

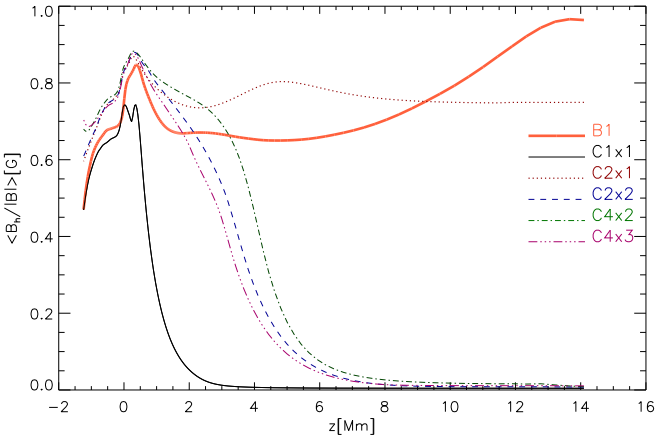

(e) Mean $|\sin\theta|$.

Figure 3.18: Plots of the mean $B_h \equiv \sqrt{B_x^2 + B_y^2}$, field inclination $\sin\theta \equiv B_h/|\mathbf{B}|$ and magnetic energy density $e_B = B^2/2\mu$ as function of height at $t = 40.0$ min

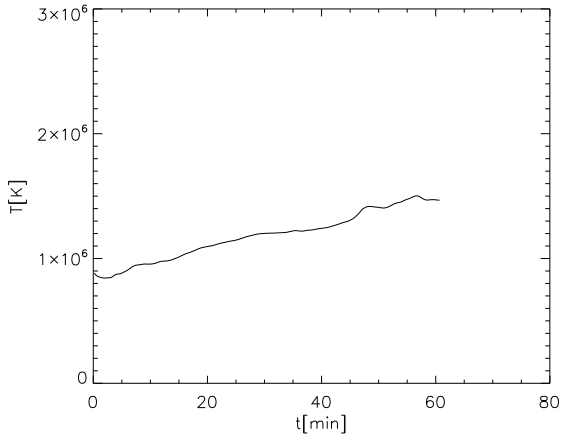

(a) $\langle T \rangle$ at $z > 3$ Mm, B1

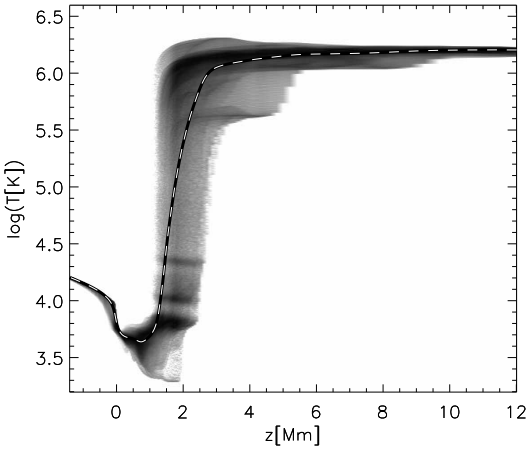

(b) Temperature histogram for B1, $t = 60.7$ min.

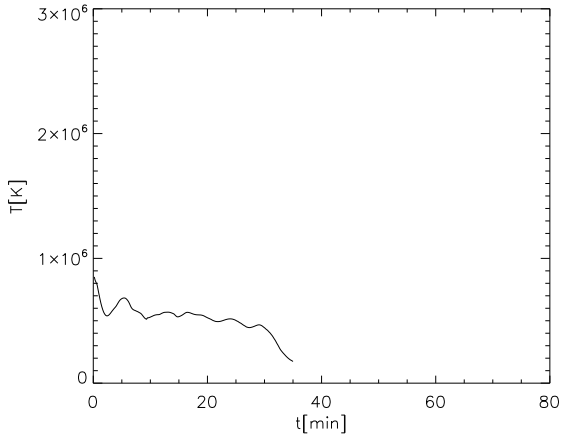

(c) $\langle T \rangle$ at $z > 3$ Mm, C1x1

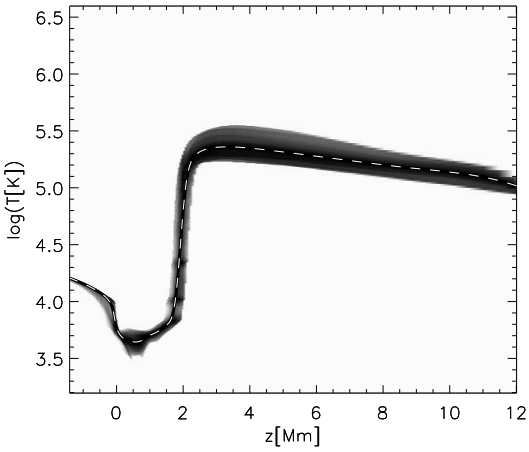

(d) Temperature histogram for C1x1, $t = 35.0$ min.

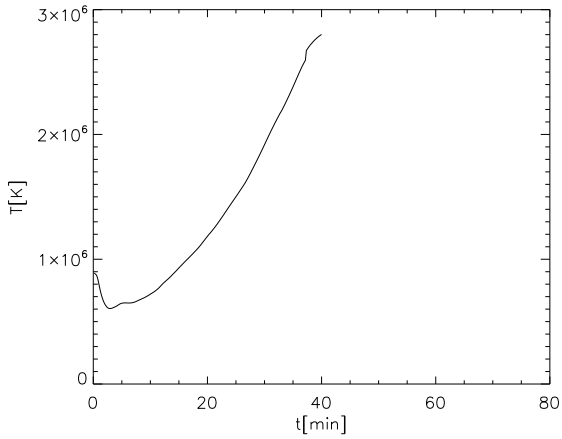

(e) $\langle T \rangle$ at $z > 3$ Mm,C2x1

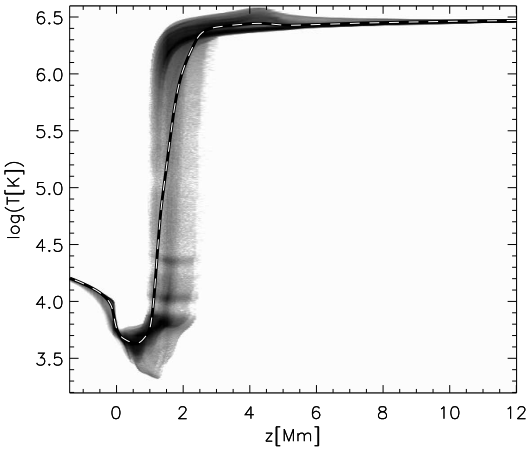

(f) Temperature histogram for C2x1, $t = 40.0$ min.

Figure 3.19: Left panels shows how the mean temperature in the regions above $z = 3.0$ Mm evolve in time, while right panels shows temperature histogram and mean temperature as function of height (dashed line).

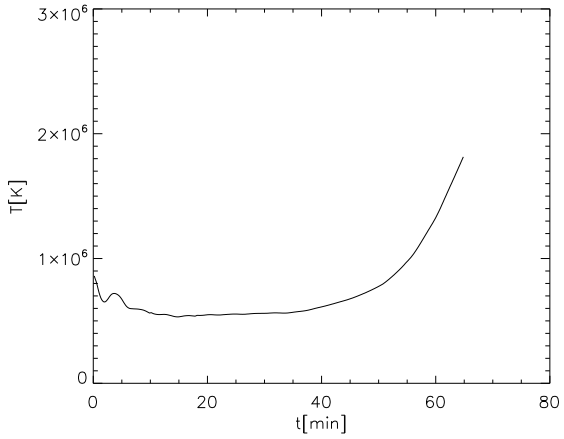

(a) $\langle T \rangle$ at $z > 3$ Mm, C2x2

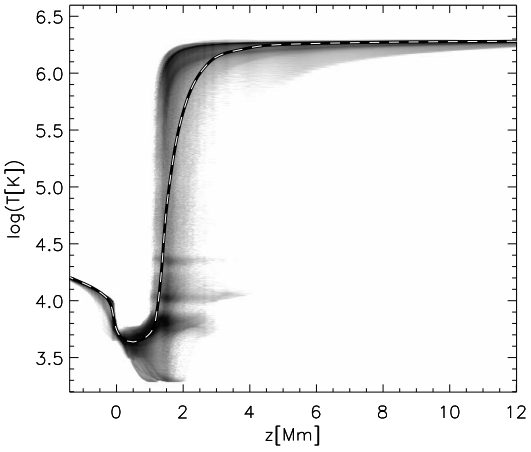

(b) Temperature histogram for C2x2, $t = 65.0$ min.

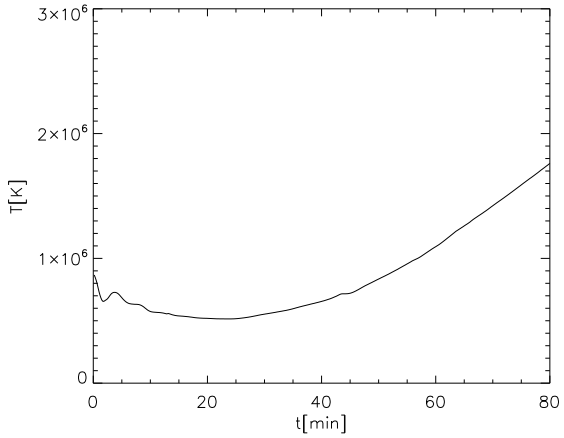

(c) $\langle T \rangle$ at $z > 3$ Mm,C4x2

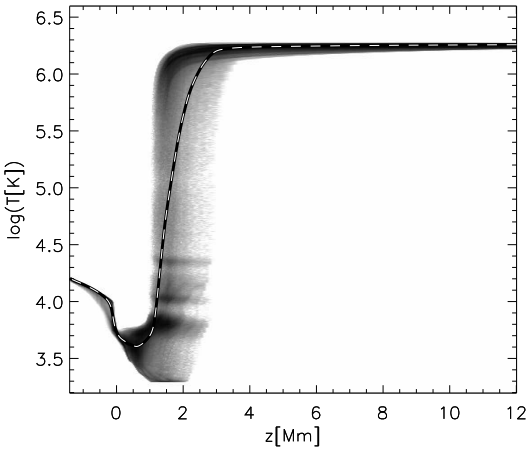

(d) Temperature histogram for C4x2, $t = 80.0$ min.

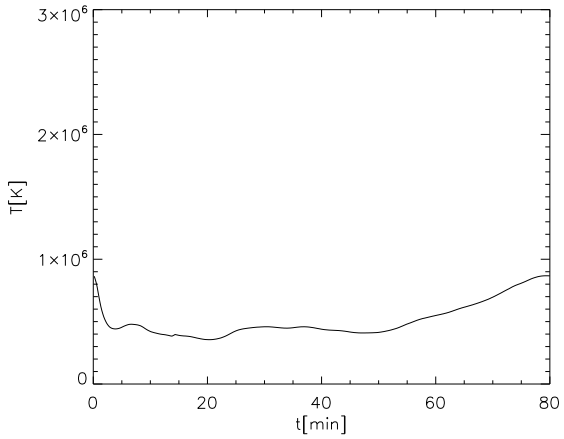

(e) $\langle T \rangle$ at $z > 3$ Mm, C4x3

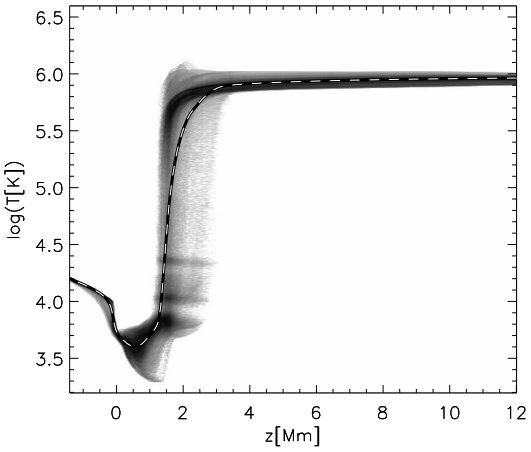

(f) Temperature histogram for C4x3, $t = 80.0$ min.

Figure 3.20: Left panels shows how the mean temperature in the regions above $z = 3.0$ Mm evolve in time, while right panels shows temperature histogram and mean temperature as function of height (dashed line).

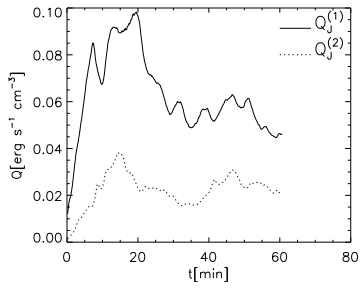

(a) B1, chromosphere

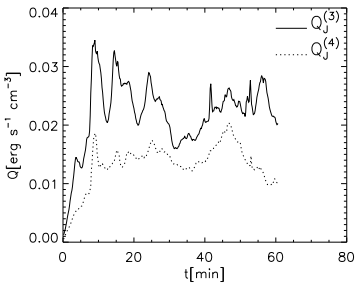

(b) B1, TR

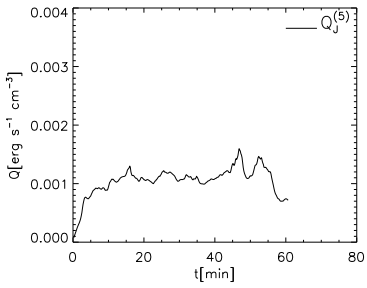

(c) B1, corona

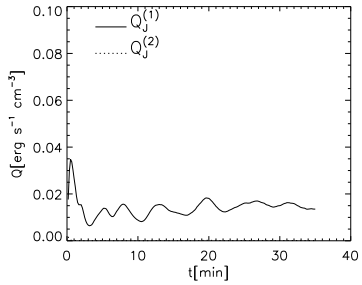

(d) C1x1, chromosphere

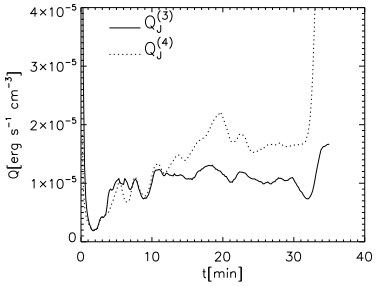

(e) C1x1, TR/corona

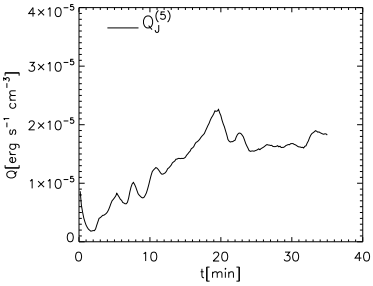

(f) C1x1, corona

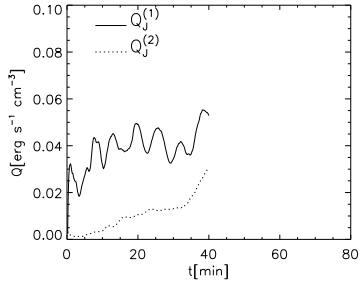

(g) C2x1, chromosphere

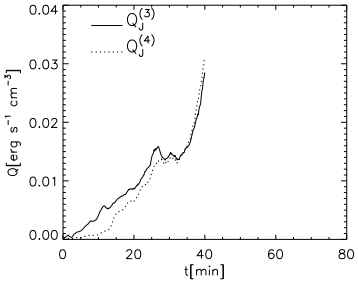

(h) C2x1, TR

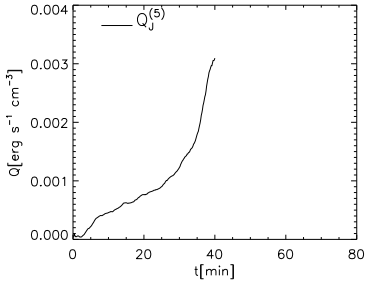

(i) C2x1, corona

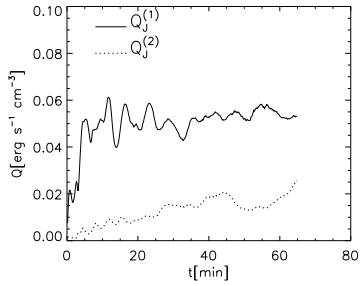

(j) C2x2, chromosphere

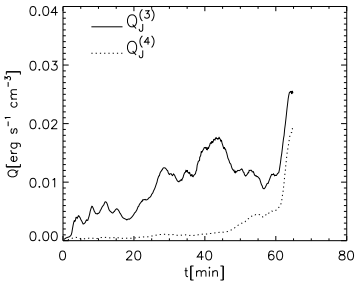

(k) C2x2, TR/coronal base

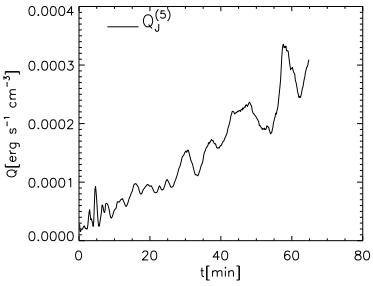

(l) C2x2, corona

Figure 3.21: Time plots of the mean Joule heating in the 5 selected regions for each model. Left column shows the mean Joule heating in the regions 1 and 2, middle column in region 2 and 3, right column in region 5. Note that the plots for C1x1 have different scaling than the the plots in the same column, because this model obtains much less Joule heating in the TR and the corona than the other models (and it runs for a quite short time). Several of the plots for the coronal heating (right column) have different scaling on the vertical axis (but the plots for C2x2, C4x2 and C4x3 have the same scaling.). The plots continues on figure 3.22.

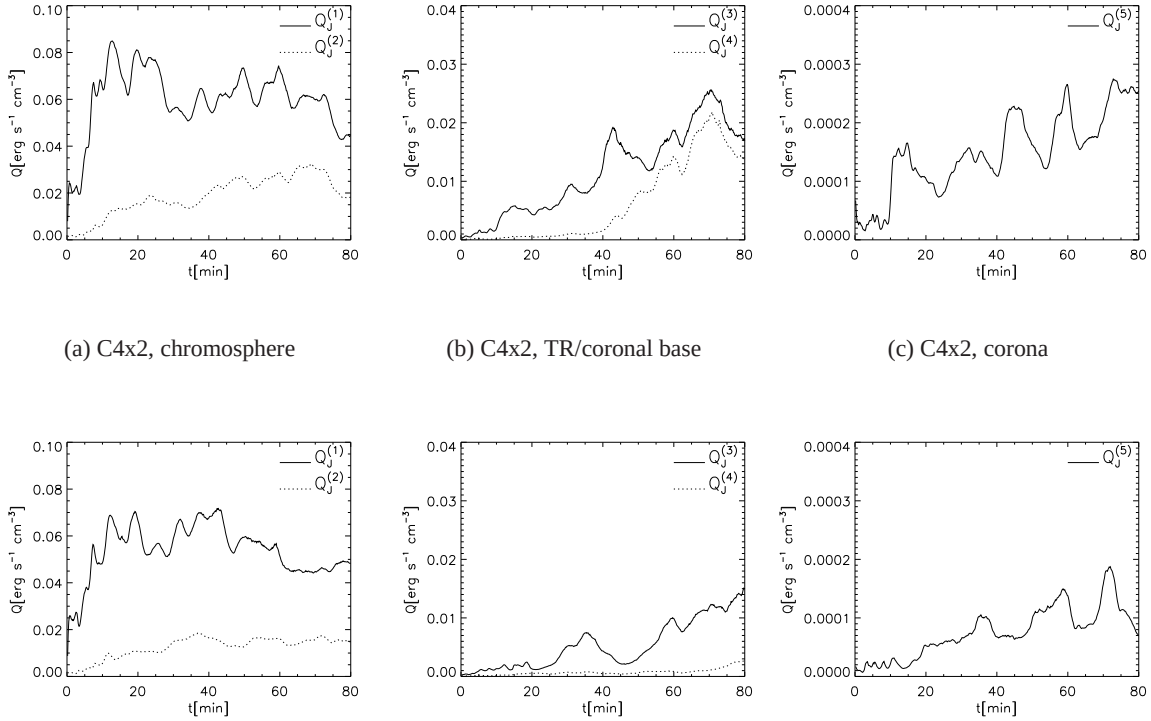

(a) C4x2, chromosphere (b) C4x2, TR/coronal base (c) C4x2, corona

(d) C4x3, chromosphere (e) C4x3, TR/coronal base (f) C4x3, corona

Figure 3.22: Time plots of the mean Joule heating in the 5 selected regions for each model. Left column shows the mean Joule heating in region 1, middle column in region 2, 3 and 4, right column in region 5. Each row corresponds to a specified model. The first part of these plots is on figure 3.21.

4

DISCUSSION AND CONCLUSIONS

4.1 Summary

In the introduction of this thesis, we first went briefly through the mechanics describing how a star works. Then we reviewed our current knowledge on one specific star, namely the Sun. We described how energy is released inside the core through nuclear fusion and transported through diffusion of electromagnetic radiation and convective motion until it leaves the Sun through the almost transparent atmosphere in the form of photons. Furthermore we went deeper into the structure of the solar atmosphere, from the quiet-Sun granulation and supergranulation to sunspots, prominences and spicules and how the density, pressure and temperature varies from the photosphere through the chromosphere and TR to the very hot corona. The fact that the corona lies from 1.5-2.5 Mm above the photosphere and outwards but is more than 200 times hotter than the photosphere led us right into the more than 60 year old problem which is dealt with in this thesis: Why does the solar corona have a temperature of more than 1 MK when the surface temperature is about only 6000 K?

A few plausible theories have been developed in attempt to answer that question, all agreeing about one thing: the heating of the corona is connected to the topology of the magnetic fields in the photosphere and the chromosphere. Therefore, the more specific problem that this thesis deals with is the following: What is the connection between the magnetic field configuration in the photosphere and the heating of the corona?

In attempt to answer this question, the numerical code Bifrost has been used to solve the MHD equations on a three-dimensional cutout of the solar atmosphere. This cutout is a box which reaches from below the photosphere and up into the corona (14.4 Mm above the photosphere). Five models have been evolved, all with the same initial condition for the hydrodynamic variables, but with different magnetic field configurations:

1) A magnetic monopole configuration i.e. a vertical homogeneous magnetic field

2) A magnetic bipole configuration

3) A magnetic quadrupole configuration

4) A magnetic 8-pole configuration

5) A magnetic 12-pole configuration (which, however, does not remain a 12-pole configuration throughout the simulation)

During the simulations, the resulting temperature structure and Joule heating have been analyzed in each model. This has been done by looking at three-dimensional plots at specific times in the simulations and at the time evolution of the interesting quantities in selected regions of the modeled atmospheres.

Having gone through the theoretical background, simulated different numerical models of the solar atmosphere and analyzed the results, it is now time to use what we have seen to draw some conclusions regarding the main problem of this thesis.

4.2 Finding a Correlation between Coronal Heating and the Photospheric Magnetic Field Configuration

By comparing all of the five models evolved in this thesis (the standard model will be brought into discussion later), one will immediately see that the coronal heating and temperature tends to *decrease* with the initial density of magnetic poles in the photosphere, except for the magnetic monopole model (C1x1), which has a density of magnetic poles equal to zero and has the lowest amount of coronal Joule heating and the lowest coronal temperature. The bipole model (C2x1) has the largest amount of coronal Joule heating, more than 100 times that of the monopole model. The three models of higher magnetic complexity (C2x2, C4x2 and C4x3) ends up with coronal Joule heating of about one order of magnitude lower than the bipole model (and one order of magnitude higher than the monopole model). Amongst those three, the quadrupole model (C2x2) gets the largest amount of coronal Joule heating, while model C4x3 gets lowest amount. Amongst these five models, there is a 1-1 correlation between the resulting coronal Joule heating and coronal temperature, i.e. the models which obtain higher coronal Joule heating obtain also higher temperature.

In the TR and upper chromosphere, the Joule heating tends to *increase* more or less with the effective density of magnetic poles, except for the bipole model, where the Joule heating increases more rapidly than in the other models. Model C4x3 has an effective density of magnetic poles which is lower than in the 8-pole model but higher than in the quadrupole model, but has a lower amount of Joule heating in these regions than both of the other two. This is probably due to the fact that the average magnetic field in the photosphere in this model is, during the second half of the simulation, significantly lower than in the other two models. In the lower chromosphere, the Joule heating tends to increase with the effective density of magnetic poles in the photosphere for all five models evolved in this thesis.

The standard model breaks with the above-mentioned (almost 1-1) correlations between the complexity in the photospheric magnetic field, the coronal Joule heating and temperature. Having a magnetic complexity in the photosphere somewhere between that of the quadrupole model and that of the 8-pole model, it has a coronal heating almost comparable to that of the bipole model, but still a temperature lower than in the 8-pole model. But in the chromosphere, the model fits well into the above-mentioned correlations between magnetic complexity and Joule heating (and it is approximately the same case with the TR).

In order to interpret the results summarized above, it is important to point out the fact that we deal with

three different kinds of models here. The magnetic quadrupole model, the 8-pole model and model C4x3 have magnetic field configurations which contains "grids" of magnetic poles in the photosphere. The bipole model represents a *line* of several magnetic poles (when considering the horizontal periodicity of the model). Finally, the standard model represents a "salt-pepper" pattern (a term introduced in section 1.3.1) of magnetic poles similar to the "magnetic grid"- models, but where the poles are more chaotically organized.

In each of the "magnetic grid"-models, the grid of magnetic poles gives rise to a corresponding grid of relatively strong vertical current sheets which heat up the corona. These current sheets are most probably regions where topologically separate parts of the magnetic configuration are pushed together, resulting in large gradients (in the magnetic field components), as mentioned briefly in chapter 1. The magnetic field on both sides of such a current sheet is more or less vertical but tilted slightly in different directions due to different topologies on each side of the current sheet, as seen in figure 3.9. The slight difference in the tilting of the magnetic field gives rise to the strong currents in the current sheet.

Amongst the three "magnetic grid"-models, the quadrupole model has the "current sheet grid" with the largest grid size, i.e. the longest distance between the strong current sheets, due to the lowest magnetic complexity of those three models. The 8-pole has the tightest grid of current sheets, which is probably the cause of the highest heating of the TR and chromosphere. Model C4x3 has a current sheet grid size in-between those of the quadrupole and the 8-pole model, but the current sheets in this model tends to be weaker, and that causes this model to get the lowest chromospheric heating of those three models.

Near the strong vertical current sheets which are arranged in grids in the magnetic grid-models, a *hierarchy* of weaker current sheets arise in the coronal regions. Those weaker current sheets lie parallel to the stronger grid current sheets. The hierarchy of current sheets tends to be more complex in the quadrupole model than in the 8-pole model, i.e. the number of weaker current sheets which lies nearby each of the strong "main current sheets" (those which lies diagonally between two magnetic poles) is larger, as seen figure 3.14. This may explain why the quadrupole model results in more coronal heating than the 8-pole model. Model C4x3 also has a relatively complex hierarchy of weaker current sheets, but the currents in this model tends to be weaker than in the other two models, which may explain why this model gets the smallest amount of coronal heating.

It is also possible that the stressing of magnetic field lines (due to the convective motions) which collapse into tiny current sheets (with a width of $\sim$100 km in the models, though only $\sim$10 m on the real Sun) and eventually burst out in *nanoflares*, is a significant contributor to the coronal heating in those magnetic grid-models. As discussed earlier, an atmosphere with a higher canopy height is likely to get more heat input from nanoflares, as demonstrated in figure 4.1. In the quadrupole and 8-pole models, the canopy is slightly above the TR, while it seems to be slightly below the TR in model C4x3. That might be another reason this model has less coronal heating than the two other magnetic grid-models.

For models with grids of magnetic poles in the photosphere, we can thus conclude that the coronal heating *increases* with the initial separation distance between magnetic poles in the photosphere (or decreases with the initial complexity) for typical separation distances shorter than 6-7 Mm (which is the case for the quadrupole model). If we simulate similar models with a higher separation distance

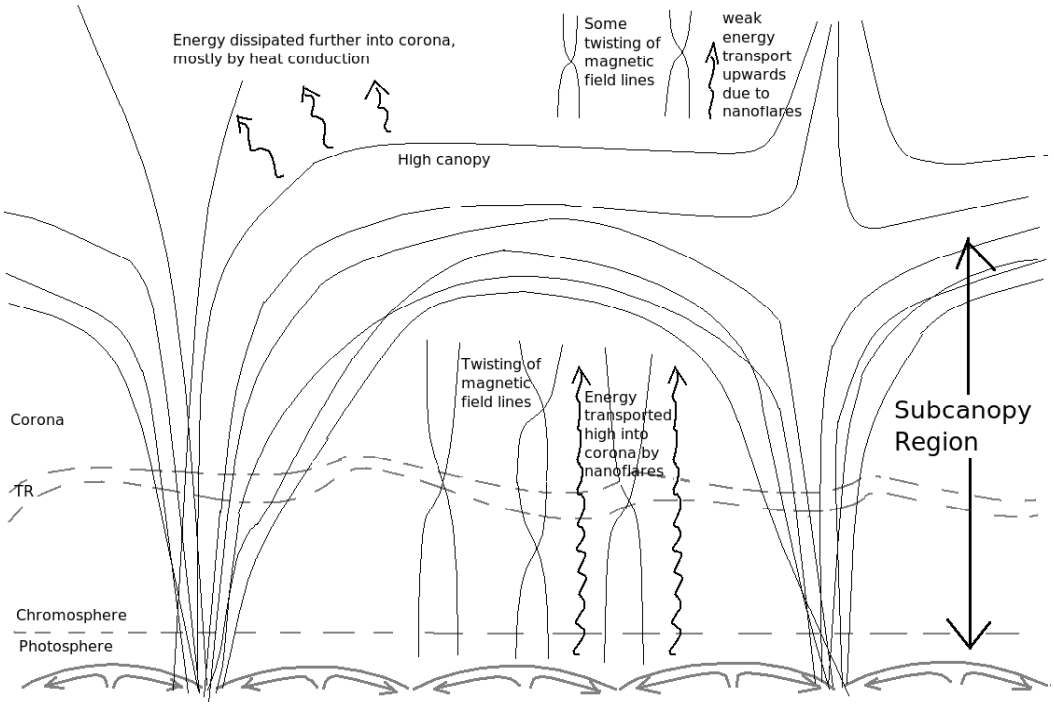

(a) Atmosphere with high separation distance between photospheric magnetic poles.

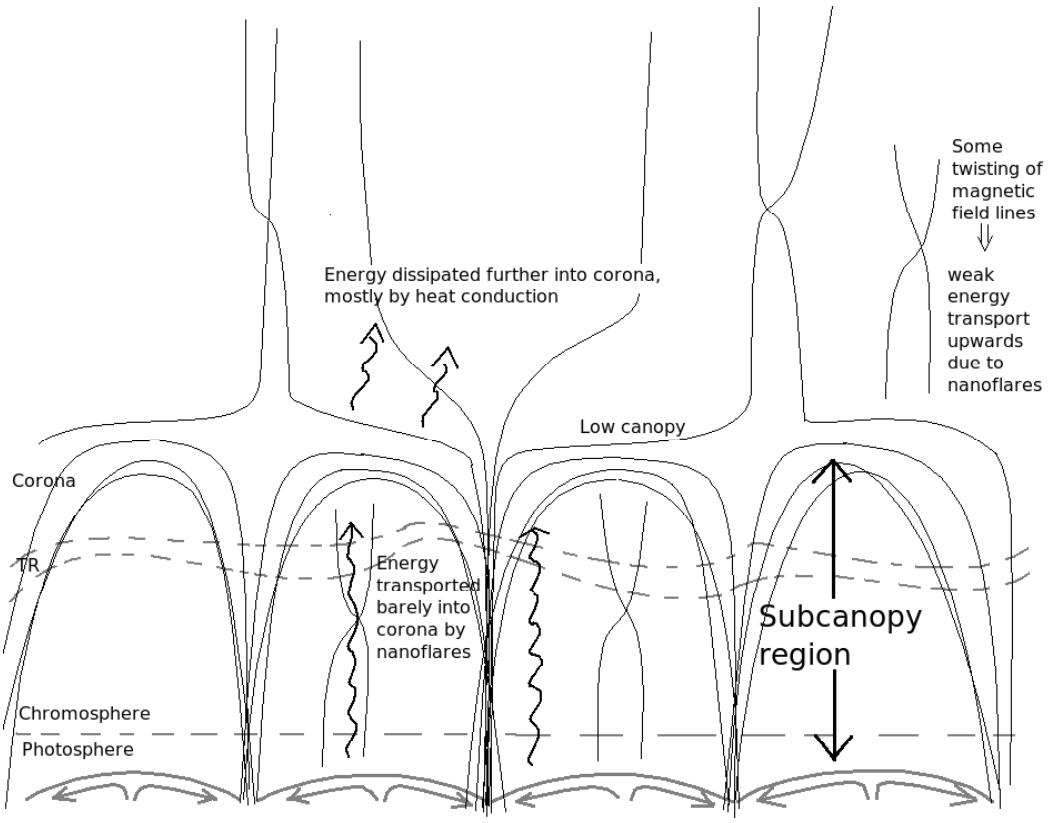

(b) Atmosphere with low separation distance between photospheric magnetic poles.

Figure 4.1: Sketches of two models of the QS atmosphere with different magnetic topology, demonstrating the dissipation of energy through nanoflares. Region borders are given by dashed lines. Magnetic fields are given by solid black lines. The loose (twisted) magnetic field lines sketched in sub-canopy regions and in regions above canopy are only to demonstrate the generation of nanoflares.

than that (which requires a larger computational box), an even higher amount of coronal heating may result. However, increasing the magnetic pole separation distance towards infinity should result in a model similar to the monopole model i.e. a coronal heating which goes almost towards zero. Therefore, amongst such magnetic grid-models, there is probably a typical pole separation distance, larger than 6-7 Mm which gives a maximum coronal heat input.

The bipole model has a very different magnetic structure than the magnetic grid-models. The magnetic topology of this model, representing a line of several poles, causes the presence of a magnetic neutral line, going in the horizontal direction perpendicular to the line of poles, above each second pole, similar to what is demonstrated in figure 1.17. The region around the magnetic neutral line generates current sheets which are much stronger than those generated in the magnetic grid-models, going out in all directions in the corona. Additionally, the high location of the magnetic canopy might allow nanoflares to more easily dissipate energy into the corona than in the magnetic grid-models. Thus, it is no surprise that this model gets a higher chromospheric heating than the magnetic grid models and a coronal heating which is one order of magnitude higher.

Since the main heat generator in the bipole model is the magnetic neutral line, a similar bipole model with longer distance between the poles (requiring a larger computational box to simulate) will probably obtain lower coronal temperatures, because the distance between several magnetic lines (considering the model to represent a longer line of poles) will be longer, or in other words, the energy from the current sheets generated near the magnetic neutral line will have a larger volume to dissipate into. However, this remains only speculation until it is numerically tested.

The photospheric magnetic field configuration in the standard model represents a salt-pepper pattern of magnetic poles, partially similar to the three magnetic grid-models evolved in this thesis, but more chaotically organized. Having a magnetic complexity in the photosphere which lies between that of the quadrupole and 8-pole models, the corona obtains still three times as high amount of Joule heating after 50-60 min than the quadrupole model does at the same time (and 1/3 of what the bipole model seems to end up with). The relatively high coronal Joule heating is likely to be caused by the fact that the chaotically organized pattern of magnetic poles gives rise to a very large and chaotically organized hierarchy of current sheets (and therefore most of the current sheets are impossible to see separately in the three-dimensional current-plot in figure 3.2(b)). Additionally, the fact that a large part of the magnetic loops reach deep into the corona probably allows nanoflares to dissipate more easily into the corona. Thus, the model obtains a coronal Joule heating almost comparable to that of the bipole model. Still, this model ends up with a lower coronal temperatures than in the quadrupole and 8-pole models. This could be caused by coronal loops which transport cooler matter from the chromosphere (or maybe lower TR) up to the corona which cools down the surrounding gas before it eventually falls back to the chromosphere. It could also just be the magnetic field configuration in this model which possibly allows more heat conduction from the corona to cooler zones than in the models evolved in this thesis, or possibly radiative cooling (needs further analysis).

Summarizing the Conclusions

For a region in the QS atmosphere with a strict square grid of magnetic poles in the photosphere, the corona receives an amount of Joule heating and a temperature which increases with the typical separation distance between magnetic poles (or decreases with the magnetic pole density), for separ-

ation distances shorter than 6-7 Mm (i.e. the longest possible separation distance possible for such magnetic grid-models in the computational boxes used here), as long as the average magnetic field strength in the photosphere is the same. This increase is mainly due to the corresponding increase in distances between the strong vertical current sheets located diagonally between magnetic poles, which gives more space for a series of weaker current sheets – parallel to the stronger current sheets – to be generated (i.e. a more complex *hierarchy* of current sheets). Another possible factor which affects the coronal heating is the amount of nanoflares dissipated into the corona, which also may increase with the pole separation due to a corresponding increase in the canopy height. If we keep increasing the pole separation distance, the coronal Joule heating will at some point reach a maximum value and decrease to a relatively small value as the pole separation distances goes towards infinity.

Having a more chaotically organized pattern results in higher amounts of coronal Joule heating due to more complex and dynamic hierarchy of large-scale current sheets and possibly more dissipation of energy from nanoflares. However, according to the numerical results, a more chaotic magnetic field will also allow some cooling events (due to coronal loops, heat conduction or radiative cooling) to occur in the corona and cause the resulting temperature to be slightly below the coronal temperature of a magnetic grid-model with the same pole mean separation distance. This kind of model is of course more likely to represent the QS atmosphere than the models which contain strict grids of magnetic poles. However, the coronal heating due to generation of current sheets will probably still increase with the typical separation distance between magnetic poles in a similar way. In other words, the coronal Joule heating in a salt-pepper pattern of magnetic poles increases both with the typical separation distance between magnetic poles and with a "chaos factor". That chaos factor can be qualitatively defined as a number which tells how much the pattern of magnetic poles deviates from a strict square grid (a quantitative definition is not necessary here, since only the standard model has magnetic poles which deviates from a strict square pattern). The temperature will also increase with the pole separation distance, but probably decrease with the chaos factor, according to the numerical models that were studied (we have, however, only studied one model with a chaotic pattern of magnetic poles, so the latter conclusion needs more simulations to be confirmed).

A region in the QS atmosphere which contains a line of several magnetic poles (as represented by the bipole model) will be heated more efficiently than a region in a salt-pepper pattern, and the heating will also increase with the density of poles along the line, as long as the pole distance does not get too short.

4.3 Possible Coronal Heating Mechanism

It is probable that the QS corona is heated by a hierarchy of current sheets, as described by Galsgaard & Nordlund (1996), generated above a salt-pepper pattern of magnetic poles in the photospheric internetwork. The current sheets may be regions where topologically separate parts of a magnetic configuration are pushed together, as seen in some of the three-dimensional current plots from the previous chapter. It can also be caused by the convective shuffling of magnetic field lines which generates nanoflares, as described by Parker (1988). The coronal heating dissipated by the current sheets in the former case increases with the typical separation distance between magnetic poles, at least for a typical pole separation distance shorter than 6-7 Mm. The heating dissipated by nanoflares

is likely to increase with the height of the magnetic canopy, which is because nanoflares are more likely to be produced in the sub-canopy region than above the canopy (since the magnetic field in the sub-canopy region is both stronger and more closely connected to the convective motions in the photosphere than the field above the canopy), and the height of the canopy also increase, more or less, with the typical pole separation distance. Thus, the total heating of the corona above a salt-pepper pattern of magnetic poles in the photosphere will increase when increasing the typical magnetic pole separation distance up to a certain value (longer than 6-7 Mm) before it starts decreasing as the separation distance goes towards infinity.

It might be possible to find lines with poles (as in the bipole model) of stronger magnetic fields in the magnetic network along the supergranular borders, since these regions are observed to contain relatively strong magnetic fields. If so, that might cause the existence of magnetic neutral lines which generate very strong current sheets. However, the resulting coronal temperature in the nearby region will not be as high as seen in the bipole model (>3.0 MK), because the energy dissipated in the strong current sheets will diffuse into the surrounding internetwork.

4.4 Final Thoughts

Because of limited time and computer resources, we have only been able to simulate five models of the QS atmosphere with different initial conditions for the magnetic field, and some of the models have run for a shorter time interval (of solar time) than ideally wanted. Therefore, it is limited how precise conclusions we can derive from our results with respect to the problem of this thesis. However, we have not failed to answer the problem dealt with in this thesis. We have managed to obtain an idea about how the coronal heating and temperature depends on the complexity of the magnetic field in the photosphere, and thus we are one (small) step closer to solving the coronal heating problem.

What could have been done better?

- Some of the models should have been run for a longer time in order to ensure stabilization of Joule heating and temperature. That would have made the results easier to analyse and compare.
- We could have included models with different magnetic pole distributions in the photosphere to get a broader set of results.

Thoughts for Future Research

There is definitely a need for more research on this problem. A suitable next step would be to start systematically analyzing more models with different densities of magnetic poles in the photosphere systematically. It would also be interesting to study models with roughly equal magnetic pole densities but with a more chaotically organized pattern of poles. With larger computational boxes, one should also study models with even smaller magnetic pole densities than in the models simulated in this thesis in order to see what magnetic pole density which yields the maximum coronal heating.

It might also be interesting to study bipole models with longer distances between the poles (requires a larger computational box) to see if the resulting coronal heat input decreases, as expected, or if the opposite happens.

BIBLIOGRAPHY

Arp, H. C., Baum, W. A., & Sandage, A. R. 1952, Astrophysical Journal, 57, 4

Aschwanden, M. J., & Charbonneau, P. 2002, Astrophysical Journal, 566, L59

Asplund, M., Grevesse, N., Sauval, A. J., & Scott, P. 2009, Annual Review of Astronomy & Astrophysics, 47, 481

Aquilano, R., Dávoli, D., Missio, H., & Acero, S. 2003, Boletin de la Asociacion Argentina de Astronomia La Plata Argentina, 46, 6

Braithwaite, J., & Nordlund, AA. 2006, Astronomy and Astrophysics, 450, 1077

Chaisson, E., & McMillan, S. 2005, Astronomy Today, 5th Edition, by E. Chaisson and S. McMillan. Prentice Hall, 2005. ISBN 0-13-144596-0.,

Cheung, M. C. M., Schüssler, M., & Moreno-Insertis, F. 2007, Astronomy & Astrophysics, 461, 1163

Copernicus, N. 1543, Norimbergae, Apud J. Petreium, 1543; [Bruxelles, Culture et Civilisation, 1966],

Yelles Chaouche, L., Moreno-Insertis, F., Martínez Pillet, V., et al. 2011, Astrophysical Journey, 727, L30

de Pontieu, B., et al. 2007, A Tale of Two Spicules: The Impact of Spicules on the Magnetic Chromosphere, Publications of the Astronomical Society of Japan, 59, 655

De Pontieu, B., McIntosh, S. W., Hansteen, V. H., & Schrijver, C. J. 2009, Astrophysical Journal, 701, L1

de Wijn, A. G., Stenflo, J. O., Solanki, S. K., & Tsuneta, S. 2009, Space Science Reviews, 144, 275

Einstein, A. 1905, Annalen der Physik, 323, 639

Feldman, U., Ralchenko, Y., & Doschek, G. A. 2010, ApJ, 708, 244

Gabriel, A. H. 1976, Royal Society of London Philosophical Transactions Series A, 281, 339

Galsgaard, K., & Longbottom, A. W. 1999, Astrophysical Journal, 510, 444

Galsgaard, K., & Nordlund, Å. 1996, Journal of Geophysical Research, 101, 13445

Gott, J. R., III, Jurić, M., Schlegel, D., et al. 2005, Astrophysical Journal, 624, 463

Gizon, L., Birch, A. C., & Spruit, H. C. 2010, Annual Review of Astronomy and Astrophysics, 48, 289

Gudiksen, B. V., & Nordlund, Astronomy and Astrophysics. 2005, Astrophysical Journal, 618, 1020

Gudiksen, B. V., Carlsson, M., Hansteen, V. H., Hayek, W., Leenaarts, J., & Martínez-Sykora, J. 2011, arXiv:1105.6306

Gustafsson, B., Bell, R. A., Eriksson, K., & Nordlund, A. 1975, Astronomy & Astrophysics, 42, 407

Hale, G. E., & Nicholson, S. B. 1938, Washington, D.C. Carnegie institution of Washington, 1938.,

Hansen, C. J., Kawaler, S. D., & Trimble, V. 2004, Stellar interiors : physical principles, structure, and evolution, 2nd ed., by C.J. Hansen, S.D. Kawaler, and V. Trimble. New York: Springer-Verlag, 2004.,

Hansteen, V. H., De Pontieu, B., Rouppe van der Voort, L., van Noort, M., & Carlsson, M. 2006, Astrophysical Journal, 647, L73

Hansteen, V. H., Hara, H., De Pontieu, B., & Carlsson, M. 2010, Astrophysical Journal, 718, 1070

Hart, A. B. 1954, Monthly Notices of the Royal Astronomical Society, 114, 17

Hasan, S. S., van Ballegooijen, A. A., Kalkofen, W., & Steiner, O. 2005, Astrophysical Journal, 631, 1270

Hirayama, T. 1971, Solar Physics, 19, 384

Hyman, J. in R. Vichnevetsky, R. S. Stepleman (eds.), Adv. in Comp. Meth. for PDE's–III, 313

Inglis, M. 2003, Observer's guide to stellar evolution: the birth, life, and death of stars, Springer,

Kalinkov, M. 1983, Early Evolution of the Universe and its Present Structure, 104, 187

Karachentsev, I. D. 2005, The Astronomical Journal, 129, 178

Karachentsev, I. D., Kashibadze, O. G., Makarov, D. I., & Tully, R. B. 2009, Monthly Notices of the Royal Astronomical Society, 393, 1265

Kerr, F. J., & Lynden-Bell, D. 1986, Royal Astronomical Society, Monthly Notices, 221, 1023

Khokhlova, V. L. 1959, Soviet Astronomy, 3, 59

Kitchatinov, L. L. 2011, arXiv:1108.1604

Kneer, F., & von Uexkuell, M. 1985, A&A, 144, 443

Kosovichev, A. G. 1995, Advances in Space Research, 15, 95

Kosovichev, A. G. 1996, Bulletin of the Astronomical Society of India, 24, 355

Lattanzio, J., & Forestini, M. 1999, Asymptotic Giant Branch Stars, 191, 31

Leenaarts, J., Carlsson, M., Hansteen, V., & Gudiksen, B. V. 2011, A&A, 530, A124

Leighton, R. B., Noyes, R. W., & Simon, G. W. 1962, Astrophysical Journal, 135, 474

Maeder, A., & Meynet, G. 1989, Astronomy and Astrophysics, 210, 155

Major, B. 2004, Publications of the Astronomy Department of the Eotvos Lorand University, 14, 187

Martínez-Sykora, J., Hansteen, V., & Carlsson, M. 2008, Astrophysical Journal, 679, 871

Martínez-Sykora, J., Hansteen, V., & Carlsson, M. 2009, Astrophysical Journal, 702, 129

Mitalas, R., & Sills, K. R. 1992, Astrophysical Journal, 401, 759

Nordlund, A. 1984, Small-Scale Dynamical Processes in Quiet Stellar Atmospheres, 181

Nordlund, Å., & Galsgaard, K. From: Klaus Galsgaard's PhD Thesis Page. 1995, "A 3D MHD Code for Parallel Computers", Retrieved on 8/9/01 from: `http://www.astro.ku.dk/~kg`

November, L. J., Toomre, J., Gebbie, K. B., & Simon, G. W. 1981, Astrophysical Journal, 245, L123

Parker, E. N. 1988, ApJ, 330, 474

Priest, E. R. 1982, Solar Magneto-hydrodynamics, Dordrecht, Holland ; Boston : D. Reidel Pub. Co. ; Hingham„ 74P

Rieutord, M., & Rincon, F. 2010, Living Reviews in Solar Physics, 7, 2

Roudier, T., Rincon, F., Rieutord, M., et al. 2009, The Second Hinode Science Meeting: Beyond Discovery-Toward Understanding, 415, 203

Rouppe van der Voort, L., Leenaarts, J., de Pontieu, B., Carlsson, M., & Vissers, G. 2009, Astrophysical Journal, 705, 272

Rusov, V. D., et al. 2010, arXiv:1009.3340

Sandage, A. R. 1953, Astrophysical Journal, 58, 61

Schrijver, C. J., & Siscoe, G. L. 2009, Heliophysics: Plasma Physics of the Local Cosmos, Edited by Carolus J. Schrijver and George L. Siscoe. Published by Cambridge University Press, London 2009. ISBN: 9780521110617,

Schwarzschild, M. 1958, Princeton, Princeton University Press, 1958.,

Socas-Navarro, H., Martínez Pillet, V., & Lites, B. W. 2004, Astrophysical Journal, 611, 1139

Sotnikova, R. T. 1978, Solnechnye Dann. Bull. Akad. Nauk SSSR, 1977, 97

Stix, M. 2004, The sun : an introduction, 2nd ed., by Michael Stix. Astronomy and astrophysics library, Berlin: Springer, 2004. ISBN: 3540207414,

Wedemeyer-Böhm, S., Lagg, A., & Nordlund, Astronomy and Astrophysics. 2009, Space Science Reviews, 144, 317